

Polaris Underground Project at Sudbury Neutrino Observatory (P.U.P.S.)

Final Report

NWMO TR-2009-02

December 2011

Gail Atkinson and Nadia Kraeva

University of Western Ontario

nwmo

NUCLEAR WASTE
MANAGEMENT
ORGANIZATION

SOCIÉTÉ DE GESTION
DES DÉCHETS
NUCLÉAIRES

Nuclear Waste Management Organization

22 St. Clair Avenue East, 6th Floor
Toronto, Ontario
M4T 2S3
Canada

Tel: 416-934-9814
Web: www.nwmo.ca

**Polaris Underground Project at Sudbury Neutrino Observatory (P.U.P.S.)
Final Report**

NWMO TR-2009-02

December 2011

Gail Atkinson and Nadia Kraeva

University of Western Ontario

Disclaimer:

This report does not necessarily reflect the views or position of the Nuclear Waste Management Organization, its directors, officers, employees and agents (the "NWMO") and unless otherwise specifically stated, is made available to the public by the NWMO for information only. The contents of this report reflect the views of the author(s) who are solely responsible for the text and its conclusions as well as the accuracy of any data used in its creation. The NWMO does not make any warranty, express or implied, or assume any legal liability or responsibility for the accuracy, completeness, or usefulness of any information disclosed, or represent that the use of any information would not infringe privately owned rights. Any reference to a specific commercial product, process or service by trade name, trademark, manufacturer, or otherwise, does not constitute or imply its endorsement, recommendation, or preference by NWMO.

ABSTRACT

Title: Polaris Underground Project at Sudbury Neutrino Observatory (P.U.P.S.)
Final Report
Report No.: NWMO TR-2009-02
Author(s): Gail Atkinson and Nadia Kraeva
Company: University of Western Ontario
Date: December, 2011

Abstract

All existing ground-motion prediction equations that are applied in seismic hazard analyses apply to sites on the Earth's surface. To extend seismic hazard analyses and ground-motion estimates to sites underground, information on the relationship between motions underground and those on the surface is required. The key objective of this study is to determine how ground motions recorded in underground cavities compare with those on the Earth's surface. This report describes the results of the 3-year PUPS (POLARIS Underground Project at Sudbury Neutrino Observatory (SNO)) research program. Ground motions on the surface and underground have been analyzed for 106 local events (shallow mining-induced events and blasts), 66 regional earthquakes (moderate events hundreds of km away), and 73 teleseismic events (large earthquakes >1000 km away).

The results of this study demonstrate that, in general, earthquake ground motions in underground cavities are lower in amplitude than those on the surface. The relationship between underground and surface motions is complex, with the ratio of surface/underground motions being a frequency-dependent function that depends on the type of earthquake and the depth of the underground cavern. Motions on the surface are amplified in specific frequency ranges due to the presence of surface waves in the signal. For earthquakes at shallow depths, occurring nearby, there are strong surface waves that cause a peak amplification of surface motions relative to those underground that often exceed a factor of two; this peak occurs near a frequency of 2 Hz. For larger earthquakes happening further away, the surface waves cause amplification at longer periods. These motions decrease in amplitude as the depth of the underground station increases, because surface-wave amplitudes diminish with increasing depth. At very low frequencies (0.1 Hz), and at very high frequencies (>10 Hz), underground and surface motions are very similar in amplitude. In general, both the potential for surface waves, and the frequency range that they affect, is dependent on the characteristics of the source (such as its depth) and the distance to the site. Consideration of these factors when assessing the seismic hazard for underground repositories may reduce the predicted ground motion levels for specific types of events.

An important conclusion regarding the attenuation of ground motion near the earthquake source was also drawn from the results of this study. Studies of signals at Sudbury, in comparison to those at SNO, show that ground motions decay at a rate of approximately $R^{-1.3}$ in the first 20 to 30 km from the earthquake source (where R is distance). This supports the ground-motion prediction equations of Atkinson and Boore (2006), and implies that a mitigating factor in seismic hazard studies in Ontario is this relatively steep attenuation of wave amplitudes moving away from an earthquake source. The studies at SNO have shown that there is a clear de-amplification of ground motions at underground stations relative to those on the surface, which depends on the type of earthquake and the depth of the station. The effect appears to be mostly due to the removal of surface wave energy at depth, and thus depends on the depth of the seismic event and its distance, as well as the depth of the station.

TABLE OF CONTENTS

	<u>Page</u>
ABSTRACT	v
1. INTRODUCTION	1
1.1 Background	1
1.2 POLARIS Underground Project at SNO (PUPS)	2
2. DATA ANALYSIS	6
2.1 Quality-control of data	6
2.2 Database	13
2.3 Noise-removing filter algorithm	25
2.4 Data processing	27
3. COMPARISON OF MOTIONS ON SURFACE TO UNDERGROUND	38
3.1 Analysis of Fourier Spectra	38
3.1.1 A few examples of spectral ratios for typical event variants	38
3.1.2 Average spectral ratios: nearest ($\Delta=8-40$ km) versus most distant ($\Delta>3500$ km) events.....	44
3.1.3 Average spectral ratios for local events at a range of distances ($\Delta=8-$ 100 km).....	49
3.1.4 Average spectral ratios for regional events ($\Delta=100-1050$ km).....	53
3.2 Analysis of Response Spectra	53
3.3 Summary of ground motions underground compared to those on the surface	60
3.4 Overview of high-frequency Rg studies	67
3.5 High-frequency Rg and Lg waves observed in Canada by surface stations at local and regional distances	68
4. IMPLICATIONS FOR OTHER GROUND MOTION PARAMETERS	78
4.1 Attenuation of ground motions near the earthquake source (<50 km)	78
4.2 Determination of high-frequency attenuation factor kappa	80
5. CONCLUSIONS	83
REFERENCES	85

LIST OF TABLES

	<u>Page</u>
Table 1: Seismograph Station coordinates.....	4
Table 2: Summary of data availability (excluding erroneous or suspect data)	11
Table 3: Actual orientation of horizontal channels of SUNO and PUPS stations	12
Table 4: Local events within 100 km of DSNO station (46.47500, -81.20111), August 2006 - October 2009	13
Table 5: Events in the Vale Creighton Mine monitored by SNO Lab and recorded by SNO and SUNO stations in August 2006 - April 2008 but with unknown location	17
Table 6: Events within 7 km of DSNO station (46.47500, -81.20111), August 2006 – October 2009, with coseismic effects (unprocessed events with permanent offsets)	17
Table 7: Teleseismic events, August 2006-April 2009.....	20
Table 8: Regional events within 1050 km of DSNO station (46.47500, -81.20111), August 2006-October 2009	22

LIST OF FIGURES

	<u>Page</u>
Figure 1: Vertical (SE-NW direction) rough scheme of SNO Lab location (http://sno.phy.queensu.ca). Surface facilities are located near the head of Shaft #9. The full horizontal distance from the Shaft #9 to SNO is about 2 km. Approximate positions of stations are shown by the red circles.....	2
Figure 2: Simplified geological map of the Sudbury Basin.	3
Figure 3: Map showing local event epicentres and stations locations. The pink filled circles correspond to the group of 8 mining events used for the full frequency band (0.5-100 Hz) spectral ratio analysis.	4
Figure 4: Nominal frequency response of SSNO station (red) and SUNO station (green).....	6
Figure 5: Typical Fourier amplitude spectra smoothed and corrected for instrument, of vertical component of ambient noise recorded on 2 July 2008 by 5 SNO stations and the SUNO station. Amplitude corresponds to velocity in m/s.	7
Figure 6: Fourier amplitude smoothed spectra of 2-h vertical records of ambient noise observed by 5 broadband SNO stations: (a) 11 November 2007 during electricity disconnection; (b) 12 November 2007, the next day after electricity was reconnected.	8
Figure 7: Fourier amplitude spectra of ambient noise (corrected for instrument) recorded on 27 August 2006. Station 46SNO (black line) worked incorrectly at this time.....	9

Figure 8: Fourier amplitude smoothed spectra of 82 min vertical records of ambient noise registered by 5 broadband SNO stations 29 November 2006, just before the Lively earthquake MN4.1. Note the problem with DSNO (blue).	9
Figure 9: Fourier amplitude smoothed spectra of 40-minute vertical records of ambient noise and a mining event MN 2.1 observed by 5 broadband SNO stations 20 November 2006. Note the problem with DSNO (blue).	10
Figure 10: Comparison of ambient noise spectra (corrected for instrument) recorded by the unlevelled DSNO station (dark blue curve) and other stations working as usual, 7 October 2008.	10
Figure 11: Ambient noise spectra (corrected for instrument) recorded by SNO and SUNO stations on 18 November 2008, two weeks after installation of the NSNO station (green line).	12
Figure 12: Distribution of local magnitudes MN in epicentre distance calculated for DSNO station for events listed in Table 4.	16
Figure 13: 3-component displacement, velocity and acceleration recorded by the 46SNO station 7 October 2007 in the coseismic slip area of the event MN3.1.....	19
Figure 14: Map showing teleseismic events epicentres and DSNO station location.	21
Figure 15: Distribution of moment magnitudes Mw in epicentre distance calculated for DSNO station for teleseismic events listed in Table 7.	22
Figure 16: Distribution of moment magnitudes Mw in epicentre distance calculated for DSNO station for regional events listed in Table 8.	24
Figure 17: Map showing regional events epicentres and DSNO station location.....	24
Figure 18: (a) Signal-to-noise ratio (red line) and noise suppressing filter (green line) amplitude spectra estimated for the 28 November 2007 M3.0 local mining related event recorded by the vertical channel of 11SNO station. (b) Top - noisy signal; bottom – enhanced signal, both in the frequency band 0.1-50 Hz.....	26
Figure 19: (a) Signal-to-noise ratio (red line) and noise suppressing filter (green line) amplitude spectra estimated for the 11 May 2008 MN2.6 (Table 3) local mining event recorded by the vertical channel of 11SNO station. (b) S-wave velocity spectra before (red line) and after (green line) filtration by the noise removing filter shown on the left.	26
Figure 20: Accelerograms of the same event as in Figure 19 recorded by vertical channels of stations (a) 11SNO and (b) DSNO. Upper lines correspond to instrument-corrected signals before filtering. Middle lines show Butterworth-filtered data in the frequency band 0.1-50 Hz; bottom lines are data after applying both noise-subtraction and additional Butterworth filtering in the frequency band 0.5-30 Hz.....	27
Figure 21: Data preparation steps. (a) <i>step1</i> : prepare velocity records for the given event (30 s before and 60 s after the P-arrival), corrected for instrument and filtered, with all information about the event and station in headers of files in the SAC-format. (b) <i>step2</i> : prepare acceleration S-wave 10 s records for the given event with noise removed by spectral subtraction.....	28
Figure 22: Seismograms of the typical mining event of MN2.6 that occurred on 11 May 2008 in the Vale Creighton mine, at 23 km distance and azimuth 334° from the SNO Lab. Seismograms are rotated to the system coordinates of the source for visual	

picking operations using polarisation properties of arriving waves. (a) Surface station 11SNO. (b) Underground station DSNO.....	30
Figure 23: Fourier spectra of acceleration with log smoothing for the mining event on 11 May 2008, of MN2.6 (Figure 22). (a) Spectra for average horizontal components of S-waves observed at 5 SNO stations and the SUNO station. (b) The same as in (a) but for vertical components. (c) Spectra for average horizontal components calculated for the whole records including both P and S waves. (d) The same as in (c) but for vertical components.	31
Figure 24: Response spectra for the mining event of 11 May 2008 MN2.6 (Figure 22). (a) Spectra for average horizontal components of S-wave observed at 5 SNO stations and the SUNO station. (b) The same as in (a) but for vertical components. (c) Spectra for average horizontal components calculated for the whole records including both P and S waves. (d) The same as in (c) but for vertical components.	32
Figure 25: Seismograms of the teleseismic earthquake Mw7.9, 12 May 2008, Sichuan, China. Seismograms are corrected for the instrument, rotated to the system coordinates of the source and filtered in the band pass 0.03-7 Hz. The bottom line corresponds to the product of vertical Z and radial R components. (a) Surface station SSNO. (b) Underground station DSNO.	33
Figure 26: Smoothed Fourier spectra of average horizontal (a) and vertical (b) components of acceleration (P and S waveforms, duration 1000 s), for the teleseismic earthquake Mw7.9, 12 May 2008, Sichuan, China (Figure 25) recorded by 5 SNO stations and the SUNO station.	34
Figure 27: Response spectra of average horizontal (a) and vertical (b) components of acceleration (P and S waveforms, duration 1000 s) for the same Sichuan event as in Figure 25.	34
Figure 28: Seismograms of the regional earthquake Mw5.4, 18 April 2008, Southern Illinois, USA. Seismograms are corrected for the instrument, rotated to the system coordinates of the source and filtered in the band pass 0.2-5 Hz. The bottom line corresponds to the product of vertical Z and radial R components. (a) Surface station 11SNO. (b) Underground station 46SNO.	35
Figure 29: Seismogram of the regional event (probable blast) MN2.5, 5 Feb 2008, east coast of Georgian Bay. Seismograms are processed as in Figure 28, but filtered in the band pass 0.5-12 Hz. (a) Surface station SSNO. (b) Underground station DSNO.....	35
Figure 30: Response spectra of average horizontal (a) and vertical (b) components (including S and surface waves, duration 180 s) of acceleration for the Illinois event (Figure 28 and Figure 30). Designations are the same as in Figure 30.	36
Figure 31: Smoothed Fourier spectra of average horizontal (a) and vertical (b) components of acceleration (including S and surface waves, duration 40 s), for the Georgian Bay event (Figure 29). Designations are the same as in Figure 30.	36
Figure 32: Smoothed Fourier spectra of average horizontal (a) and vertical (b) components of acceleration (including S and surface waves, duration 180 s), for the Illinois event (Figure 28).	37
Figure 33: Response spectra of average horizontal (a) and vertical (b) components of acceleration for the Georgian Bay event (Figure 29 and 31). Designations are the same as in Figure 30.	37

Figure 34: Log ratios of surface motions to underground motions for the typical mining event MN2.6 on 11 May 2008 calculated for Fourier spectra of S-waves. (a) Average horizontal component. (b) Vertical component.	39
Figure 35: Log ratios of surface motions to underground motions for the typical mining event MN2.6 on 11 May 2008, calculated for Fourier spectra of P- and S-waves. (a) Horizontal components. (b) Vertical components.	40
Figure 36: Log ratios of surface stations to underground stations for teleseismic event Mw7.9, 12 May 2008, Sichuan, China (Figure 25) calculated for Fourier spectra of average horizontal component (on the left) and vertical component (on the right). (a) For 1000 s records including P- and S-wave groups. (b) For P-wave group only (55 s).....	41
Figure 37: Log ratios of surface stations to underground stations for the regional event Mw5.4, 18 April 2008, Southern Illinois (Figures 28, 30 and 32) calculated for Fourier spectra of average horizontal component (on the left) and vertical component (on the right). (a) For S and Lg-waves (180 s). (b) For the P-wave package (90 s).....	42
Figure 38: Log ratios of surface stations to underground stations for the Georgian Bay regional event MN2.5, 5 February 2008 (Figures 29, 31 and 33) calculated for Fourier spectra of average horizontal component (on the left) and vertical component (on the right) including both S and Rg/Lg waves (40 s).	43
Figure 39: Mean log ratios of the surface station SSNO to underground station 46SNO. Error bars correspond to the standard deviations of these ratios. (a) From database of 73 teleseismic earthquakes ($\Delta > 3500$ km). (b) From database of 97 close local mining events ($\Delta = 8-40$ km).	44
Figure 40: Mean log ratios of the surface stations SSNO (upper line) and 11SNO (low line) to underground stations 46SNO (on the left) and DSNO (on the right) calculated from database of 97 close local mining events ($\Delta = 8-40$ km). Error bars correspond to the standard errors of these ratios.	45
Figure 41: Distribution of standard deviations over frequency for the mean log ratios shown in Figure 40. (a) Horizontal components. (b) Vertical components.	46
Figure 42: Mean log ratios of the surface stations SSNO (upper line) and 11SNO (low line) to underground stations 46SNO (on the left) and DSNO (on the right) calculated for 73 teleseismic ($\Delta > 3500$ km) earthquakes. Error bars correspond to the standard errors of these ratios.....	46
Figure 43: Distribution of standard deviation over frequency for mean log ratios shown in Figure 42. (a) Horizontal components. (b) Vertical components.	47
Figure 44: Mean log ratios (from the local events database) of (a) the surface stations SSNO and 11SNO and (b) underground stations 46SNO and DSNO. Error bars plotted correspond to the standard errors of these ratios.	47
Figure 45: Mean log ratios (from the distant events database) of (a) the surface stations SSNO and 11SNO and (b) underground stations 46SNO and DSNO. Error bars plotted correspond to the standard errors of these ratios. Designations are the same as in the previous figure.	48
Figure 46: Mean log ratios (from the 14 close local events database including NSNO records) of (a) SSNO/NSNO, (b) 11SNO/NSNO and (c) NSNO/DSNO. Error bars correspond to the standard errors of these ratios.	49

Figure 47: Mean log spectral ratios based on the data from three groups of local events. Ratios shown are (a) of the surface stations SSNO to underground stations 46SNO and DSNO, and (b) underground stations NSNO and DSNO. Error bars correspond to the standard deviation of these ratios.....50

Figure 48: Comparison of spectra of acceleration (corrected for instrument, cm/s^2) of signal (solid lines) and pre-event noise (dotted lines) calculated for the M2.1 blast that occurred on 4 May 2009 at 35 km distance from DSNO (left) and the typical mining event of MN2.6, 11 May 2008, at 23 km from DSNO (right). Vertical components are shown in blue, horizontal ones in red and green.....51

Figure 49: Mean log ratios of (a) the surface station SSNO and underground station NSNO, (b) underground stations NSNO and DSNO, and (c) underground stations 46SNO and DSNO, averaged over two blasts (# 96 and 97 in Table 4). Error bars plotted correspond to the standard deviation of these ratios.52

Figure 50: Mean log spectral ratios based on the data from five groups of regional events with increasing epicentre distances. Ratios shown are (a) of the surface stations SSNO to underground stations 46SNO, (b) of the surface stations SSNO to underground stations DSNO, and (c) underground stations 46SNO and DSNO. Error bars correspond to the standard deviation of these ratios.54

Figure 51: Log ratios of surface stations to underground stations for the event MN2.6 on 11 May 2008 (Figures 22 to 24 and Figures 34 to 35) calculated for response spectra of S-wave and P+S waves. (a) Average horizontal component, S-wave. (b) Vertical component, S-wave. (c) Average horizontal component, P+S-wave. (d) Vertical component, P+S-wave.55

Figure 52: Log ratios of surface stations to underground stations for the teleseismic event Mw7.9, 12 May 2008, Sichuan, China (Figures 25 to 27 and Figure 36) calculated for response spectra of the body waves group (1000 s). (a) Average horizontal component. (b) Vertical component.....56

Figure 53: Log ratios of surface stations to underground stations for the regional event Mw5.4, 18 April 2008, Southern Illinois (Figures 28, 30, 32 and 37) calculated for response spectra of acceleration of the 180 s record including S and Lg waves. (a) Average horizontal component. (b) Vertical component.56

Figure 54: Average ratios of response spectra of the surface station SSNO to underground station 46SNO. Error bars correspond to the standard deviations of these ratios. (a) From the database of 73 teleseismic earthquakes. (b) From the database of 97 close local mining events ($\Delta=8-40$ km).57

Figure 55: Average ratios of response spectra of the surface stations SSNO (upper two plots) and 11SNO (lower two plots) to underground stations 46SNO (on the left) and DSNO (on the right) for horizontal (red) and vertical (green) components of S-waves, from database of 97 close local mining events ($\Delta=8-40$ km). Error bars correspond to the standard errors of these ratios.....57

Figure 56: Distribution of standard deviation over frequency for average ratios of response spectra shown in Figure 55. (a) Horizontal components. (b) Vertical components.....58

Figure 57: Average ratios of response spectra of the surface stations SSNO (upper two plots) and 11SNO (lower two plots) to underground stations 46SNO (on the left) and DSNO (on the right) for horizontal (red) and vertical (green) components of S-waves,

from database of 73 teleseismic earthquakes ($\Delta > 3500$ km). Error bars correspond to the standard errors of these ratios..... 58

Figure 58: Average ratios of response spectra of the surface stations SSNO and 11SNO (on the left) and underground stations 46SNO and DSNO (on the right), from (a) the database of 97 nearby mining events ($\Delta = 8-40$ km), and (b) 73 teleseismic earthquakes ($\Delta > 3500$ km). Error bars correspond to the standard errors of these ratios. 59

Figure 59: Distribution of standard deviation over frequency for average ratios of response spectra shown in Figure 57. (a) Horizontal components. (b) Vertical components..... 59

Figure 60: Mean log spectral ratios averaged over 7 groups of events sorted by distance, for horizontal (left) and vertical (right) components. Error bars correspond to the standard errors of these ratios. In the legend, the range of epicenter distances is given for every curve with the number of events. (a) Ratios for SSNO station on the ground surface relative to the 46SNO station underground (1.4 km). (b) Ratios for SSNO station on the surface relative to the DSNO station underground (2.1 km). (c) Ratios between underground stations 46SNO to DSNO..... 62

Figure 61: Frequency-amplitude variability depending on the site location: vertical Z component of ground motion acceleration for the regional event Mw5.4, 18 April 2008, Southern Illinois (Figures 28, 30, 32, 37 and 53) at SNO and SUNO stations in three frequency bands, 0.5-1.5 Hz (left column), 1.5-4 Hz (central column) and 4-10 Hz (right column). (a) First 10 s of the P-wave. (b) The whole record including Pn, Sn and Lg wave-groups. Horizontal components (R and T) show similar amplifications..... 63

Figure 62: Frequency-amplitude variability depending on the site location: (a) vertical and (b) transverse components of ground motion acceleration for the typical mining event MN2.6 on 11 May 2008 at 5 SNO stations in three frequency bands, 0.5-3 Hz (left column), 3-6 Hz (central column) and 6-20 Hz (right column). Epicentre distance for DSNO station is 22.8 km as estimated by GSC (Table 4). 64

Figure 63: The MN2.1, 8 May 2008 mining event at 35.3 km from the SNO Lab. (a) Frequency-amplitude variability depending on the station depth; vertical components of ground motion acceleration in three frequency bands, 0.2-4 Hz (left column), 4-9 Hz (central column) and 9-20 Hz (right column). The stations names and their depths are given above the traces. (b) Log ratios of surface stations to underground stations calculated for Fourier spectra of average horizontal component (left) and vertical component (right) of S-waves..... 65

Figure 64: Records of the local Sudbury mining event MN2.1, 8 May 2008 (35.3 km distant from DSNO as determined from the GSC epicenter location) in the frequency band 0.2-10 Hz and their spectrograms. (a) vertical and (b) tangential components of acceleration at ground surface (SSNO station); (c) vertical and (d) tangential components of acceleration at 2.1 km depth (DSNO station). The time intervals on seismograms for surface stations, as selected by gray shading, represent the group velocity arrival time windows for (a) Rg (2.5 to 2.9 km/s) and (b) Lg (2.8 to 3.2 km/s)..... 66

Figure 65: Particle motion (velocity in radial-vertical plane) in the Rayleigh wave during 1.5 s (starting 5.1 s after P-wave arrival, see Figure 64) for the mining event MN2.1, 8 May 2008, in the 0.2-4.0 Hz frequency band, at ground surface (gray solid curve), at a depth of 1.6 km (thin black dotted curve), and at a depth of 2.1 km (thick black solid curve). Direction of movement indicated by arrows corresponds to retrograde particle motion. 67

Figure 66: Seismograms of the Lively earthquake recorded by six nearby regional stations (vertical (a,b) component and transverse (c,d) component) located at distances of 22-354 km from the source as determined from the GSC epicenter location. (a,c) 0.5-1.2 Hz frequency band. (b,d) 1.2-2.2 Hz frequency band. Marks show P and S body wave arrivals; Rg and Lg pick the maximal phase of surface waves in a given frequency range. The time intervals on seismograms, as selected by gray shading, represent the group velocity arrival time window 2.8 to 3.2 km/s (a,b) and 3.3 to 3.6 km/s (c,d).70

Figure 67: (a) Smoothed Fourier spectra and (b) spectral ratios of horizontal (T and R) and vertical (Z) components of acceleration (S and Rg/Lg waveforms), for the Lively earthquake (Figure 66) recorded by Canadian broadband stations at local and regional distances. Spectra are averaged over stations listed in the legend (their epicenter distances are given in the brackets). Spectra are corrected for instrument and geometrical spreading and reduced to 100 km.71

Figure 68: (a) Smoothed Fourier spectra and (b) spectral ratios of horizontal (T and R) and vertical (Z) components of acceleration (S and Rg/Lg waveforms), for the ML=3.8, 11 September 2008 at 11:21AM, h=1 km earthquake recorded by Canadian broadband stations at local and regional distances. Spectra are averaged over stations listed in the legend (their epicenter distances are given in the brackets). Spectra are corrected for instrument and geometrical spreading and reduced to 100 km.72

Figure 69: (a) Smoothed Fourier spectra and (b) spectral ratios of horizontal (T and R) and vertical (Z) components of acceleration (S and Rg/Lg waveforms), for the MN=3.8, 4 August 2004 at 11:55PM, h=3 km earthquake recorded by Canadian broadband stations at local and regional distances. Spectra are averaged over stations listed in the legend (their epicenter distances are given in the brackets). Spectra are corrected for instrument and geometrical spreading and reduced to 100 km.73

Figure 70: (a) Smoothed Fourier spectra and (b) spectral ratios of horizontal (T and R) and vertical (Z) components of acceleration (S and Rg/Lg waveforms), for the MN=4.3, 20 October 2005 at 9:16PM, h=11 km earthquake recorded by Canadian broadband stations at local and regional distances. Spectra are averaged over stations listed in the legend (their epicenter distances are given in the brackets). Spectra are corrected for instrument and geometrical spreading and reduced to 100 km.74

Figure 71: (a) Smoothed Fourier spectra and (b) spectral ratios of horizontal (T and R) and vertical (Z) components of acceleration (S and Rg/Lg waveforms), for the MN=4.0, 14 July 2006 at 9:34AM, h=5 km earthquake recorded by Canadian broadband stations at local and regional distances. Spectra are averaged over stations listed in the legend (their epicenter distances are given in the brackets). Spectra are corrected for instrument and geometrical spreading and reduced to 100 km.75

Figure 72: (a) Smoothed Fourier spectra and (b) spectral ratios of horizontal (T and R) and vertical (Z) components of acceleration (S and Rg/Lg waveforms), for the MN=5.4, 6 March 2005 at 6:17AM, h=13.3 km earthquake recorded by Canadian broadband stations at local and regional distances. Spectra are averaged over stations listed in the legend (their epicenter distances are given in the brackets). Spectra are corrected for instrument and geometrical spreading and reduced to 100 km.76

Figure 73: (a) Smoothed Fourier spectra and (b) spectral ratios of horizontal (T and R) and vertical (Z) components of acceleration (S and Rg/Lg waveforms), for the MN=4.5, 25 February 2006 at 1:39AM, h=19 km earthquake recorded by Canadian broadband

stations at local and regional distances. Spectra are averaged over stations listed in the legend (their epicenter distances are given in the brackets). Spectra are corrected for instrument and geometrical spreading and reduced to 100 km.77

Figure 74: Mean and standard deviation of apparent geometric spreading coefficient (b) from hypocentral distance $R = 3$ to 24 km, based on 20 shallow events that occurred within 5 km of SUNO, and were recorded at both SUNO and SNO surface stations. Assumes constant $Q = 400$. Average $b = 1.32 \pm 0.06$ 80

Figure 75: Example Fourier displacement spectra at the source ($R=1\text{km}$) for surface stations.....81

Figure 76: Kappa values determined from slope of log Fourier displacement versus frequency for each record (3-10 Hz).....82

1. INTRODUCTION

1.1 BACKGROUND

All existing ground-motion prediction equations that are applied in seismic hazard analyses apply to sites on the Earth's surface. To extend seismic hazard analyses and ground-motion estimates to sites underground, information on the relationship between motions underground and those on the surface is required. A key objective of this study is to determine how ground motions recorded in underground cavities compare with those on the Earth's surface.

Seismic motions underground have been studied by many authors since the pioneering study of Kanai and Tanaka (1951) in the Hitachi mine in Japan, which documented amplification of seismic wave motions on the surface relative to those underground (up to 450 mbgs). Numerous experiments involving borehole *in situ* observations made at different levels within a soil column and in the bedrock below have been conducted to improve understanding of the effects of a shallow soil column on ground motion, and to quantify the observed amplification and attenuation effects of near-surface formations on incident seismic motion (Blakeslee and Malin, 1991; Fukushima et al., 1995; Kinoshita, 1999, 2008; Graizer et al., 200; Okada et al., 2004; Yamanaka et al., 2004; Lida et al., 2005 and many others). Site response studies using deep underground records under conditions similar to those of the PUPS experiment in the Gran Sasso Massif in Abruzzo in Central Italy (1.4 km depth) (De Luca et al., 1998) and in the Tangshan Area in China (0.8 km) (Matsunami et al., 2003) also have shown that the ground motion intensity at depth is less than that at ground surface. In general, an amplification of at least two on the surface is expected, due to the free-surface effect (with some caveats), but observed surface amplification may be much larger due to amplification of amplitudes through the near-surface materials. For example, site transfer functions evaluated with respect to underground sites in Gran Sasso show an amplification factor of as much as 6 in the 1–8 Hz frequency range (De Luca et al., 1998), which is attributed to a combination of the free-surface effect and resonance effects in the surface layers.

In this study, amplification for surface stations located on hard rock (glaciated norite and granitic rocks) is addressed, relative to stations located in similar rock material at depths of more than 1 km. It is known that near-surface weathering and jointing tends to reduce near-surface shear-wave velocities, even for hard rock sites such as those in Sudbury. For example, typical hard rock sites in eastern North America (ENA) have surface velocities in the range of 2.5 to 3 km/s, while velocities at a depth of a few km are about 3.5 km/s (Beresnev and Atkinson, 1997). The near-surface gradient acts to amplify seismic waves, with the amplification being an increasing function of frequency (Boore and Joyner, 1997). On the other hand, the increased cracking and weathering near the surface disrupts high-frequency motions and leads to greater energy absorption. There is thus an offsetting factor to the amplification by the velocity gradient, which is typically modelled by the high-frequency decay parameter, κ (Anderson and Hough, 1984); the interplay between these two factors could, in general, lead to either smaller or larger motions being recorded underground.

Conservation of energy requires amplification by a factor of two in seismic wave amplitudes when waves traveling through the earth encounter a free surface. This amplification may not apply in this experiment, as the underground stations are within caverns and thus have their own "free surface". However, the typical dimension of the underground facilities where the seismometers are installed is only 5-10 m for the shafts and 20-50 m for the SNO lab cavity, which is small relative to the wavelengths of the signals being analyzed (300-30,000 m); thus

the underground caverns are expected to be essentially invisible in the main frequency band analyzed (about 0.1-10 Hz). On the other hand, in the case of *SV* and *P* waves, the free surface effect is more complex, and for oblique incidences, surface amplitudes may even be smaller than those at depth (Shearer and Orcutt, 1987; Fukushima et al., 1995). Furthermore, the transfer function between the free surface and a point at depth in a half-space will generally be frequency-dependent. Finally, one might also expect to see some de-amplification at the deeper stations due to the rapid attenuation with depth of any surface wave contributions to the seismic signals.

In summary, given the number of factors involved, it is difficult to predict the motions one would expect in underground caverns based on observations on the surface, even when the surface observatories are located on hard rock. This study provides valuable empirical information on the seismic motions that should be expected for underground caverns, relative to those predicted by seismic hazard studies conducted for the surface.

1.2 POLARIS UNDERGROUND PROJECT AT SNO (PUPS)

The POLARIS Underground Project at SNO (PUPS) takes advantage of the unique 3-dimensional geometry offered by the SNO lab, located at a depth of 2 km beneath the Vale Creighton Mine in Sudbury, Ontario, and its access tunnels through Shaft #9. Figure 1 presents a cross-section (SE-NW-vertical) of the mine (imported from the SNO lab site <http://sno.phy.queensu.ca>) with the location of ore bodies indicated by the yellow fields. This is a schematic picture showing the relative location of the main geological features, mine shafts, SNO lab and its surface facilities, which include a major laboratory building near the head of Shaft #9. The approximate positions of stations were added to this schematic as red circles.

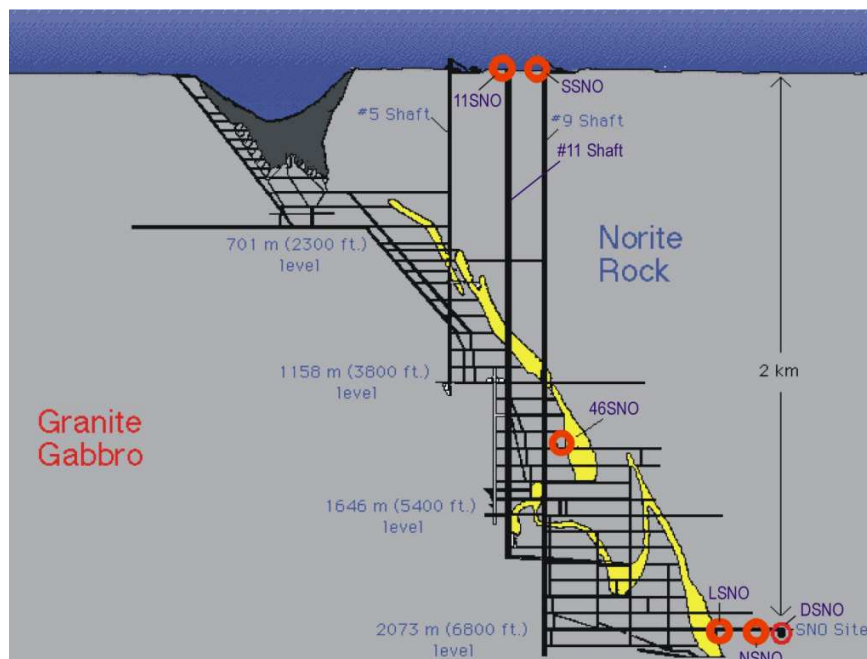


Figure 1: Vertical (SE-NW direction) rough scheme of SNO Lab location (<http://sno.phy.queensu.ca>). Surface facilities are located near the head of Shaft #9. The full horizontal distance from the Shaft #9 to SNO is about 2 km. Approximate positions of stations are shown by the red circles.

The Vale Creighton Mine is located at the southeastern corner of the elliptical Sudbury Igneous Complex (60 km long by 30 km wide, see Figure 2), in the area of the massive sulphide ore zone between the main mass norite and footwall granite gabbro domains (Malek et al, 2008). The genesis of the Sudbury structure is a major meteorite impact about two billion years ago (Moon and Jiao, 1998). Results of the Lithoprobe AGT high-resolution seismic reflection survey (Boerner et al., 1994) revealed an extremely asymmetric geometry of the Sudbury Basin at depth (Milkereit et al., 1992; Wu et al., 1995; Boerner et al., 2000). Reconnaissance seismic surveys have shown that the South Range of the Sudbury structure consists of two steeply dipping (>45°) reflections; the north-dipping contact between norite and the footwall complex is truncated at about 3,000-m depth by a south-dipping shear zone, corresponding to the underlying footwall of granite and greenstone (Milkereit et al., 1996).

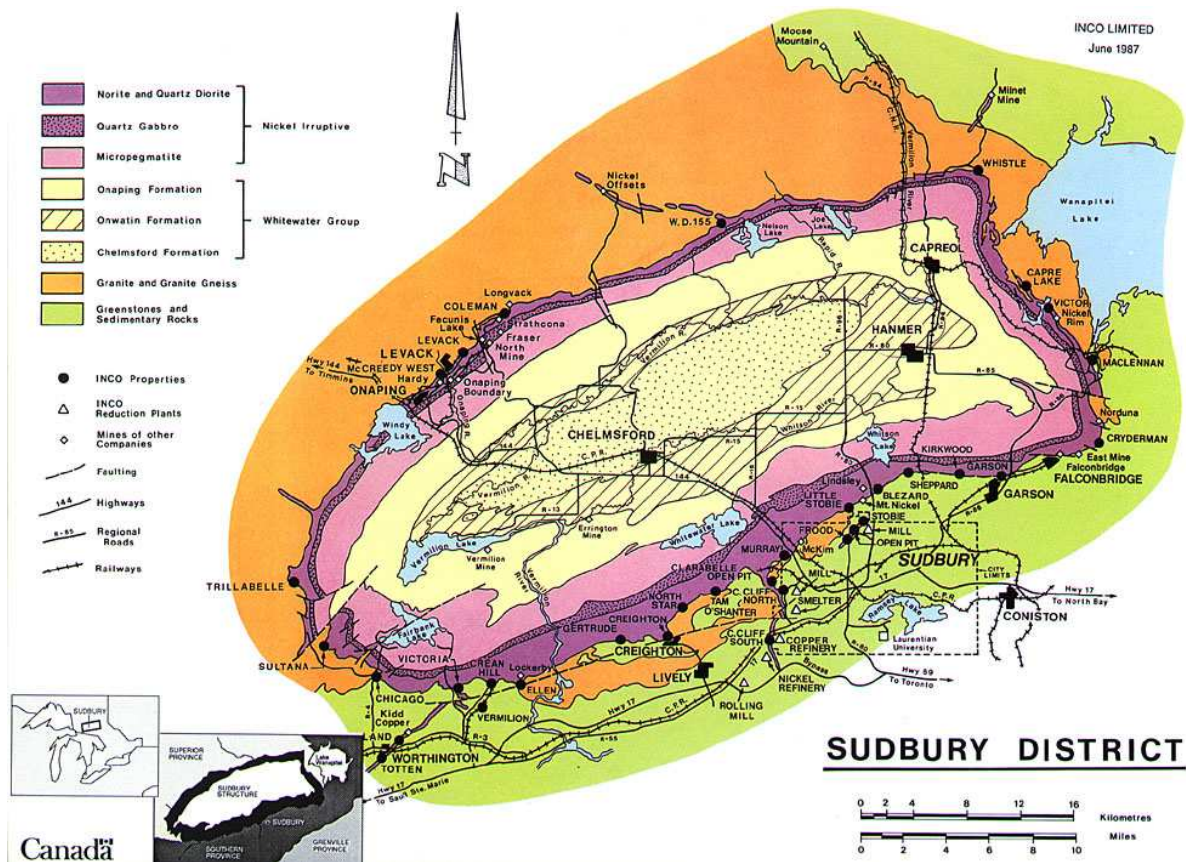


Figure 2: Simplified geological map of the Sudbury Basin.

Data from composite logs from different boreholes (Milkereit and Eaton, 1998; Boerner et al., 2000), and laboratory studies of drill core samples (Salisbury et al. 1994), show significant variability in material properties across the structure (14% variability in density and 24% in P-wave velocity). Finally note that there is not yet a comprehensive published model of the Sudbury structure that would integrate all the available data and conflicting interpretations (Boerner et al., 2000) in such a way as to provide a structure and velocity model for quantitative site effect analysis at SNO.

Five portable Taurus seismograph units obtained from the POLARIS Consortium, each with

3-component broadband seismometers sampling at 200 samples/second, were installed in the following locations (see Figure 1 and Figure 3, Table 1):

1. Station DSNO - Within the SNO lab at 2073 m depth (6800 ft). This is a modern lab facility, with on-site internet access.
2. Station LSNO - At the SNO 2073 m level (6800 ft), at a location along the drift between the lab and shaft #9. On November 5, 2008, this station was moved to a new location near the new SNO lab, and renamed NSNO.
3. Station 46SNO - At the 1402 m level (4600 ft), within the SNO satellite lab.
4. Station SSNO - A short distance from the SNO Lab building on the surface. This location has internet access.
5. Station 11SNO - On the surface, near shaft #11.

Table 1: Seismograph Station coordinates

Code	Latitude, Grad	Longitude, grad	Depth, km
SSNO	46.47151	-81.18707	0
11SNO	46.46831	-81.1986	0
46SNO*	46.47333	-81.19167	1.4
LSNO	46.47036	-81.20877	2.1
NSNO	46.47728	-81.21063	2.1
DSNO	46.47546	-81.218247	2.1
SUNO	46.64380	-81.3442	0

* approximate estimate

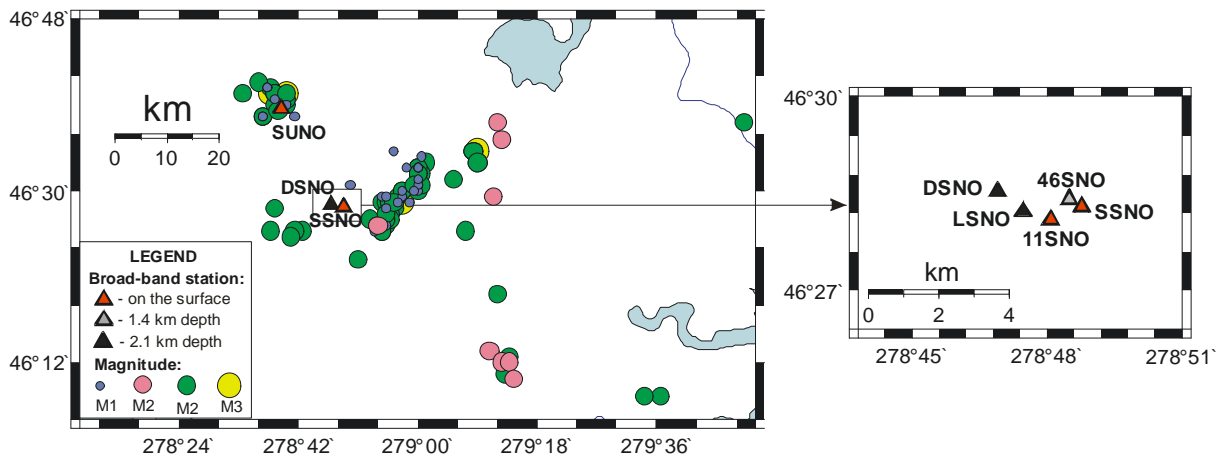


Figure 3: Map showing local event epicentres and stations locations. The pink filled circles correspond to the group of 8 mining events used for the full frequency band (0.5-100 Hz) spectral ratio analysis.

All stations had power access and were supplied also by battery power for continuous functioning during electricity shutdowns. Only two stations, DSNO and SSNO, had internet access, and only surface stations had a GPS connection with satellites. The other sites (LSNO,

NSNO, 46SNO and 11SNO) used internal clocks with inherent drifts in timing. The sites were all within, or on, hard rock. The vertical sensor axis of every seismograph is oriented in the 'up' direction, while the other two axes were oriented perpendicularly to it in the horizontal plane, arbitrarily relative to a meridian.

The installations were made possible through the cooperation of the SNO Lab and Inco. Figure 3 shows the station locations along with local seismic events observed during the whole period of the PUPS project (August 2006-October 2009). Epicentres were located by the Geological Survey of Canada (GSC). The PUPS project concluded in 2009, with all instruments being removed in October 2009.

During the more than three years of operation, PUPS recorded local, regional and teleseismic events, in an effort to better understand, at least from an observational perspective, the extent to which seismic signals are influenced by near-surface site and path effects for hard rock sites. Most seismographic stations in eastern Canada are located on hard rock sites; thus an understanding of near-surface effects is important in order to properly interpret observed earthquake ground motions across the network and their engineering implications. Furthermore, the work is important to seismic hazard estimation for underground storage facilities, in particular proposed facilities for nuclear waste storage. By comparing signals observed on the surface to those at subsurface locations, empirical models of rock site response may be developed and evaluated in terms of gross rock properties and other factors. SNO was selected for this study because of its deep underground caverns that are readily accessible. Moreover, using a combination of signals recorded at SNO and on nearby national stations, in particular SUNO (20 km away, at Sudbury), provides an opportunity to perform a study of attenuation near the earthquake source and earthquake source/site properties, such as 'kappa' and stress drop (see sections 3.6, 4.1 and 4.2).

Note that the lack of detailed information on material properties, combined with timing limitations of underground stations due to the lack of GPS beneath the surface, limit the potential scope of our investigations by observational studies, and precludes detailed theoretical modelling of the signals.

Figure 4 shows the transfer functions of the SNO and SUNO seismic stations (SNO station SSNO is selected for the plot; all SNO stations have identical responses). The transfer function of the SNO stations, equipped with the Trillium 120P sensor, is approximately flat from 100 s to 10 Hz, with a narrow maximum (amplification by a factor of 2.3) at frequency (f) 40 Hz, and a roll-off at 40 DB/decade below the lower corner frequency, as shown in Figure 4. The SNO stations sample at 200 samples/sec. The SUNO 3-component broadband station, equipped with the CMG3ESP-POLARIS sensor, does not have the high-frequency peak in response; its response is approximately flat between 100 s and 40 Hz. The SUNO sampling rate is 100 samples/second.

For this study, all events sufficiently distant from stations (such that the signals could be described as 'far-field') that are recorded strongly (signal well above noise), at both underground and surface sites, are processed and analysed. Signal processing for each event at each station involves: (i) the transformation of recorded signals from the time domain to the frequency domain; (ii) the removal of instrument response to obtain absolute ground-motion amplitudes; (iii) the estimation of signal to noise to determine the appropriate frequency range for analysis; and, (iv) the application of a noise-suppressing filter. The analysis is focused on the frequency domain representation of site effects and other ground-motion characteristics.

Attention was restricted to 'far-field' signals to avoid any significant complications that can occur in signal processing for events sufficiently close to recording stations (i.e., to cause a permanent displacement offset). These issues are described in more detail in Section 2.2.

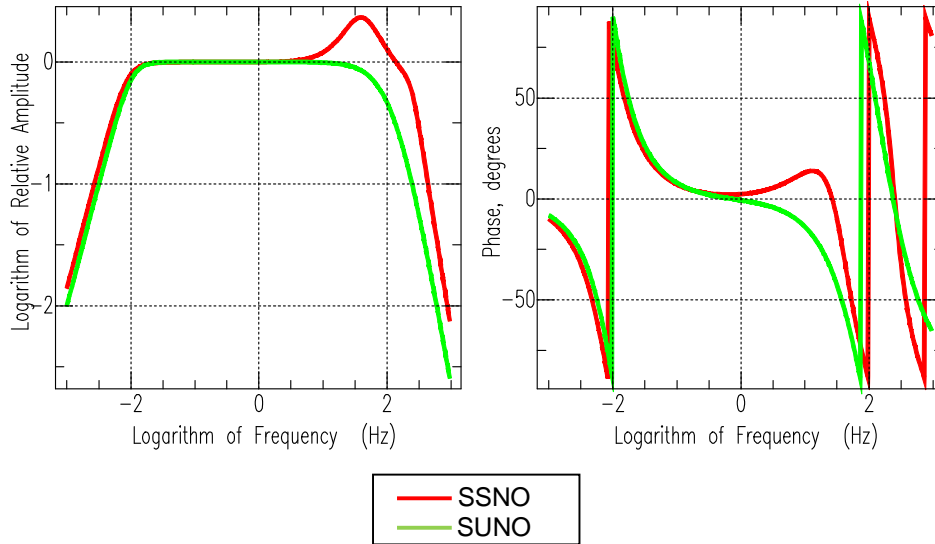


Figure 4: Nominal frequency response of SSNO station (red) and SUNO station (green).

2. DATA ANALYSIS

2.1 QUALITY-CONTROL OF DATA

The simplest way to do rough verification of input broadband data, and to exclude evident data errors, is to first analyze typical noise signals recorded by the stations and compare their spectra among stations. Common terminology in the field is used here, and thus the long-period ($T > 1$ s) ambient noise are defined as "microseisms", while the short-period ($T < 1$ s) ambient noise are referred to as "microtremors"; note that microseisms are of natural origin, while microtremors are mainly of artificial origin (Bard, 1999).

Natural ambient long-period seismic noise is mostly composed of surface waves that originated close to the surface of the Earth. Primary and secondary microseisms have periods similar to the main sea-swell period and half period, respectively; they are related to the interaction of the sea waves with the sea bottom and coast due to acoustic resonance provided by wave-to-wave interactions (Longuet-Higgins, 1950; Gutenberg, 1951; Kedar et al. (2008)).

Far from the shoreline, this wavefield is stable and, when no earthquake or other sources are active, must have the same spectral amplitudes at all SNO and SUNO stations because the depth of penetration of surface waves at $T = 5$ s is much more than 2 km (Soczkiewicz, 1997). An illustration is provided in Figure 5. The secondary microseism peak at 5 s is clearly recognized here, and has the same amplitudes for all 5 stations. It can be concluded that, in the first approximation, all 5 stations worked correctly at the time covered by Figure 5, at least during the periods analyzed.

Because the SNO seismic network is located in a working mine, the stations record high-frequency microtremors, which are in general different for every location within the mine. However, there was an electricity disconnection made on November 11, 2007 that provided a period free from mining noise, allowing an opportunity to estimate the minimal basic level of ambient noise at the stations. Figure 6 presents the smoothed Fourier amplitude spectra of 2 hr vertical records of noise made during this activity-free period in the INCO mines, when power and all machines and communications were stopped, in comparison to spectra for the next day, after the power was reconnected and normal activity resumed (Figure 6b). All three underground stations have very similar spectra at frequencies less than 30 Hz during the power outage (Fig. 6a), whereas the surface station 11SNO demonstrates 3-4 times higher noise at 1-30 Hz. It is remarkable that the secondary microseismic peak again has the same amplitudes at the underground and surface station 11SNO. Figure 6 shows also that the SSNO station (magenta curve) worked incorrectly; note how its long period amplitudes are depressed. Study of noise spectra at SSNO has shown that this station worked incorrectly during the period between two 'restarts', from October 1, 2007 to December 12, 2007. In general, noise studies have been very useful in identifying time periods during which instrument malfunctions occurred.

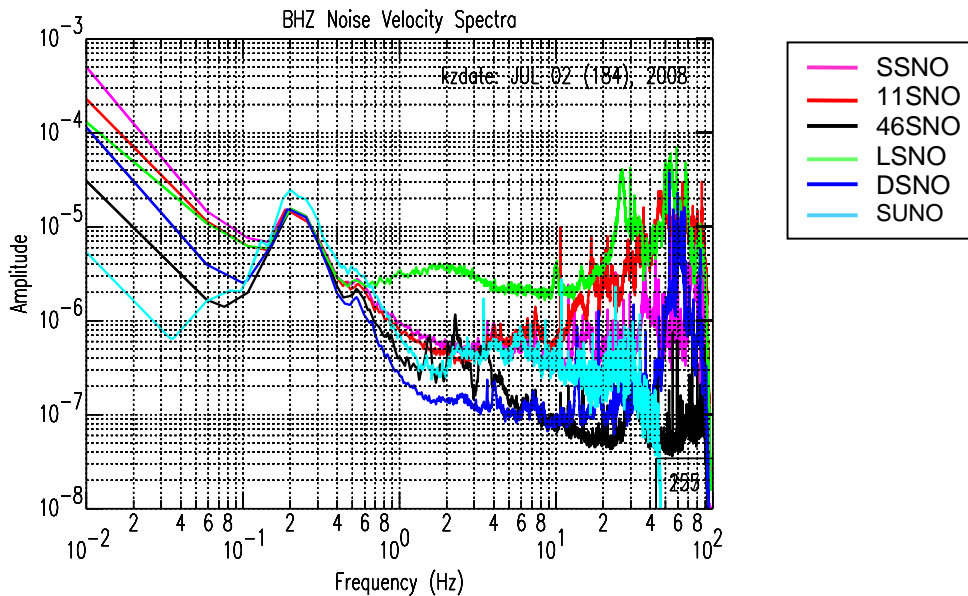


Figure 5: Typical Fourier amplitude spectra smoothed and corrected for instrument, of vertical component of ambient noise recorded on 2 July 2008 by 5 SNO stations and the SUNO station. Amplitude corresponds to velocity in m/s.

Additionally, incorrect seismograph operation was sometimes observed (opposite to that of SSNO, see Figure 6). Figure 7 provides such an example for station 46SNO. It worked incorrectly between two starts of the system: August 17 and November 7, 2006. The low frequency part of the spectra of ambient noise on the 46SNO sensor was amplified in comparison to all other stations.

Figure 8 demonstrates transfer function problems at DSNO station detected in the period between two system restarts on November 8, 2006 and May 22, 2007. Fourier spectra presented here are calculated for 82 min vertical records of ambient noise recorded November

29, 2006, just before the Lively earthquake of MN4.1. Due to unknown reasons, the transfer function of the DSNO station was far from nominal at all frequencies, so that seismograms of signals recorded by this station at that time had one-sided impulse forms. For comparison, see Figure 9, comparing the spectra of a mining event of MN2.1 that occurred 25 km away from the SNO Lab on November 20, 2006 and was recorded by 5 SNO stations, along with ambient background noise. As in the previous case documented for the SSNO station, the DSNO seismometer began to work incorrectly just after restarting. This is unfortunate as it means that the DSNO signals recorded very near the Lively earthquake (Atkinson et al., 2007) are not reliable.

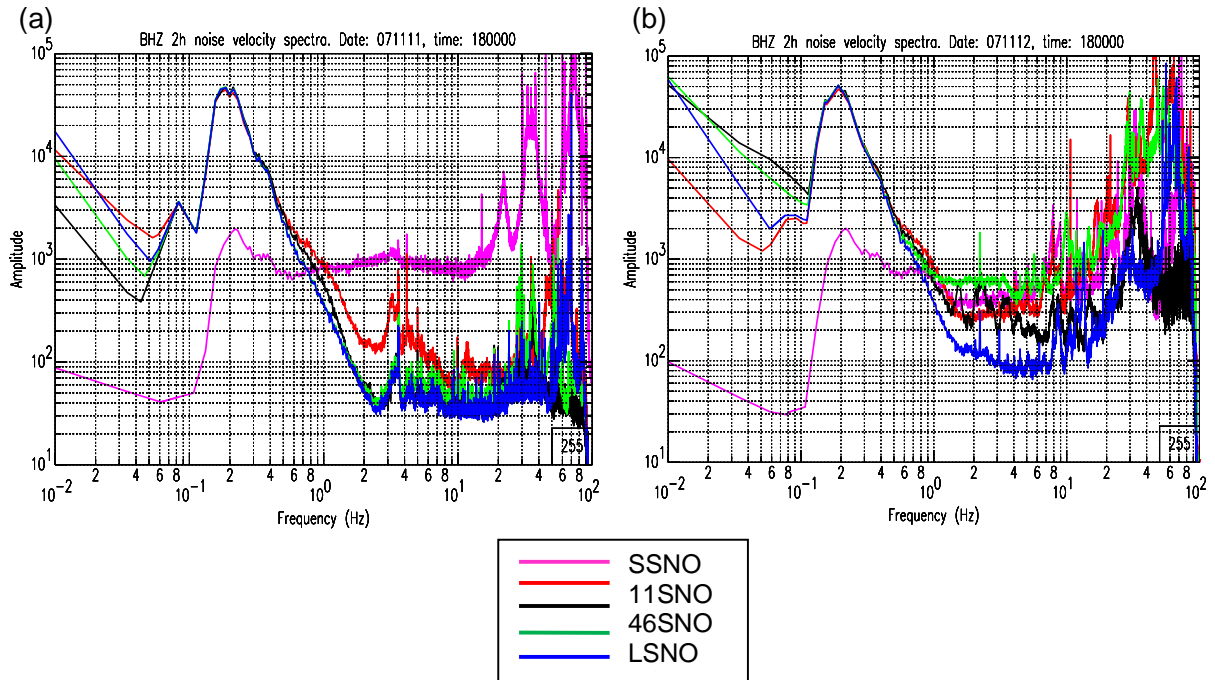


Figure 6: Fourier amplitude smoothed spectra of 2-h vertical records of ambient noise observed by 5 broadband SNO stations: (a) 11 November 2007 during electricity disconnection; (b) 12 November 2007, the next day after electricity was reconnected.

In general, the instrument problems took place between two consequent restarts of the system, or were caused by unauthorized moving of a station during operation (by mining personnel). During one visit to the SNO Lab on November 5, 2008, it was observed that the DSNO station (in the Clean Lab) was moved so that its level was far from center, and the station had subsequently self-restarted. Analysis of data has shown that this move happened on September 18, 2008 at about 15:45 GMT. After that, a large baseline shift was causing overflow of the disk with loss of data and the system self-restart. Fortunately, data of this station transmits to GSC via Internet, so that data at DSNO between the two service visits of June 16 and November 5, 2008 were not all lost. However, interruption of internet connection and occasional losses of power have resulted in some data loss. Ambient noise spectra (corrected for instrument) recorded by the unlevelled DSNO station that time is presented in Figure 10 (dark blue curve) in comparison with spectra of other stations.

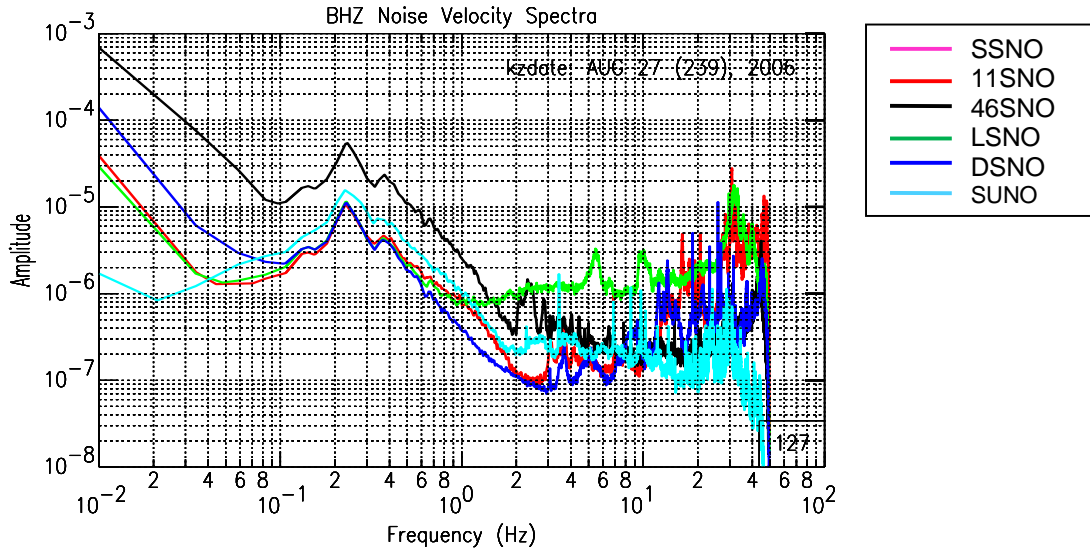


Figure 7: Fourier amplitude spectra of ambient noise (corrected for instrument) recorded on 27 August 2006. Station 46SNO (black line) worked incorrectly at this time.

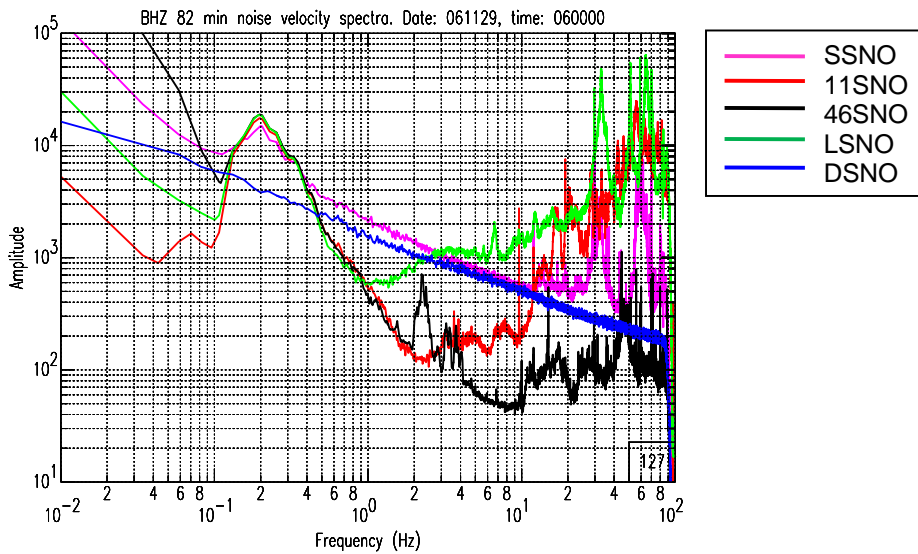


Figure 8: Fourier amplitude smoothed spectra of 82 min vertical records of ambient noise registered by 5 broadband SNO stations 29 November 2006, just before the Lively earthquake MN4.1. Note the problem with DSNO (blue).

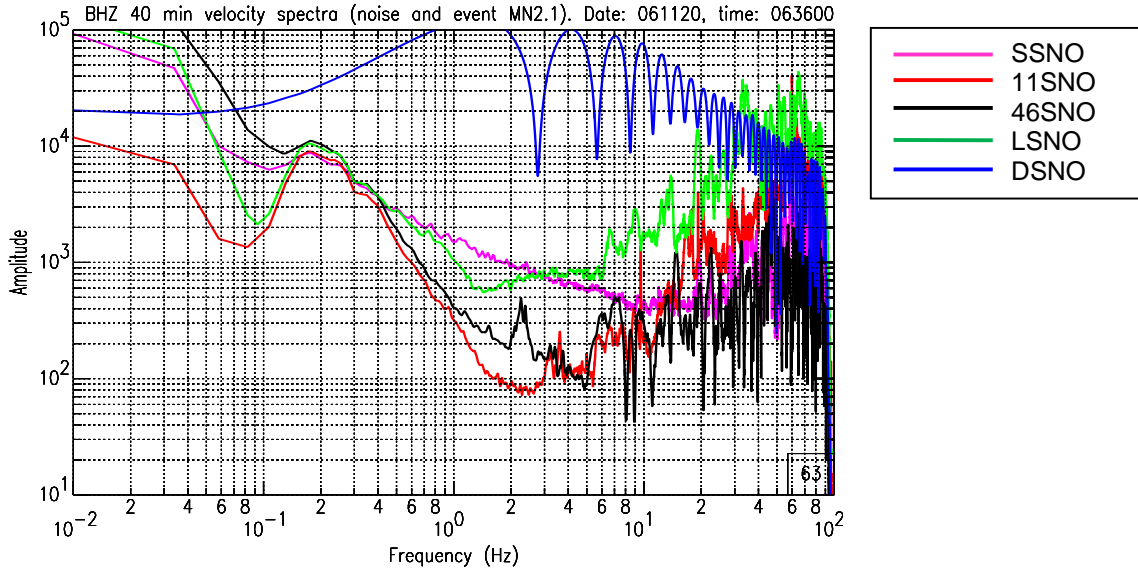


Figure 9: Fourier amplitude smoothed spectra of 40-minute vertical records of ambient noise and a mining event MN 2.1 observed by 5 broadband SNO stations 20 November 2006. Note the problem with DSNO (blue).

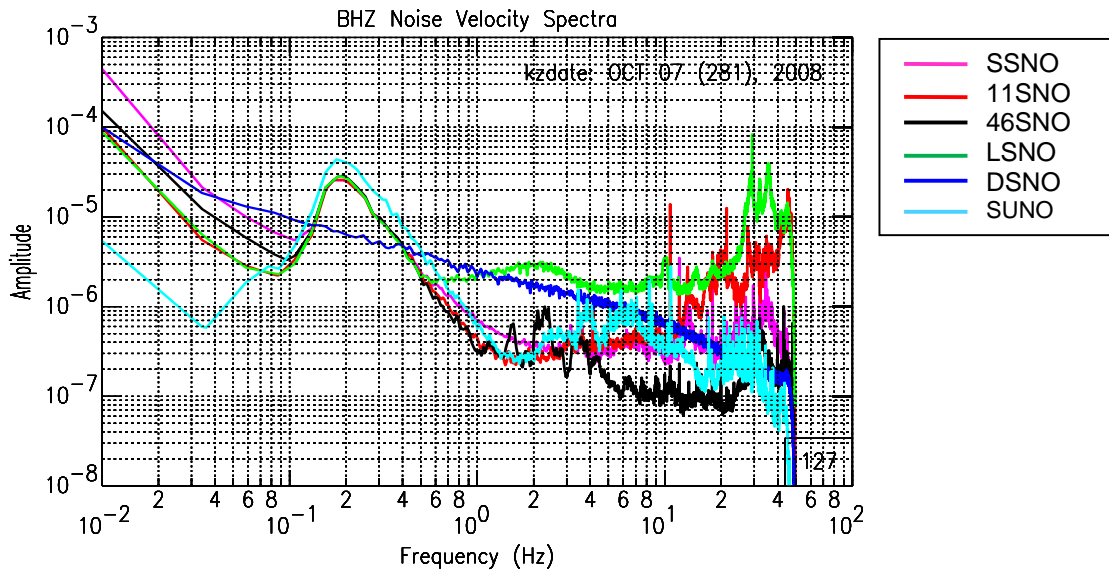


Figure 10: Comparison of ambient noise spectra (corrected for instrument) recorded by the unlevelled DSNO station (dark blue curve) and other stations working as usual, 7 October 2008.

To summarise, two types of incorrect operation of seismometers were observed over the course of the experiment: (i) when the Fourier velocity amplitude spectrum of ambient noise had the form of a line that sloped downwards with increasing frequency; and (ii) when the spectrum was amplified or depressed at low frequencies <1 Hz. The first problem was most likely due to improper levelling and mass centering of a sensor, while the reason of the second type of distortion is unclear. After removing erroneous and suspect data, the available data is

as given in Table 2, over the PUPS project. During other time periods, the data are either unreadable, or suffer from apparent errors in instrument response, as indicated by noise analyses.

Table 2: Summary of data availability (excluding erroneous or suspect data)

Station's Code	Time of data availability (error-free periods) dd/mm/yy					
11SNO	24.08.2006-14.09.2006	06.11.2006-10.02.2007	10.02.2007-22.05.2007	22.05.2007-01.10.2007	01.10.2007-10.12.2007	10.12.2007-17.06.2008
SSNO		07.11.2006-22.05.2007		22.05.2007-01.10.2007		12.12.2007-18.06.2008
46SNO		07.11.2006-13.02.2007	13.02.2007-23.05.2007		02.10.2007-10.12.2007	10.12.2007-17.06.2008
DSNO	16.08.2006-08.11.2006		12.02.2007-01.04.2007	01.04.2007-03.10.2007	03.10.2007-11.12.2007	11.12.2007-16.06.2008
LSNO	24.05.2006-08.11.2006	08.11.2006-12.02.2007	12.02.2007-06.05.2007	22.05.2007-03.10.2007	03.10.2007-11.12.2007	13.12.2007-16.06.2008
11SNO	17.06.2008-04.11.2008	04.11.2008-15.04.2009	15.04.2009-05.10.2009			
SSNO	18.06.2008-04.11.2008	04.11.2008-15.04.2009	15.04.2009-05.10.2009			
46SNO	17.06.2008-04.11.2008	04.11.2008-15.04.2009	15.04.2009-07.10.2009			
DSNO	16.06.2008-18.09.2008	05.11.2008-16.04.2009	16.04.2009-08.09.2009			
LSNO	16.06.2008-03.11.2008					
NSNO		05.11.2008-14.02.2009	16.04.2009-06.10.2009			

The horizontal components of the SNO stations are arbitrary in their orientation, as direction (east, west, etc.) is not readily determined underground. Direction is not important for studies involving the random or average horizontal component. For some applications, however, it can be useful to know the actual directions of the so-called "EW" and "NS" components. To find these directions, particle-motions corresponding to the long-period first motions of the P-waves that arrived from a few very strong teleseismic earthquakes were calculated and compared with records made by the SUNO station 20 km distant. Correction angles were found as the difference between back azimuths estimated from observations at SUNO and PUPS stations, averaged through several events. This allowed for determination of the actual orientation of the "EW" and "NS" components at each underground station. These orientations are given in Table 3, listing the actual angles of the components labelled "EW" and "NS".

As already noted, there is an additional difference between the SNO stations and most networks: underground stations do not have exact time, because GPS signals from satellites cannot be captured by the systems underground. The time shifts for every station can be determined approximately using strong teleseismic events. These estimations are sufficient for record identification purposes, but are too rough for event location using standard techniques based on time delays. The use of relative geometry of the directions of P-wave polarization

observed at a few stations can give the real location of small mining events which are too weak to be recorded by the regional network.

Table 3: Actual orientation of horizontal channels of SUNO and PUPS stations

Code of station	before 4-5 Nov 2008		after 4-5 Nov 2008	
	Azimuth of NS-axis degrees	Azimuth of EW- axis Degrees	Azimuth of NS-axis degrees	Azimuth of EW- axis Degrees
SSNO	334	64	342	72
11SNO	149	239	359	89
46SNO	61	151	70	160
LSNO	295	25		
NSNO			111	201
DSNO	287	17	293	23
SUNO	0	90	0	90

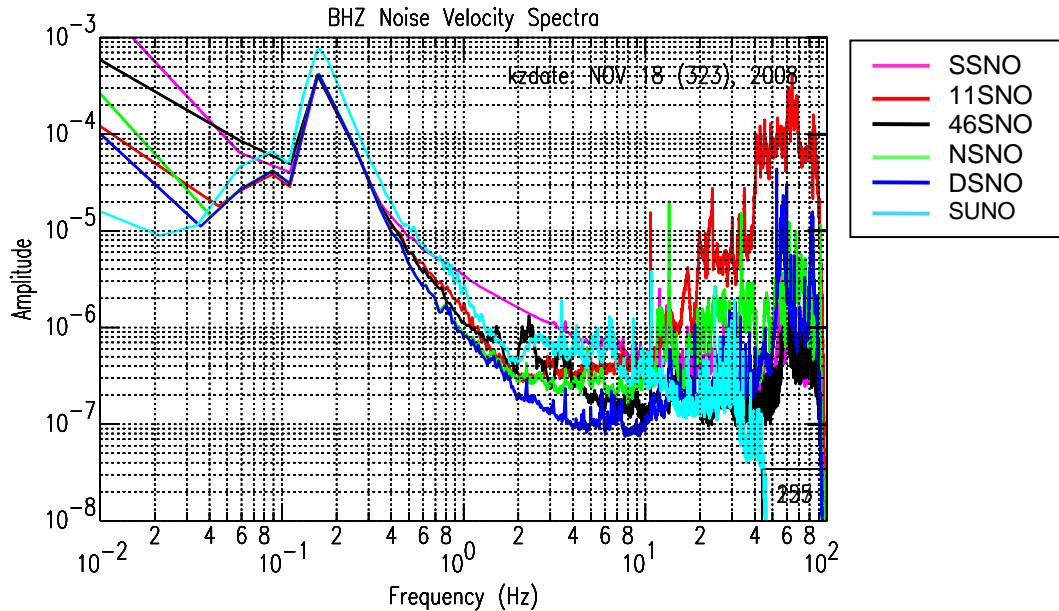


Figure 11: Ambient noise spectra (corrected for instrument) recorded by SNO and SUNO stations on 18 November 2008, two weeks after installation of the NSNO station (green line).

Analysis of ambient noise spectra resulted in the conclusion that the noisiest station is LSNO. It continuously recorded strong and very broadband (0.5-80 Hz) mining activity noise. The only way to improve data quality of the LSNO station was to relocate it to a quieter site. After long negotiations with SNO and Vale Canada Limited (Vale) to allow relocation, the LSNO station was moved on November 5, 2008 to the relatively quiet tunnel leading to the new clean SNO Lab under construction and was renamed NSNO. The standard microtremor spectra recorded by NSNO and other stations is presented in Figure 11. In general, this station remained noisier than its nearest neighbour DSNO, but the level of this noise relative to DSNO was almost by an

order of magnitude better than it was at LSNO. After this relocation, the noisiest station was 11SNO (due to its proximity to the shaft transporting waste rock on the surface), but SNO and Vale authorities could not offer a better surface placement with a power connection.

2.2 DATABASE

All events recorded by the SNO stations can be divided into a few broad categories, each of which dictates different approaches for data processing. Nearby local events (<40 km) provide a good picture of motions at intermediate to high frequencies (>1 Hz), while very distant large global events (teleseisms) may be able to provide some constraints at long periods (<1 Hz).

The most useful local events in the database are 106 small events with magnitudes ranging from 1.4 to 3.8 MN (where MN is the Nuttli (1973) magnitude), for which there are two or more records at SNO stations, as listed in Table 4 and shown in Figure 3. The events were recorded between August 2006 and October 2009, and include mining events around the SNO Lab located at epicentral distances of 1-100 km.

Table 4: Local events within 100 km of DSNO station (46.47500, -81.20111), August 2006 - October 2009

N	Date dd/mm/yyyy	Time (UT)	Latitude	Longitude	Distance, km	Mag MN	Category
1	24/08/2006	21:50:51	46.47	-81.36	12.2	2.8	C13
2	24/08/2006	23:04:26	46.49	-81.09	8.7	1.7	C13
3	28/08/2006	15:39:07	46.44	-81.08	10.1	1.4	C12
4	01/09/2006	08:09:49	46.65	-81.36	23.0	2.2	C13
5	02/09/2006	00:00:25	46.49	-81.04	12.4	1.8	C13
6	06/09/2006	19:01:31	46.50	-81.00	15.7	1.4	B1
7	17/09/2006	00:29:09	46.48	-81.06	10.9	2.4	D123
8	18/09/2006	05:23:27	46.51	-81.17	4.6	1.4	D123
9	25/09/2006	06:14:23	46.65	-81.33	21.8	1.7	D123
10	03/10/2006	23:54:43	46.48	-81.09	8.6	2.8	D123
11	21/10/2006	00:24:05	46.65	-81.33	21.8	2.2	D123
12	22/10/2006	22:50:05	46.45	-81.12	6.8	2.7	D123
13	22/10/2006	22:57:14	46.47	-81.08	9.3	1.9	D123
14	22/10/2006	22:59:49	46.43	-81.11	8.6	1.4	D124
15	24/10/2006	22:37:10	46.52	-80.91	22.9	2.3	C12
16	25/10/2006	00:05:08	46.68	-81.37	26.2	2.5	D123
17	20/11/2006	04:51:25	46.67	-81.36	24.9	2.1	C45
18	29/11/2006	08:31:59	46.48	-81.05	11.6	1.8	D145
19	29/11/2006	08:34:05	46.50	-81.04	12.7	1.7	D145
20	14/12/2006	13:32:13	46.63	-81.31	19.1	1.9	B5
21	21/12/2006	06:50:48	46.50	-81.00	15.7	2.4	C56
22	23/12/2006	12:12:18	46.52	-81.00	16.2	2	C56
23	31/12/2006	22:41:02	46.48	-81.08	9.3	2.1	B5
24	02/01/2007	06:46:41	46.48	-81.07	10.1	2.5	B5
25	02/01/2007	06:47:27	46.38	-81.15	11.3	2.2	B5
26	02/01/2007	07:48:20	46.48	-81.02	13.9	1.5	D145
27	02/01/2007	12:26:06	46.48	-81.07	10.1	2.1	B5
28	07/01/2007	12:34:31	46.67	-81.36	24.9	2	C56
29	11/01/2007	13:00:25	46.49	-81.08	9.4	1.9	B5

N	Date dd/mm/yyyy	Time (UT)	Latitude	Longitude	Distance, km	Mag MN	Category
30	24/01/2007	02:58:45	46.55	-80.85	28.2	2.3	B5
31	26/01/2007	16:37:07	46.63	-81.39	22.5	1.8	C45
32	12/02/2007	08:27:43	46.54	-81.00	17.0	2.8	B5
33	17/02/2007	22:31:23	46.46	-81.07	10.2	2	A
34	08/03/2007	00:30:02	46.47	-81.06	10.9	2.7	A
35	09/03/2007	22:20:23	46.43	-81.37	13.9	2.8	A
36	21/03/2007	22:50:50	46.51	-81.00	16.2	1.5	B5
37	24/03/2007	00:02:52	46.54	-81.00	17.0	1.6	B5
38	13/05/2007	02:13:08	46.69	-81.40	28.3	2.8	C45
39	14/06/2007	12:01:24	46.67	-81.36	24.9	2.6	B3
40	22/06/2007	14:24:41	46.63	-81.39	22.5	1.8	C23
41	07/08/2007	12:18:34	46.54	-81.00	17.0	2.1	B3
42	28/08/2007	10:17:32	46.54	-81.03	15.0	1.5	D234
43	02/09/2007	09:21:49	46.66	-81.36	23.9	1.7	B3
44	02/10/2007	22:55:28	46.49	-81.05	11.7	2.6	B1
45	05/10/2007	11:17:53	46.54	-81.00	17.0	1.8	B1
46	09/10/2007	07:38:42	46.54	-81.00	17.0	1.6	B1
47	28/11/2007	13:27:35	46.67	-81.33	23.8	3	B1
48	01/01/2008	04:25:01	46.46	-81.07	10.2	2.6	B6
49	05/01/2008	08:58:51	46.57	-81.06	15.1	1.8	C46
50	21/02/2008	23:58:00	46.67	-81.44	28.4	2.4	A
51	25/02/2008	21:59:12	46.57	-80.86	28.2	2.3	A
52	05/03/2008	02:42:21	46.63	-81.39	22.5	2	B4
53	13/03/2008	04:25:43	46.44	-81.08	10.1	2.4	A
54	25/03/2008	16:26:35	46.50	-81.04	12.7	2	A
55	25/03/2008	16:17:16	46.50	-81.04	12.7	2	A
56	09/04/2008	04:30:52	46.55	-80.98	18.9	2.9	A
57	10/04/2008	23:29:09	46.44	-81.10	8.7	2.4	A
58	12/04/2008	13:32:19	46.45	-81.07	10.4	2.2	A
59	19/04/2008	07:40:01	46.63	-81.39	22.5	2	B4
60	19/04/2008	11:30:17	46.63	-81.39	22.5	2.1	B4
61	24/04/2008	22:47:09	46.45	-81.08	9.7	2.4	A
62	30/04/2008	19:15:32	46.43	-81.29	8.5	2.3	A
63	08/05/2008	23:24:23	46.32	-80.80	35.3	2.1	B4
64	11/05/2008	16:28:00	46.66	-81.33	22.8	2.6	A
65	12/05/2008	07:28:35	46.53	-80.99	17.0	2	A
66	12/06/2008	23:26:34	46.43	-81.09	9.9	2.3	A
67	23/06/2008	00:49:12	46.57	-80.86	28.2	2.6	A
68	12/08/2008	06:36:12	46.53	-81.00	16.6	2.5	A
69	13/08/2008	17:37:31	46.54	-81.00	17.0	2.8	A
70	18/08/2008	14:54:12	46.50	-81.01	15.0	1.8	C45
71	04/09/2008	22:45:08	46.43	-81.09	9.9	2.3	A
72	09/09/2008	07:53:39	46.68	-81.38	26.6	1.7	C24
73	09/09/2008	07:53:41	46.68	-81.38	26.6	1.5	C24
74	09/09/2008	07:54:12	46.68	-81.38	26.6	1.6	C24
75	09/09/2008	13:35:21	46.54	-81.00	17.0	1.6	B4
76	09/09/2008	22:54:49	46.57	-80.86	28.2	2.9	A
77	11/09/2008	11:21:49	46.48	-81.04	12.4	3.8	A
78	16/09/2008	23:25:37	46.43	-81.31	9.7	2.4	A
79	17/09/2008	16:01:16	46.56	-80.99	18.8	1.4	C24
80	01/10/2008	07:44:01	46.52	-81.00	15.0	1.8	C45

N	Date dd/mm/yyyy	Time (UT)	Latitude	Longitude	Distance, km	Mag MN	Category
81	02/10/2008	20:30:07	46.42	-81.32	10.0	2.6	B5
82	06/10/2008	23:03:50	46.67	-81.37	26.0	3.4	B5
83	20/10/2008	20:14:12	46.54	-81.00	16.0	1.6	C45
84	19/11/2008	08:39:56	46.51	-80.99	17.9	2	A
85	05/12/2008	18:36:13	46.57	-80.85	30.1	3.1	B6
86	17/12/2008	02:55:37	46.46	-81.08	10.8	2.5	B6
87	21/12/2008	08:25:48	46.64	-81.35	20.9	2.7	B6
88	12/01/2009	11:28:38	46.67	-81.33	23.3	2.2	B6
89	22/01/2009	22:11:00	46.18	-80.78	46.1	2.2	B6
90	18/02/2009	20:48:45	46.48	-81.06	12.2	2.3	B4
91	23/02/2009	08:37:53	46.53	-81.00	17.8	2.1	B4
92	27/02/2009	09:02:56	46.51	-81.01	16.4	2	B4
93	03/03/2009	20:26:59	46.43	-80.88	26.5	2.5	B4
94	28/04/2009	22:43:51	46.55	-80.85	29.5	2.6	A
95	29/04/2009	19:15:47	46.22	-80.82	41.8	2.4	A
96	04/05/2009	20:58:16	46.59	-80.79	35.2	2.1	A
97	05/05/2009	15:55:06	46.44	-81.10	9.9	2.2	A
98	10/06/2009	23:35:43	46.21	-80.77	45.4	2	A
99	27/06/2009	03:11:09	46.62	-80.80	35.9	1.8	B2
100	22/07/2009	22:33:20	46.20	-80.79	45.0	2	B2
101	06/08/2009	17:03:14	46.49	-80.81	31.4	2.3	B2
102	17/08/2009	18:02:16	46.14	-80.39	73.0	2.2	C24
103	01/09/2009	23:11:46	46.20	-80.77	46.1	2	B2
104	22/09/2009	17:34:21	46.14	-80.43	71.0	2.3	C25
105	23/09/2009	18:11:30	46.62	-80.18	79.0	2	D245
106	23/09/2009	22:32:31	46.17	-80.76	48.0	2	C25

The category represented in the last column of Table 4 reflects the fullness of the database for the given event. Assigning to every station the sequence number: 1- SSNO, 2-11SNO, 3-46SNO, 4-LSNO/NSNO, 5- DSNO and 6-SUNO, the database categories are as follows:

- **A** - there are records at all 6 stations 1-6;
- **B1** - there are records at 5 stations; data of 1st station (SSNO) is missing; **B6** - there are records at 5 stations; data of 6th station (SUNO) is missing;
- **C12** - there are records at 4 stations; data of 1st and 2nd stations (SSNO and 11SNO) are missing;
- **D145** - there are records at 3 stations; data of 1st, 4th and 5th stations (SSNO, LSNO/NSNO and DSNO) are missing;
- **E3456** - there are only records at 2 stations; data of 3rd, 4th, 5th and 6th stations (46SNO, LSNO/NSNO, DSNO and SUNO) are missing.

The reason why records of any station are missing may be noise, incorrect transfer function or loss of data (see the previous chapter). Note that the distance given in Table 4 is the epicentral (horizontal) distance between DSNO station and the epicentre location estimated from regional data by the Geological Survey of Canada (GSC). For the weakest events, these distances may be in error by as much as 5 to 7 km.

Data from the POLARIS SUNO station were added to the database for use in evaluating ground-motion characteristics, such as attenuation and source parameters. Figure 12 shows the distribution of the data from the local events by magnitude and distance.

For local events, there are two available sources of information: the GSC's catalogue and database, and results of monitoring of the SNO Lab and Vale Creighton mine. The SNO Lab catalogue is accessible but it does not contain the event locations. Negotiations with the Vale Creighton mine authorities have provided additional information on mining events and blasts. One problem, however, is that the epicentre locations are given in Vale's own system of coordinates. Furthermore, their catalogue includes only events within or very close to this mine, so that they are mainly near-field and are not suitable for the site effect studies. The GSC catalogue provides a rough estimation of epicentres under the assumption that their depth is 1 km, for events strong enough to be well-recorded on the network. For smaller events, locations and magnitudes are not readily available. There are at least an additional 25 events (Table 5) for which the epicentres have not been determined. The epicentres for these events could potentially be determined by more detailed analysis involving application of the polarization analysis approach.

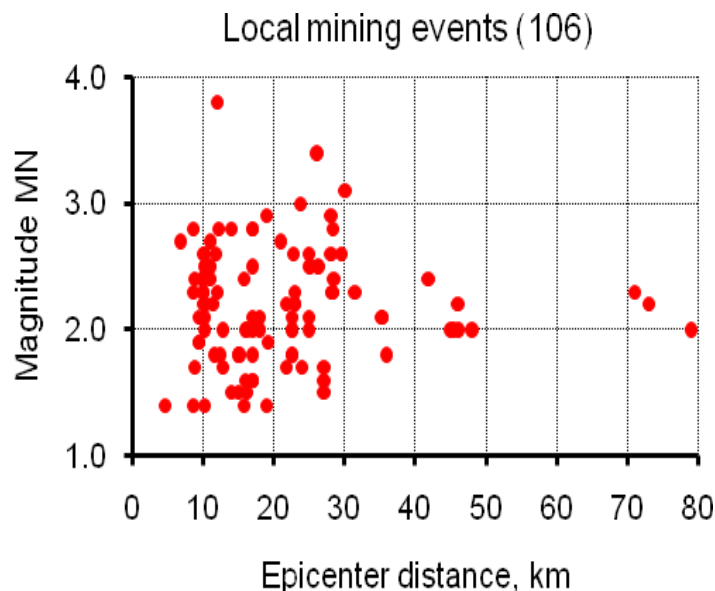


Figure 12: Distribution of local magnitudes MN in epicentre distance calculated for DSNO station for events listed in Table 4.

Additionally, there is a special group of very close events with significant near-field effects, due to the location of the seismic sensors within the coseismic slip area. The list of these events (Table 6) includes not only the Lively earthquake and its strongest aftershocks, but many other rock bursts located very near to at least one of the SNO stations. As in Table 4, the distance given in Table 6 is the epicentral distance between DSNO station and an event.

Figure 13 shows the broadband 3-component record of displacement, velocity and acceleration made by the 46SNO station from one such event, with magnitude MN3.1, which occurred on October 7, 2007. The processing of the input velocity record includes dividing by sensitivity, DC

(constant offset) correction by removing the mean determined from the pre-event segment of the record, and integration and differentiation to get displacement and acceleration, respectively.

Table 5: Events in the Vale Creighton Mine monitored by SNO Lab and recorded by SNO and SUNO stations in August 2006 - April 2008 but with unknown location

N	Date, dd/mm/yyyy	Time (UT)	Stations	Comments
1	26/10/2006	06:13:05	11,d,l	JSR, 2 blasts
2	20/11/2006	06:56:29	s,u,11,46,l	INCO blast
3	24/11/2006	07:01:39	s,u,11,46,l	INCO, 2 blasts
4	21/12/2006	06:55:12	s,11,46,l	JSR blast
5	10/02/2007	21:53:58	u,s,11,46,l	INCO blast
6	14/02/2007	09:21:42	u,s,11,46,l	INCO blast
7	24/02/2007	21:57:28	s,u,11,46,l	JSR blast
8	26/04/2007	06:17:32	s, u,11,46,l	INCO blast
9	01/05/2007	06:11:24	s, u,11,46,l	INCO blast
10	05/05/2007	04:25:39	s, u,11,46,l	INCO blast
11	05/05/2007	19:58:56	s, u,11,46,l	INCO blast
12	09/05/2007	06:12:37	s,u,11,46	INCO blast
13	11/05/2007	06:10:50	s,u,11,46	INCO blast
14	12/05/2007	19:51:03	s, u,11,46	INCO blast
15	14/06/2007	06:13:38	s,11,d,l	INCO blast
16	16/06/2016	02:46:30	s, u,11,d,l	Rock burst
17	28/08/2007	10:21:54	s,u,11,d,l	Mining event
18	22/09/2007	19:57:32	s, u,11,d,l	JSR blast
19	29/09/2007	04:53:16	s, u,11,d,l	INCO blast
20	26/10/2007	02:13:05	u,11,46,d,l	JSR blast
21	31/10/2007	06:16:42	u,11,46,d,l	JSR blast
22	24/11/2007	20:59:57	u,11,46,d,l	INCO blast
23	24/11/2007	20:59:57	u,11,46,d,l	INCO blast
24	29/12/2007	20:35:19	s,u,11,46,d,l	JSR blast
25	06/04/2008	16:26:35	s,u,11,46,d,l	Mining event

Table 6: Events within 7 km of DSNO station (46.47500, -81.20111), August 2006 – October 2009, with coseismic effects (unprocessed events with permanent offsets)

N	Date, dd/mm/yyyy	Time (UT)	Latitude degrees	Longitude degrees	Distance km	Magnitude MN	Stations
1	04/09/2006	20:28:20	46.46	-81.2	1.7	1.9	u,11,d,l
2	28/11/2006	21:02:55	46.48	-81.2	0.6	1.6	s,u,11,46,l
3	28/11/2006	22:26:42	46.47	-81.19	1	1.8	s,u,11,46,l
4	29/11/2006	07:22:55	46.48	-81.18	1.7	4.1	s,u,11,46,l
5	29/11/2006	07:36:17	46.47	-81.22	1.6	2	s,u,11,46,l
6	29/11/2006	07:38:17	46.48	-81.21	0.9	3.1	s,u,11,46,l
7	15/03/2007	08:46:08	46.45	-81.25	4.7	2	s, u,11,46,l
8	19/08/2007	07:30:40	46.46	-81.17	2.9	1.3	s, u,11,d,l
9	07/10/2007	22:15:51	46.46	-81.17	2.9	3.1	u,11,46,d,l
10	08/10/2007	00:56:26	46.46	-81.17	2.9	1.5	u,11,46,d,l

N	Date, dd/mm/yyyy	Time (UT)	Latitude degrees	Longitude degrees	Distance km	Magnitude MN	Stations
11	09/10/2007	22:20:27	46.46	-81.17	2.9	0.9	u,11,46,d,l
12	10/10/2007	00:44:22	46.46	-81.17	2.9	1.1	u,11,46,d,l
13	11/10/2007	23:14:33	46.48	-81.12	2.5	2.4	u,11,46,d,l
14	16/10/2007	06:00:14	46.46	-81.17	2.9	1.1	11,46,d,l
15	16/10/2007	11:43:20	46.48	-81.17	2.5	2	11,46,d,l
16	16/10/2007	12:26:18	46.46	-81.17	2.9	0.9	11,46,d,l
17	16/10/2007	06:21:38	?	?	?	?	u,11,46,d,l
18	18/10/2007	00:33:34	46.46	-81.17	2.9	1	u,11,46,d,l
19	20/11/2007	14:34:59	46.46	-81.17	2.9	0.6	11,46,d,l
20	05/12/2007	14:21:09	46.46	-81.17	2.9	2.7	u,11,46,d,l
21	19/12/2007	07:45:01	?	?	?	?	s,11,46,d,l
22	19/12/2007	07:35:34	46.49	-81.19	1.9	2.8	s,11,46,d,l
23	22/02/2008	00:17:26	?	?	?	?	s,u,11,46,d,l
24	19/03/2008	08:06:36	46.47	-81.2	0.6	2.9	s,u,11,46,d,l
25	04/04/2008	04:31:24	46.47	-81.19	1	2.4	s,u,11,46,d,l
26	24/04/2008	21:51:50	46.45	-81.21	2.9	2.1	s,u,11,46,d,l
27	10/05/2008	04:04:38	46.46	-81.17	4	1.8	U
28	11/05/2008	05:56:17	46.46	-81.17	3	1.7	s,u,11,46,d,l
29	17/05/2008	05:27:35	46.46	-81.17	3	1.4	s,u,11,46,d,l
30	29/05/2008	00:23:22	46.45	-81.19	3	2.3	s,u,11,46,d,l
31	19/06/2008	08:08:51	46.46	-81.17	3	2.4	s,u,11,46,d,l
32	24/06/2008	16:17:58	46.46	-81.22	2	2.2	s,u,11,46,d,l
33	11/09/2008	15:49:36	46.45	-81.21	<5	2	s,u,11,46,d,l
34	11/09/2008	18:55:20	46.46	-81.22	<5	2	s,u,11,46,d,l
35	06/12/2008	22:46:04	46.51	-81.16	5	2.7	s,11,46,d,n
36	17/01/2009	22:09:18	46.5	-81.3	7	2.1	s,11,46,d,n
37	27/01/2009	09:24:02	46.51	-81.18	<5	1.6	s,11,46,d,n
38	10/02/2009	09:53:47	46.5	-81.19	<5	2	s,u,11,46,d,n
39	14/02/2009	19:10:53	46.46	-81.17	4	1.6	s,u,11,46,d,n
40	14/02/2009	20:19:24	46.46	-81.17	4	3.2	s,u,11,46,d,n
41	15/02/2009	00:54:40	46.46	-81.17	4	2.2	s,u,11,46,d,n
42	15/02/2009	01:17:42	46.46	-81.17	4	2.9	s,u,11,46,d,n
43	15/02/2009	01:23:11	46.46	-81.17	4	2.7	s,u,11,46,d,n
44	15/02/2009	03:01:51	46.46	-81.17	4	1.9	s,u,11,46,d,n
45	15/02/2009	04:27:12	46.46	-81.17	4	1.4	s,u,11,46,d,n
46	18/02/2009	13:53:59	46.46	-81.17	4	2	s,u,11,46,d,n
47	14/03/2009	19:45:58	46.48	-81.16	4	2.6	s,u,11,46,d,n
48	14/03/2009	22:17:12	46.48	-81.17	<5	2.9	s,u,11,46,d,n
49	17/03/2009	08:37:27	46.49	-81.16	<5	1.9	s,u,11,46,d,n
50	06/04/2009	08:23:10	46.5	-81.14	1	2	s,u,11,46,d,n
51	20/04/2009	20:40:36	46.48	-81.2	<5	2.9	s,u,11,46,d,n
52	10/05/2009	01:05:36	46.48	-81.15	<5	2.8	s,u,11,46,d,n
53	11/05/2009	02:50:59	46.48	-81.17	<5	2.4	s,u,11,46,d,n

071007a dist=3.9km baz=1.9 MN=3.1

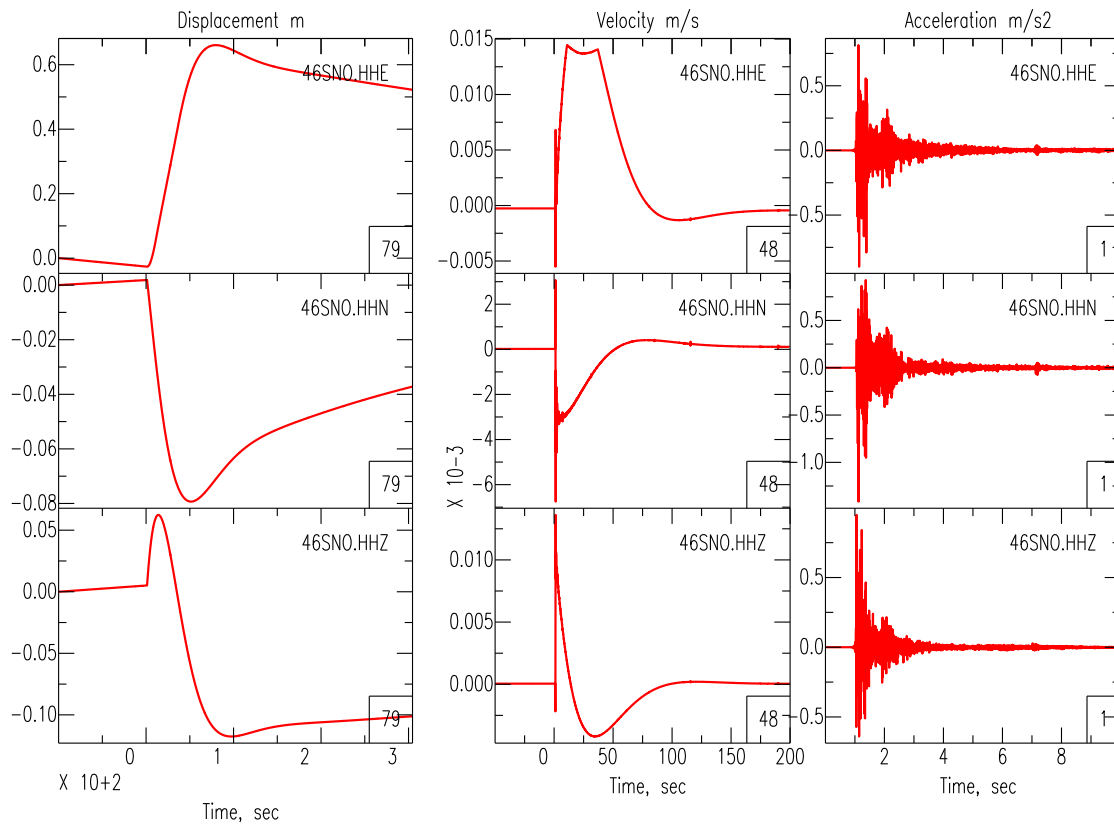


Figure 13: 3-component displacement, velocity and acceleration recorded by the 46SNO station 7 October 2007 in the coseismic slip area of the event MN3.1.

Non-linear effects are clearly seen in this typical near-field record. The input signal is discontinuous, in the form of a generalized Heaviside step function in displacement, delta function in velocity, and derivative of delta function in acceleration. This results in a seismometer response in the form of derivatives of its transfer function, depending on the order of the discontinuity (turn-on transient process). This kind of data demands additional studies for processing, and are therefore not used in this study for spectral estimations – which are made under the assumption of far-field observations and a linear record of continuous ground motions.

To evaluate long-period behaviour at underground stations, teleseismic records from large distant earthquakes are most useful. 73 regional and teleseismic events (Table 7, Figure 14) located by GSC and the U.S. Geological Survey (USGS) have been processed. For these events, there are two or more records on the SNO network with sufficiently high signal-to-noise ratios in the frequency band of interest (0.05-1 Hz for teleseismic and 0.3-1 Hz for regional events).

Table 7: Teleseismic events, August 2006-April 2009

N	Date dd/mm/yyyy	Time (UT)	Latitude degrees	Longitude degrees	Distance km	Magnitude Mw	Depth km	Category
1	24/08/2006	21:50:37	51.148	157.522	7818	6.5	43	C13
2	25/08/2006	00:44:46	-24.403	-67.028	7978	6.6	184	C13
3	01/09/2006	10:18:52	-6.759	155.512	13062	6.8	38	C13
4	13/11/2006	01:26:36	-26.052	-63.283	8232	6.8	572	B5
5	15/11/2006	11:14:14	46.592	153.266	8410	8.3	10	B5
6	09/01/2007	15:49:35	59.370	-136.870	3874	6	20	C56
7	13/01/2007	04:23:21	46.243	154.524	8385	8.1	10	B5
8	01/04/2007	20:39:59	-8.466	157.043	13094	8.1	24	A
9	13/06/2007	19:29:40	13.554	-90.618	3755	6.7	23	B3
10	16/07/2007	14:17:37	36.808	134.850	10104	6.8	350	B3
11	02/08/2007	03:21:43	51.307	-179.971	6690	6.7	21	B3
12	08/08/2007	17:05:05	-5.859	107.419	15428	7.4	280	B3
13	15/08/2007	23:40:58	-13.386	-76.603	6645	7.7	39	B3
14	20/08/2007	22:42:28	8.036	-39.251	5835	7	6	B3
15	10/09/2007	01:49:12	2.966	-77.963	4831	6.5	15	B3
16	12/09/2007	11:10:27	-4.438	101.367	15339	8.2	34	B3
17	12/09/2007	23:49:04	-2.625	100.841	15141	7.8	35	B3
18	13/09/2007	03:35:29	-2.130	99.627	15090	7	22	B3
19	28/09/2007	13:38:58	22.013	142.668	11235	7.4	260	B3
20	30/09/2007	05:23:34	-49.271	164.115	15275	6.9	10	B3
21	02/10/2007	18:00:07	54.640	-161.800	5462	6.2	48	B1
22	24/10/2007	21:02:51	-3.899	101.020	15281	6.8	21	B1
23	31/10/2007	03:30:16	18.900	145.388	11392	7.2	207	B1
24	14/11/2007	15:40:50	-22.247	-69.890	7695	7.7	40	B1
25	16/11/2007	03:13:00	-2.312	-77.838	5415	6.7	122	B1
26	29/11/2007	19:00:20	14.944	-61.274	3958	7.4	156	B1
27	09/12/2007	07:28:21	-25.996	-177.514	12521	7.7	152	C14
28	12/12/2007	23:39:58	52.050	-131.990	3671	5.6	20	B4
29	19/12/2007	09:30:28	51.360	-179.509	6661	7	34	B6
30	05/01/2008	10:39:09	50.980	-130.930	3622	5.7	10	B6
31	05/01/2008	11:01:01	51.070	-131.060	3629	6.5	10	B6
32	05/01/2008	11:44:44	50.830	-130.980	3629	6.4	10	B6
33	06/01/2008	00:20:29	51.330	-131.300	3640	5.3	10	B6
34	09/01/2008	14:39:57	51.500	-131.320	3637	5.9	10	B6
35	08/02/2008	09:38:14	10.671	-41.899	5428	6.9	9	A
36	20/02/2008	08:08:30	2.768	95.964	14542	7.4	26	A
37	25/02/2008	08:36:33	-2.486	99.972	15129	6.9	25	A
38	20/03/2008	22:32:58	35.490	81.467	10762	7.2	10	A
39	09/04/2008	12:46:13	-20.071	168.892	13114	7.3	33	A
40	16/04/2008	05:54:20	51.878	-179.165	6606	6.6	13	A
41	12/05/2008	06:28:02	31.002	103.322	11412	7.9	19	A
42	23/05/2008	19:35:35	7.310	-34.900	6177	6.5	8	A
43	17/06/2008	17:42:10	5.010	-82.650	4591	5.9	10	C34
44	22/06/2008	23:56:30	67.700	141.280	6861	6.1	18	A
45	03/07/2008	06:34:54	10.280	-60.440	4463	5.8	33	B4
46	05/07/2008	02:12:04	53.880	152.890	7776	7.7	632	B5
47	08/07/2008	09:13:07	-15.990	-71.750	6971	6.2	123	C45
48	17/07/2008	22:51:55	44.370	-129.420	3722	5.7	10	B4

N	Date dd/mm/yyyy	Time (UT)	Latitude degrees	Longitude degrees	Distance km	Magnitude Mw	Depth km	Category
49	26/08/2008	21:00:37	-7.640	-74.380	6023	6.4	154	A
50	28/08/2008	12:37:35	50.170	-129.630	3552	5.9	10	A
51	10/09/2008	13:08:15	8.090	-38.720	5857	6.6	10	A
52	13/09/2008	09:32:01	4.790	-75.520	4646	5.7	132	A
53	18/09/2008	01:41:03	-4.550	-106.000	6151	6	10	B4
54	24/09/2008	02:33:05	17.610	-105.500	3901	6.4	10	B5
55	07/10/2008	10:00:48	79.820	-115.450	3958	5.7	10	B5
56	11/10/2008	10:40:14	19.160	-64.830	3376	6.1	23	B5
57	16/10/2008	19:41:26	14.420	-92.360	3699	6.7	24	B5
58	02/11/2008	13:48:43	51.550	-174.370	6364	6.1	36	B5
59	15/11/2008	23:03:17	13.050	-88.750	3768	5.8	49	A
60	17/11/2008	12:55:23	79.650	-116.060	3952	5.7	7	A
61	19/11/2008	06:11:21	8.270	-82.970	4233	6.2	32	A
62	24/11/2008	09:02:59	54.200	154.320	7690	7.3	492	A
63	28/11/2008	13:42:19	40.350	-126.980	3715	5.9	10	C36
64	07/12/2008	06:23:10	13.350	-44.830	4997	5.7	10	B6
65	19/12/2008	08:31:51	47.000	-27.290	4037	5.9	2	B6
66	25/12/2008	08:11:59	49.120	-128.630	3507	5.8	10	B6
67	03/01/2009	19:43:51	-0.410	132.880	13921	7.6	17	C36
68	08/01/2009	19:21:34	10.200	-84.160	4026	6.1	4	C56
69	15/01/2009	17:49:39	46.860	155.150	8307	7.4	36	B6
70	24/01/2009	18:09:50	59.600	-153.190	4782	5.8	98	B6
71	06/03/2009	10:50:29	80.260	-1.800	4755	6.5	9	B4
72	19/03/2009	18:17:41	-23.050	-174.670	12073	7.6	34	B4
73	07/04/2009	04:23:34	46.140	151.420	8532	7	39	B4

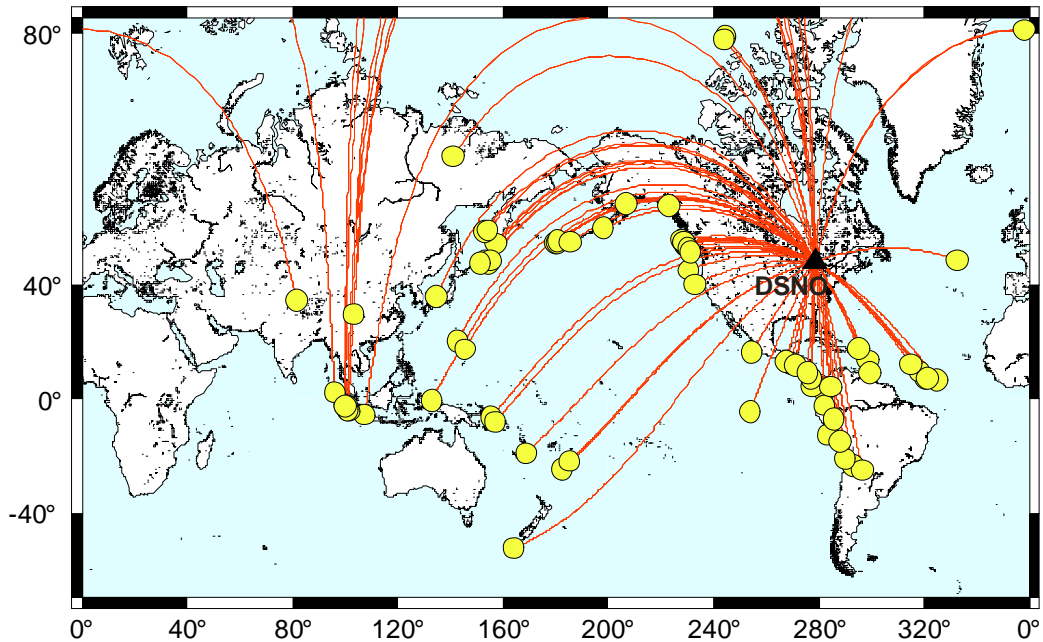


Figure 14: Map showing teleseismic events epicentres and DSNO station location.

Figure 15 shows the distribution of the data from the teleseismic events by magnitude and distance.

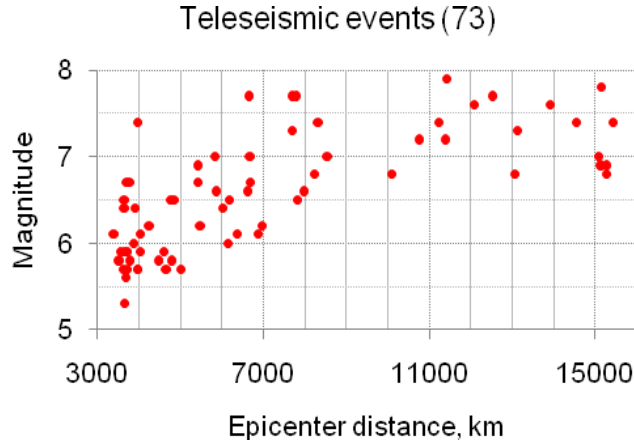


Figure 15: Distribution of moment magnitudes M_w in epicentre distance calculated for DSNO station for teleseismic events listed in Table 7.

72 other teleseismic events recorded by SNO stations during April–September, 2009 were extracted as well. These events were not processed, but were included in the database and are obtainable from the University of Western Ontario’s POLARIS ftp server, located at: <ftp://polaris.es.uwo.ca/pub/seismotoolbox/pupsdatabase>.

Finally, the regional event catalogue, showing events recorded during the PUPS experiment with good signal-to-noise ratio (SNR), for frequencies 0.5-10 Hz, is listed in Table 8, and its distribution by magnitude and distance is shown in Figure 16.

Table 8: Regional events within 1050 km of DSNO station (46.47500, -81.20111), August 2006-October 2009

N	Date dd/mm/yyyy	Time (UT)	Latitude Degrees	Longitude degrees	Distance Km	Magnitude M_w	Depth km	Category
1	23/11/2006	10:42:57	37.16	-81.97	1036	4.3	0	D145
2	07/12/2006	04:44:59	49.51	-81.53	339	4.2	16	C45
3	06/01/2007	04:08:45	47.03	-76.23	384	3.3	18	E1456
4	02/10/2007	07:26:20	48.28	-78.57	282	3	1g	D145
5	12/02/2007	23:11:41	45.29	-83.47	220	2.7	0g	B4
6	12/03/2007	23:18:17	41.33	-81.39	572	3.7	5	B4
7	11/05/2007	05:55:23	46.71	-76.09	392	3.2	18	B4
8	19/07/2007	17:07:58	43.71	-78.17	389	3.1	5	C34
9	06/08/2007	14:50:16	45.07	-83.49	237	2.8	0g	C34
10	30/09/2007	17:35:35	46.88	-76.52	361	3.9	13	C34
11	01/10/2007	16:42:08	47.08	-76.88	337	4.1	18	B3
12	13/10/2007	05:53:32	46.53	-75.13	466	3.5	11	C14
13	28/10/2007	09:47:18	46.55	-77.17	309	3.4	18g	C14
14	20/12/2007	12:16:41	45.79	-76.96	336	3	18	C46
15	23/12/2007	23:48:35	46.26	-77.32	299	3.6	18	C46

N	Date dd/mm/yyyy	Time (UT)	Latitude Degrees	Longitude degrees	Distance Km	Magnitude Mw	Depth km	Category
16	05/02/2008	19:33:52	45.86	-79.38	156	2.5	0g	B4
17	21/03/2008	18:08:53	49.74	-81.48	357	3	16g	B4
18	18/04/2008	09:36:57	38.45	-87.89	1047	5.2	12	B4
19	18/04/2008	15:14:16	38.48	-87.85	1042	4.8	10	B4
20	21/04/2008	05:38:29	38.5	-87.85	1039	4	10	B4
21	11/06/2008	04:36:34	45.63	-75.38	460	3.2	18	B4
22	12/07/2008	07:17:10	48.14	-80.09	203	3.1	1g	B4
23	20/07/2008	08:14:51	48.25	-78.44	287	3.3	1g	B4
24	22/08/2008	19:31:49	49.26	-82.84	235	3	0g	B4
25	15/11/2008	10:52:53	47.74	-69.71	883	4.2	20	A
26	26/11/2008	20:35:54	45.06	-83.45	235	2.7	0g	B6
27	29/12/2008	17:57:12	45.14	-83.33	222	2.6	0g	B6
28	31/12/2008	06:54:49	46.15	-75.45	444	3.2	7	B6
29	04/01/2009	04:36:48	46.31	-79.65	121	2.1	5g	B6
30	06/01/2009	09:40:13	48.73	-81.32	251	3.8	1g	B6
31	06/01/2009	21:20:02	45.08	-83.4	231	2.7	0g	B6
32	15/01/2009	10:32:49	48.68	-85.88	429	3	1g	B6
33	26/01/2009	08:30:03	46	-78.98	179	2.4	5g	B6
34	26/01/2009	20:36:52	45.08	-83.42	235	2.6	0g	C36
35	12/02/2009	19:34:37	45.07	-83.5	237	2.6	0g	A
36	24/02/2009	00:58:36	48.13	-80.05	204	3.4	5g	B4
37	09/03/2009	23:47:18	45.96	-79.64	133	2	0g	B4
38	18/03/2009	18:19:08	48.28	-78.6	282	2.6	1g	B4
39	26/03/2009	15:07:07	45.36	-79.97	157	2.2	0g	B4
40	23/04/2009	18:02:46	46.33	-79.49	134	2.4	0g	A
41	24/04/2009	13:42:46	38.81	-82.27	856	3.3	5	A
42	25/04/2009	13:00:02	46.15	-79.28	154	2.7	5g	A
43	27/04/2009	21:35:12	46.38	-79.42	139	2	0g	A
44	26/05/2009	21:48:04	48.29	-78.5	288	2.6	1g	A
45	28/05/2009	09:19:24	45.83	-75.85	421	3.0	18	B2
46	29/05/2009	17:15:03	46.35	-79.55	129	2.5	0g	A
47	03/06/2009	22:30:18	46.40	-79.46	135	2.2	0g	A
48	05/06/2009	15:07:52	42.86	-78.25	466	3.4	18g	A
49	10/06/2009	17:45:21	45.13	-83.44	228	2.5	0g	B2
50	10/06/2009	20:21:35	45.28	-79.64	181	2.5	0g	A
51	16/06/2009	00:01:04	48.72	-81.34	250	3.1	1g	A
52	17/06/2009	08:20:22	47.26	-77.14	323	3.1	18g	A
53	24/06/2009	16:29:55	45.95	-83.72	202	2.3	0g	A
54	03/07/2009	07:12:30	48.27	-78.45	288	2.2	1g	C23
55	08/07/2009	14:02:07	45.89	-83.2	166	2.5	0g	A
56	21/07/2009	14:20:56	49.73	-65.68	1210	4.2	13.8	A
57	06/08/2009	02:39:24	48.25	-78.44	288	2.2	1g	B2
58	11/08/2009	05:28:35	48.71	-81.37	249	2.6	1g	A
59	12/08/2009	22:37:03	45.67	-79.43	165	2.0	0g	A
60	24/08/2009	14:18:49	45.86	-83.29	174	2.4	0g	A
61	02/09/2009	19:11:22	45.67	-79.72	147	2.1	0g	A
62	03/09/2009	13:53:46	45.90	-83.24	169	2.4	0g	A
63	03/09/2009	22:01:43	45.45	-80.13	142	2.0	0g	B2
64	11/09/2009	02:14:16	48.25	-78.43	288	2.1	1g	C25
65	30/09/2009	15:32:42	45.69	-79.39	166	2.3	0g	C25
66	03/10/2009	06:04:32	45.97	-77.02	328	3.1	18g	B5

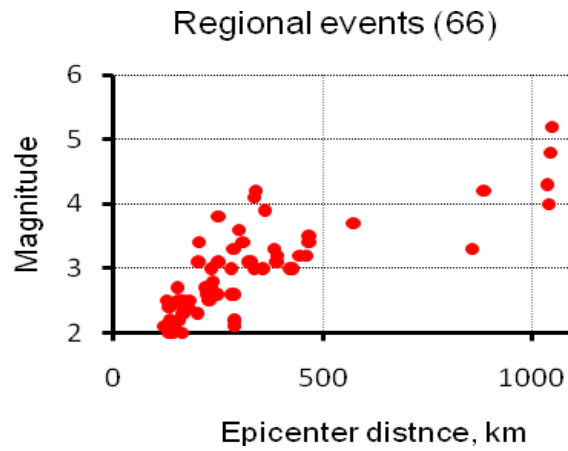


Figure 16: Distribution of moment magnitudes M_w in epicentre distance calculated for DSNO station for regional events listed in Table 8.

The regional event database includes records of 66 regional events, with magnitude 2-5.2, at distances 121 km–1210 km. This database is not uniform with respect to source depth. There were 40 events within 300 km, of which only 4 had depths of 5 km or greater; the other 36 nearby regional events were mining-related or blasts, typically at 0-1 km depth. By contrast, the more distant 26 events are not mining-related (except one or two), and originated at 5-20 km depth (Figure 17).

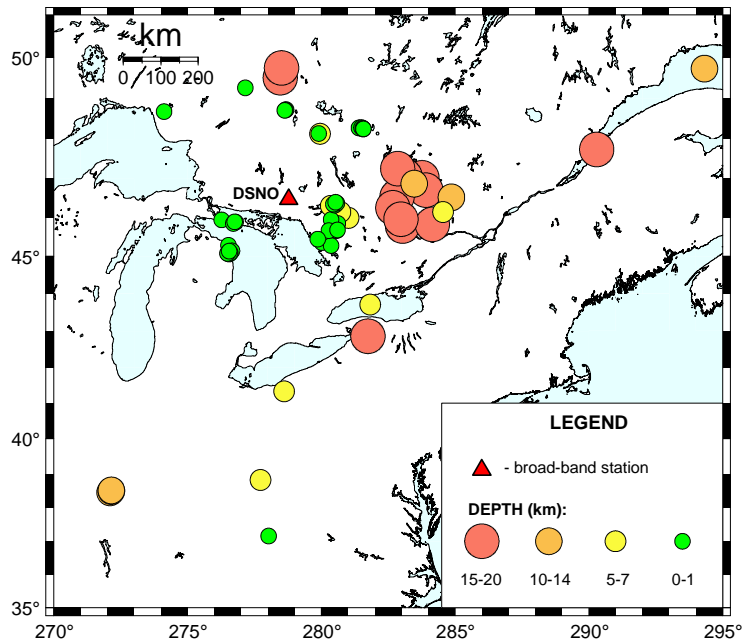


Figure 17: Map showing regional events epicentres and DSNO station location.

2.3 NOISE-REMOVING FILTER ALGORITHM

Mining activity noise is the main challenge and problem in the SNO station data processing. To exclude noise from digital data, it is necessary to apply some kind of filtering. In the first year of the PUPS project, the usual bandpass Butterworth filter was used, with high and low corner frequencies estimated from the signal-to-noise ratio (SNR) depending on frequency. It is reasonable to take into consideration, for further spectral analysis, only frequencies where the SNR exceeds a factor of two. However, the signal inside this band can be refined, and the band can be broadened, if a noise-suppression technique is employed to improve the SNR in the speech signal. – The approach is based on the combination of spectral subtraction with iterative Wiener filtering (Boll, 1979; Davidek et al., 1995; Sovka et al., 1996). The key idea of spectral subtraction is to estimate background noise and then to subtract this estimation from the noisy signal. The noise characteristics are calculated during speech pauses. In this case, the pre-event noise is used to represent the background noise estimation.

Let $s[n]$, $v[n]$, and $u[n]$ represent a signal from seismic event, noise and noisy signal, respectively. Suppose that a signal is stochastic, while noise is additive and uncorrelated with it:

$$u[n] = s[n] + v[n] \quad (1)$$

It is assumed further that the noise is short-term stationary and its rate changes relatively slowly compared to that of the signal. In this case it is possible to apply concepts such as correlation and autocorrelation (Jenkins and Watts, 1969), which in the frequency domain allows for the conclusion that the power spectra of the signal and noise are also additive:

$$\mathcal{U}(e^{j\omega T}) = S(e^{j\omega T}) + V(e^{j\omega T}), \quad (2)$$

where $\mathcal{U}(e^{j\omega T})$ is the short-time power spectral density (PSD) of a noisy signal, $S(e^{j\omega T})$ and $V(e^{j\omega T})$ are the PSDs of the signal and noise, respectively. Then the simplest approximation of the adaptive noncausal Wiener filter transfer function is then:

$$\mathcal{H}^2(e^{j\omega T}) = [|\mathcal{U}(e^{j\omega T})|^2 - |\bar{U}(e^{j\omega T})|^2] * [|\mathcal{U}(e^{j\omega T})|^{-2}] = 1 - Y^2(e^{j\omega T}) \quad (3)$$

where $Y(e^{j\omega T})$ is the signal-to noise spectral ratio, and $|\bar{U}(e^{j\omega T})|^2$ is the smoothed estimation of the noise PSD, performed by averaging of PSDs of the pre-event noise calculated in sliding windows. For 10 s S-wave signals from local mining events, a 30s duration of this pre-event noise, using a 10 s sliding window with a shift of 5 s, seems to be a reasonable compromise. The noise suppressing filter will be individual for every event and every station channel; for example, the green curve in Figure 18 on the left shows the spectral amplitude of the filter calculated for the event of Nov 28, 2007 (MN3.0), as recorded by the vertical sensor at the 11SNO station.

The effectiveness of this filter depends on how stationary the noise is, and is affected by distortions introduced by descriptions of a mostly deterministic signal by random process operations, such as correlation and PSD. Comparison of the original and filtered signals on Figure 18b, or spectra of the input noisy signal (red curve) and refined one after filtration (green curve), as shown in Figure 19 on the right, demonstrates that microseisms and microtremors in the signal have been reduced; this supports applicability of the method described above to our seismic signals. Because the filter does not fully remove the noise at frequencies where the

SNR is low ($f < 0.5\text{ Hz}$ and $f > 30\text{ Hz}$), additional Butterworth band-pass filtering is applied to improve the results. This is shown on Figure 20. Note that noise issues place limitations on the frequency range over which conclusions can be drawn.

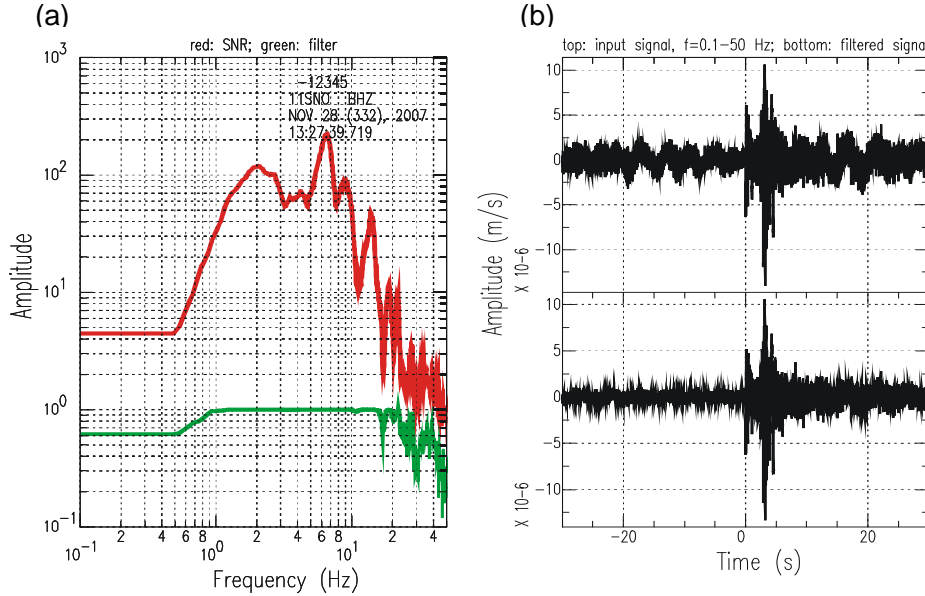


Figure 18: (a) Signal-to-noise ratio (red line) and noise suppressing filter (green line) amplitude spectra estimated for the 28 November 2007 M3.0 local mining related event recorded by the vertical channel of 11SNO station. (b) Top - noisy signal; bottom – enhanced signal, both in the frequency band 0.1-50 Hz

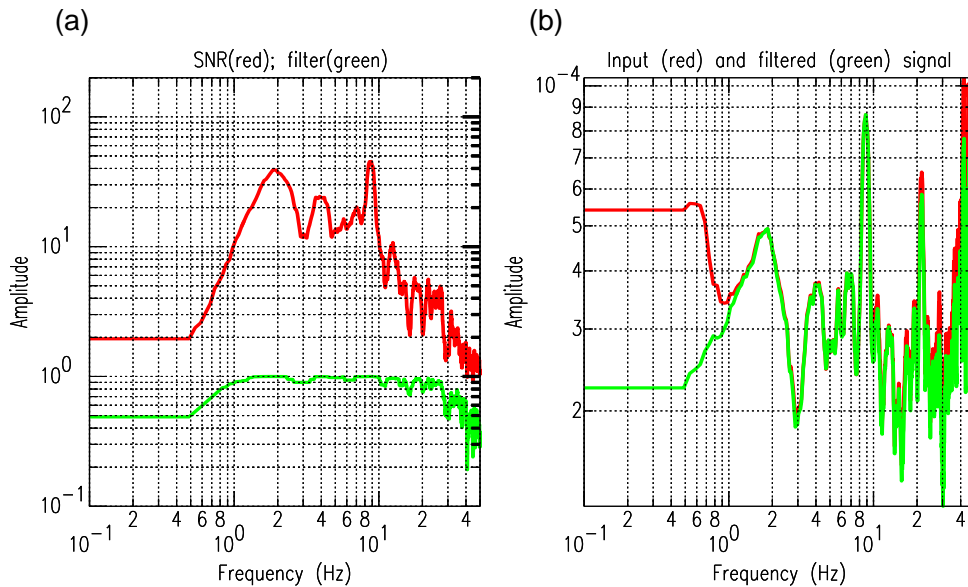


Figure 19: (a) Signal-to-noise ratio (red line) and noise suppressing filter (green line) amplitude spectra estimated for the 11 May 2008 MN2.6 (Table 3) local mining event recorded by the vertical channel of 11SNO station. (b) S-wave velocity spectra before (red line) and after (green line) filtration by the noise removing filter shown on the left.

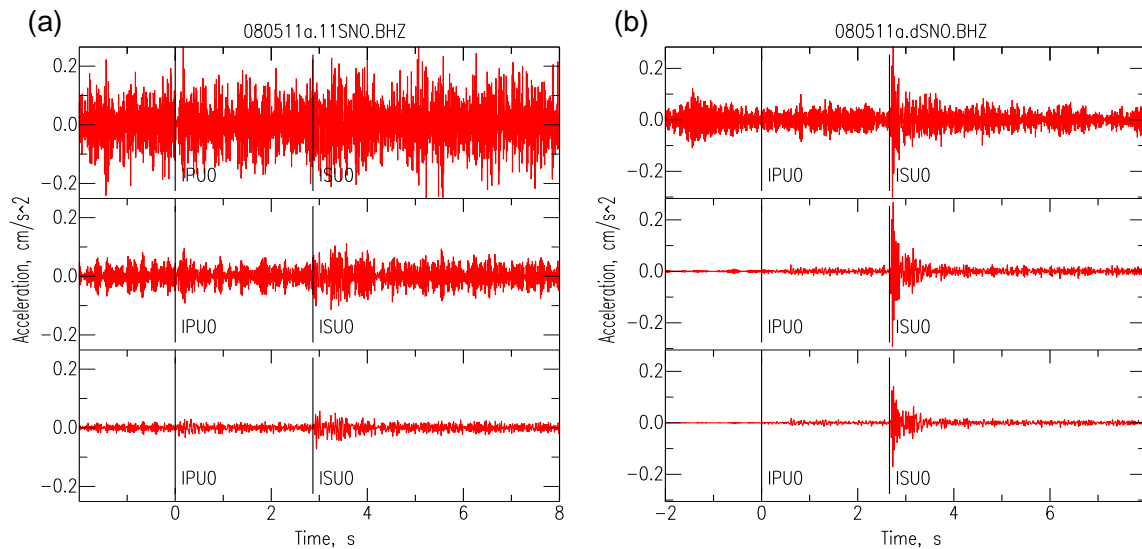


Figure 20: Accelerograms of the same event as in Figure 19 recorded by vertical channels of stations (a) 11SNO and (b) DSNO. Upper lines correspond to instrument-corrected signals before filtering. Middle lines show Butterworth-filtered data in the frequency band 0.1-50 Hz; bottom lines are data after applying both noise-subtraction and additional Butterworth filtering in the frequency band 0.5-30 Hz.

2.4 DATA PROCESSING

When dealing with a large amount of digital data, it is important to systematize the process of their preparation to minimize manual manipulations and associated potential errors. UNIX and LINUX systems are the most suitable environments for such work, allowing operations with lists of records, commands and routines, compiling of C and Fortran codes in the command line, and the advantages of shell programming. In addition, this method can take advantage of the capabilities of the Lawrence Livermore National Laboratory Seismic Analysis Code (SAC) package (<http://www.iris.edu/manuals/sac/manual.html>), with which many manipulations can be performed using data processing scripts.

The process of data preparation for events with known epicentres starts with extracting of digital 3-component seismograms from the continuous individual SNO stations' records, windowed in accordance with the origin time in the catalogue. Due to large time shifts at underground stations without GPS timing, the time window must be sufficiently wide to ensure the presence of the seismogram of the particular event in this piece of record. Extraction of data is realized using the special Nanometrics program "APOLLO". The data extracted are in the miniSEED (Standard for Exchange of Earthquake Data) format, which is first converted to sac-binary format. Conversion is done by a publicly available utility HAM of Ernesto Del Prete presented in the seismological software library at the Observatories and Research Facilities for European Seismology (ORFEUS) at <http://www.orfeus-eu.org/Software/conversion.html>, last accessed in 2006. The conversion yields a set of input raw data files in SAC format consisting of the 30-line header (but including very limited information on details of the data parameters), and the digital seismogram measured in velocity counts.

In the case of local mining events (Table 4), the main goal in the first stage of preparing data for further spectral analysis is to import a 10s sample that includes the S-wave signals into SAC text format, corrected for the instrument and pre-event noise, filtered in the frequency band 0.1-50 Hz, with the header including all information about the event and seismometer. Header information includes: absolute GMT times of P and S arrival and zero time, event and station coordinates, azimuth and distance to the event, event magnitude, corner frequencies of the band-pass filter, the frequency region where SNR>2, units (e.g., cm/s), time increment, number of points, name of the station and component, maximum and minimum values of dependent variable, and component azimuth and incident angles. If necessary, additional user determined information can be added to the header.

Figure 21 presents a diagram showing two steps of data preparation to reach this goal. The two steps are realised as two c-shell scripts using LINUX and SAC utilities (Note: except for the additional noise correction routine, and functions that pick body waves and do automatic signal cutting, etc., these scripts are similar in their output to the FORTRAN program “sacprocessT” written by Gail Atkinson in the project’s first year study for data processing in the Windows environment).

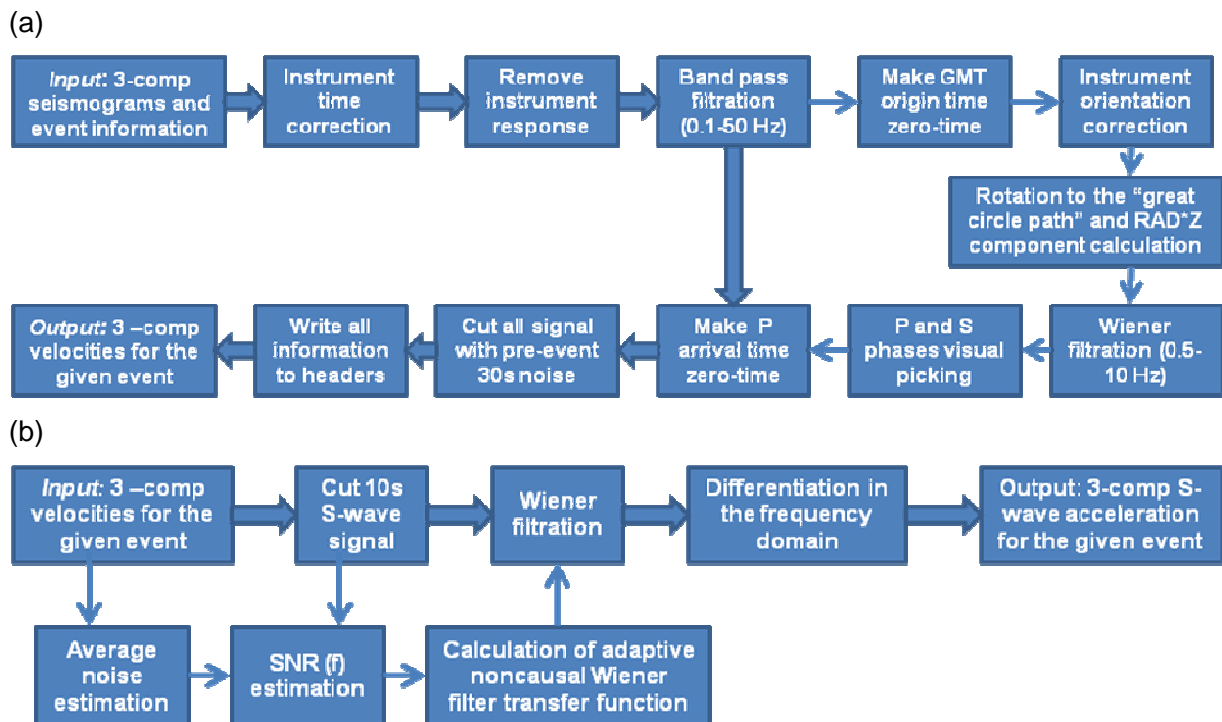


Figure 21: Data preparation steps. (a) step1: prepare velocity records for the given event (30 s before and 60 s after the P-arrival), corrected for instrument and filtered, with all information about the event and station in headers of files in the SAC-format. (b) step2: prepare acceleration S-wave 10 s records for the given event with noise removed by spectral subtraction.

The script corresponding to *step 1* (Figure 21a) prepares velocity records for the given event, corrected for instrument and filtered, and writes all information about the event and station in headers of files in SAC-format. First, it applies the rough time corrections based on the preliminary teleseismic event observations. The instrument response is then removed by the spectral division method realised in the SAC routine: this uses the poles, zeros, normalization factor and channel sensitivity of the Trillium seismometer transfer function as combined with the Nanometrics data acquisition system. The values of these parameters are located on the University of Western Ontario's POLARIS ftp server at the following address: <ftp://polaris.es.uwo.ca/pub/seismotoolbox/pupsdatabase>. Finally, band-pass filtering (0.1-50 Hz) is applied.

Based on the specified GMT zero time, the script automatically finds the time window that contains the signal, and displays it on the screen in the system coordinates of the source (R - radial, T - transverse, Z - vertical components and the R*Z product), as shown in Figure 22. The plotted traces are used for visual picking of P- and S-phase onsets, using polarisation properties of arriving waves (Plesinger et al., 1986), as shown in Figure 22. Specifically, for surface observations, the transverse components show very clearly the time of the SH-phase onset, while the product of vertical and radial components R*Z must be positive for P-waves, negative for SV-waves and oscillating for Rayleigh waves. This holds in the ideal case of a horizontally-homogeneous Earth and a correct epicentre location; the plotting of the R*Z product helps to read a seismogram and determine the type of waves arriving more reliably. For underground observations, the R*Z product is zero if the depth of the event and seismometer are equal, or negative, if the seismometer is deeper than the hypocenter (Figure 22b). To make picking easier, the noise-suppressing adaptive Wiener SAC filter is applied to the signal. This is a prediction error filter designed using the Yule-Walker Method from an autocorrelation function estimated from the designated partial data window (<http://www.iris.edu/manuals/sac/manual.html>). Note, however, that this version of the Wiener filter distorts the amplitude spectra of a signal, and thus is used only as a picking aid.

The onset time of the P-wave is used for cutting of the 3-component whole-signal from the given event, along with the pre-event noise (30 s before and 60 s after the P-phase onset). These files are saved in the digital database and can be used later for different purposes.

The script corresponding to *step 2* of processing (Figure 21b) extracts just the 10 s portion containing the S-wave from the whole-signal velocity files (from step 1); it converts the signal to acceleration by differentiation in the frequency domain, with noise removed by spectral subtraction. The average pre-event noise and noise suppressing filter are calculated using the techniques described above. For every event and every station's channel, the script outputs postscript files with figures showing the distribution of signal to noise ratio over all frequencies; from this information, the appropriate frequency range for analysis, and the S-wave velocity spectra before and after noise correction are determined (see the example on Figure 19).

Finally, for every event and every station, the Fourier amplitude spectrum of acceleration is calculated (Figure 23) and the response spectrum of acceleration (Figure 24) of a signal extracted in *step 2*. Log-based smoothing, in increments of 0.1 log units of frequency, is applied to the Fourier amplitude spectrum. These procedures are realised through the FORTRAN code `spectra.f`, which is taken from the program `sacprocess.f` used for response spectra calculations in the first year of the project; this spectrum calculation is based on the Nigam-Jennings approach as implemented by Boore (1996). The program outputs two summary files with all amplitude and response spectra for the given event, accompanied by the

information about this event taken from the headers of individual SAC data files. Special c-shell scripts then take these files as input to prepare postscript figure files with summary spectral graphics for every event.

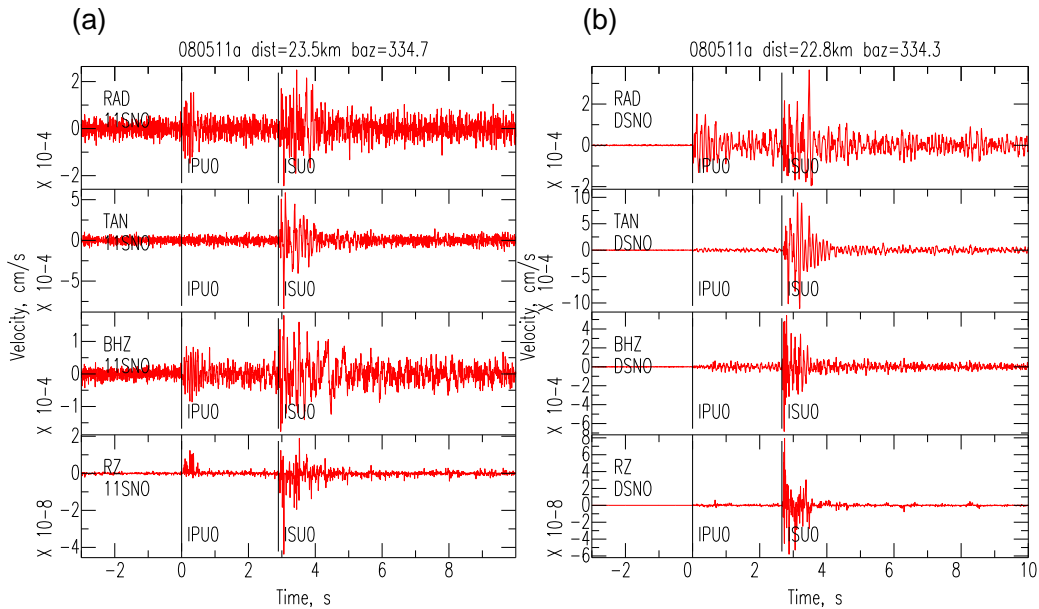


Figure 22: Seismograms of the typical mining event of MN2.6 that occurred on 11 May 2008 in the Vale Creighton mine, at 23 km distance and azimuth 334° from the SNO Lab. Seismograms are rotated to the system coordinates of the source for visual picking operations using polarisation properties of arriving waves. (a) Surface station 11SNO. (b) Underground station DSNO.

Figure 23 presents the smoothed Fourier amplitude spectra of acceleration (FACCN), calculated separately for the average horizontal component (Figure 23a) and the vertical component (Figure 23b) for a typical mining-related event – an event of MN2.6 that occurred on May 11, 2008 in the Vale Creighton mine at 23 km distance and azimuth 334° from the SNO Lab (seismograms of this event recorded at SSNO and DSNO stations are shown in Figure 22). Note that this event occurred close to the SUNO station, which is why the SUNO amplitudes are markedly higher than those at the SNO stations. The standard FACCN spectra usually are calculated for S-waves (Figures 23a and 23b). For verification, calculations have also been made for the whole seismograms including both P and S waves (Figures 23c and 23d).

Response spectra may offer some advantages in comparison to Fourier spectra, in that response spectra have a smoother behaviour with frequency, and are less influenced by noise, because they reflect the peak response of an oscillator to the signal, rather than being a cumulative measure. Therefore, response spectra are also used to examine this issue. Figure 24 shows 5% damped pseudo-acceleration response spectra (PSA) for the same typical event, again for S waves and the whole P+S record, for horizontal and vertical components separately. From comparison of S- and P+S-waves spectra presented in Figure 23 and Figure 24 it can be concluded that the spectra are very similar for all stations except the noisy station LSNO. For this station, including the P-waves results in a critical increase of noise in the input data,

distorting spectra at frequencies less than 3-4 Hz, especially for horizontal components (Figure 23c and Figure 24c).

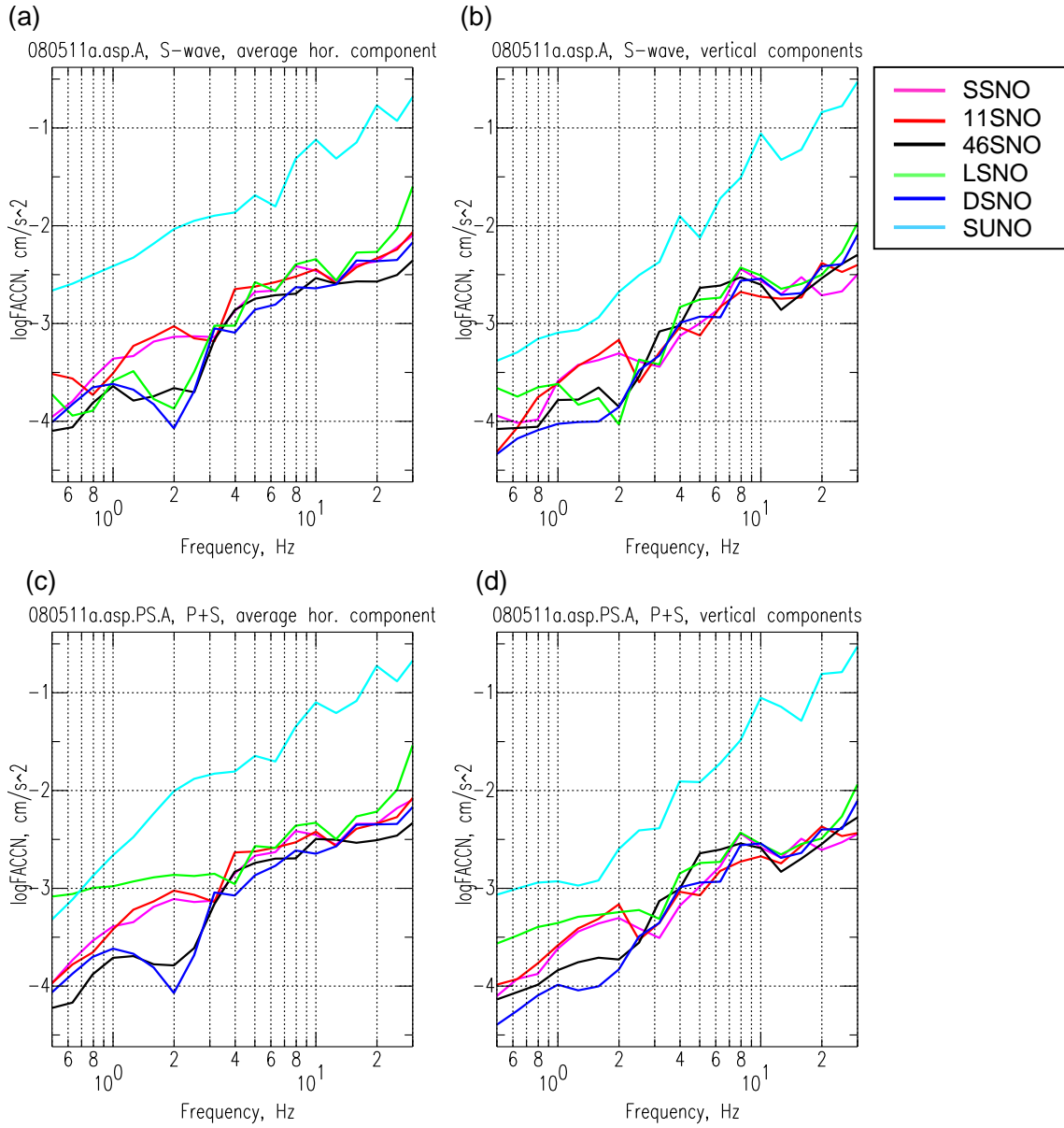


Figure 23: Fourier spectra of acceleration with log smoothing for the mining event on 11 May 2008, of MN2.6 (Figure 22). (a) Spectra for average horizontal components of S-waves observed at 5 SNO stations and the SUNO station. (b) The same as in (a) but for vertical components. (c) Spectra for average horizontal components calculated for the whole records including both P and S waves. (d) The same as in (c) but for vertical components.

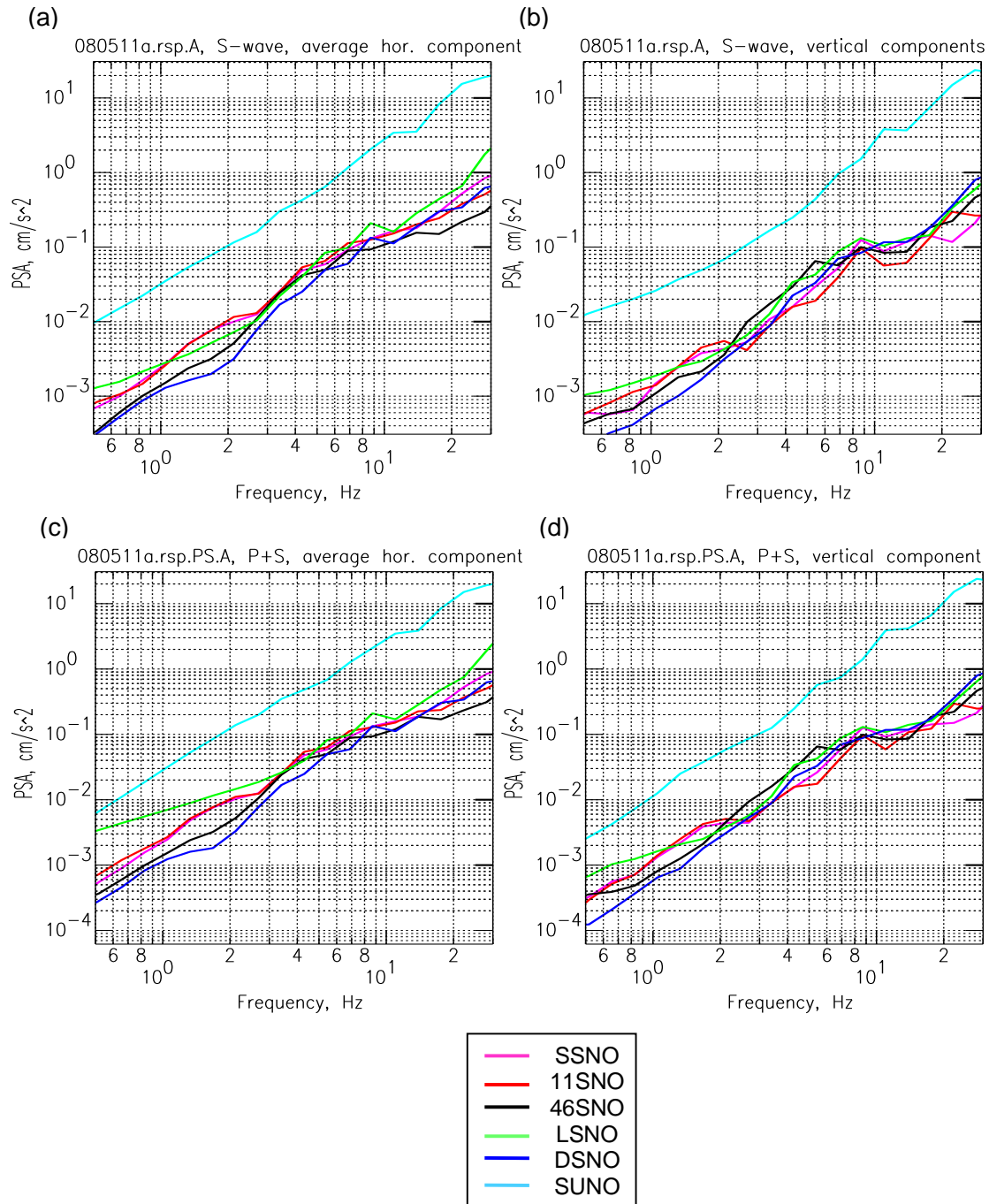


Figure 24: Response spectra for the mining event of 11 May 2008 MN2.6 (Figure 22). (a) Spectra for average horizontal components of S-wave observed at 5 SNO stations and the SUNO station. (b) The same as in (a) but for vertical components. (c) Spectra for average horizontal components calculated for the whole records including both P and S waves. (d) The same as in (c) but for vertical components.

In the case of regional and teleseismic earthquakes, data processing is the same as described above, but noise correction is not performed (noise correction is most important at high frequencies, and requires a long pre-signal window). The extracted signal includes both P and S waveforms and often a surface wave package. In contrast to the local events, P-wave amplitudes of distant earthquakes are not affected by the local network geometry. The length of the teleseismic signals is often 1000 s or more.

An example of a typical teleseismic event recorded by surface and underground SNO stations is shown in Figure 25. Input velocities are corrected for the instrument, filtered in the frequency band $f=0.03-7$ Hz, and recalculated into the system coordinates of the source. In this frequency band, waveforms recorded on the surface by SSNO station (Figure 16a) and underground by the station DSNO (Figure 16b) are very similar by inspection.

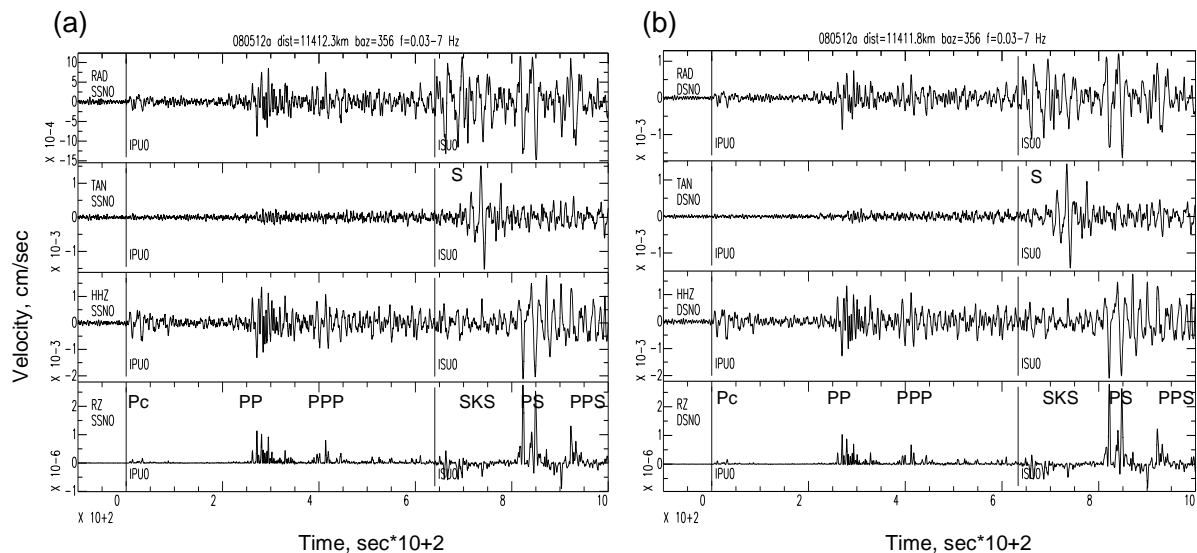


Figure 25: Seismograms of the teleseismic earthquake Mw7.9, 12 May 2008, Sichuan, China. Seismograms are corrected for the instrument, rotated to the system coordinates of the source and filtered in the band pass 0.03-7 Hz. The bottom line corresponds to the product of vertical Z and radial R components. (a) Surface station SSNO. (b) Underground station DSNO.

Differences between waveforms of teleseismic events recorded on the surface and underground become apparent in the spectral domain, as shown for the Fourier spectra of acceleration on Figure 26, and for response spectra on Figure 27. Specifically, the surface spectra begin to diverge from those underground as frequency increases, starting at 0.1 Hz for horizontal components and 0.3 Hz for the vertical. Surface stations show larger spectral amplitudes. The rising spectral amplitudes at frequencies above 1.2 to 1.5 Hz are indicative of increasing levels of noise contamination; reliable spectral ratios from teleseismic data can be obtained only for frequencies <1 Hz. Examples of regional events are presented in Figure 28 and Figure 29; the first event is the earthquake of moment magnitude (Mw) 5.4 that occurred

on April 18, 2008 in Southern Illinois, and the second one is a probable blast of MN2.5 that occurred on February 5, 2008 along the east coast of Georgian Bay.

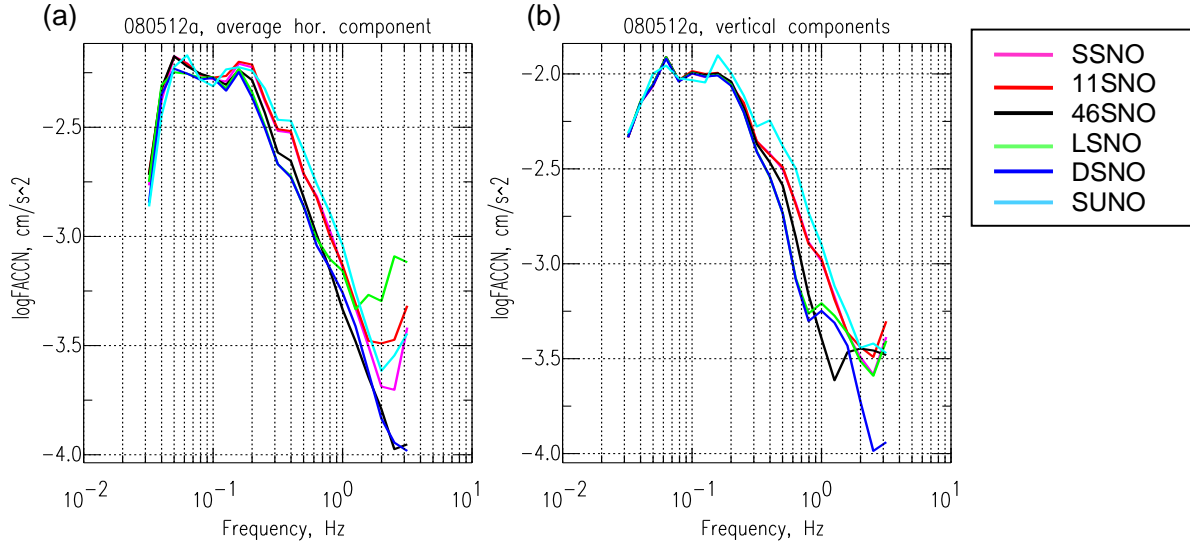


Figure 26: Smoothed Fourier spectra of average horizontal (a) and vertical (b) components of acceleration (P and S waveforms, duration 1000 s), for the teleseismic earthquake Mw7.9, 12 May 2008, Sichuan, China (Figure 25) recorded by 5 SNO stations and the SUNO station.

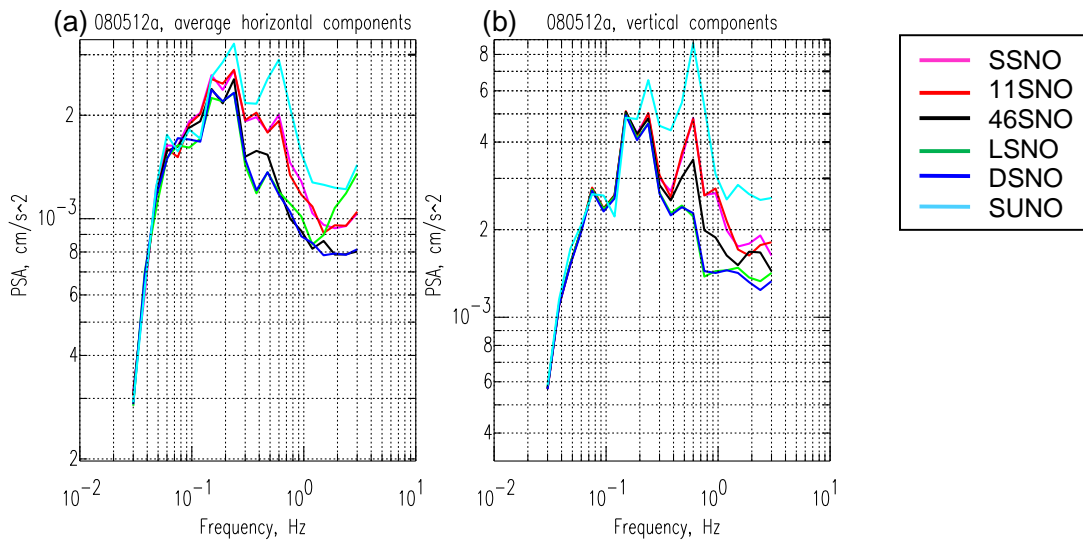


Figure 27: Response spectra of average horizontal (a) and vertical (b) components of acceleration (P and S waveforms, duration 1000 s) for the same Sichuan event as in Figure 25.

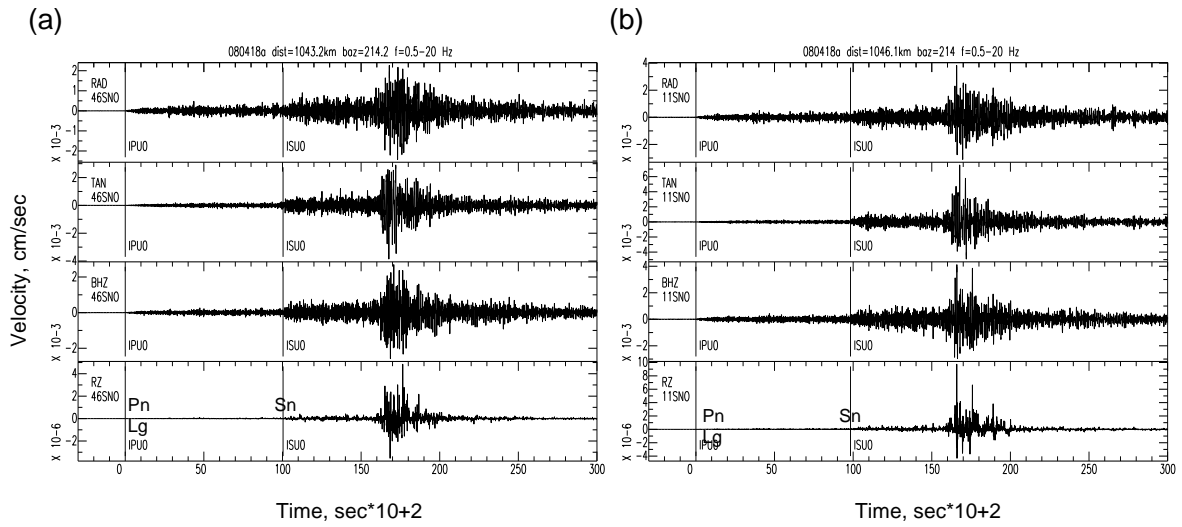


Figure 28: Seismograms of the regional earthquake Mw5.4, 18 April 2008, Southern Illinois, USA. Seismograms are corrected for the instrument, rotated to the system coordinates of the source and filtered in the band pass 0.2-5 Hz. The bottom line corresponds to the product of vertical Z and radial R components. (a) Surface station 11SNO. (b) Underground station 46SNO.

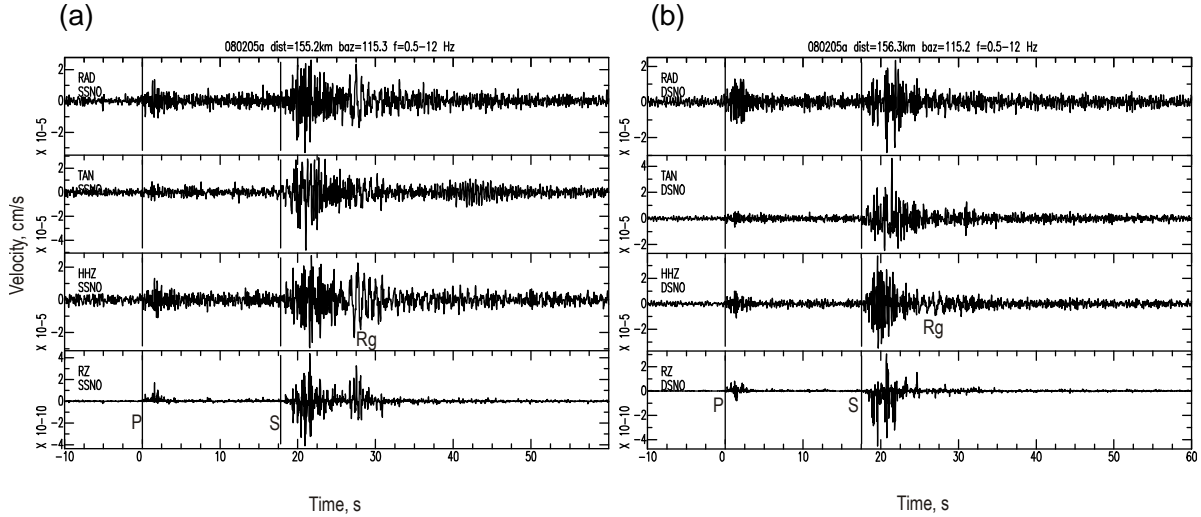


Figure 29: Seismogram of the regional event (probable blast) MN2.5, 5 Feb 2008, east coast of Georgian Bay. Seismograms are processed as in Figure 28, but filtered in the band pass 0.5-12 Hz. (a) Surface station SSNO. (b) Underground station DSNO.

Spectra of these events are shown in Figure 30 and Figure 31 (FACCN spectra), and Figure 32 and Figure 33 (response spectra). The SNR for these events is good in the frequency band 0.5-10 Hz.

As in the case of the teleseismic signals from the Sichuan earthquake, spectra presented for the Illinois and Georgian Bay events demonstrate clear amplification of surface spectral amplitudes, especially at 0.7-1.2 Hz.

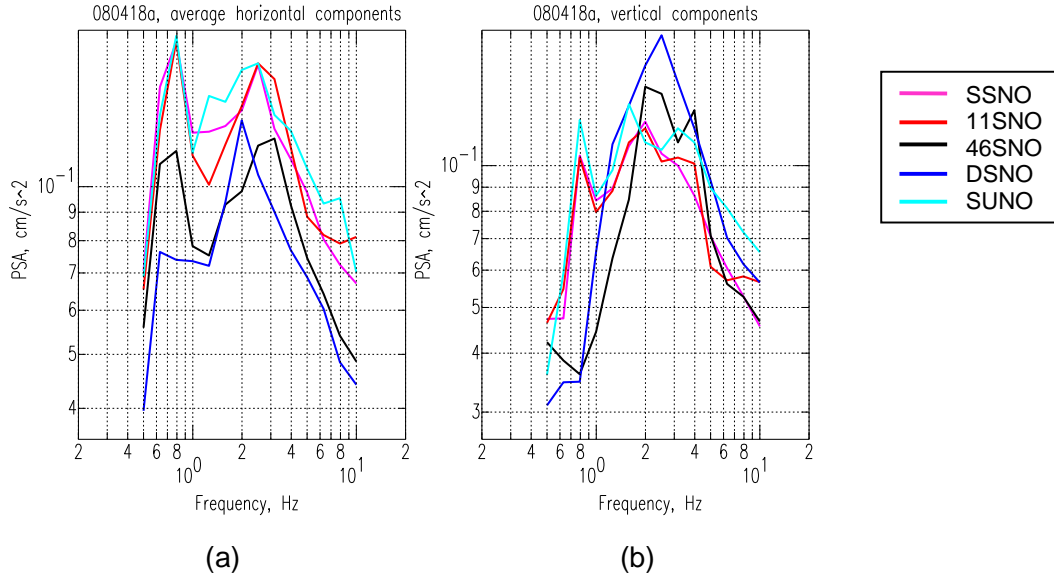


Figure 30: Response spectra of average horizontal (a) and vertical (b) components (including S and surface waves, duration 180 s) of acceleration for the Illinois event (Figure 28 and Figure 30). Designations are the same as in Figure 30.

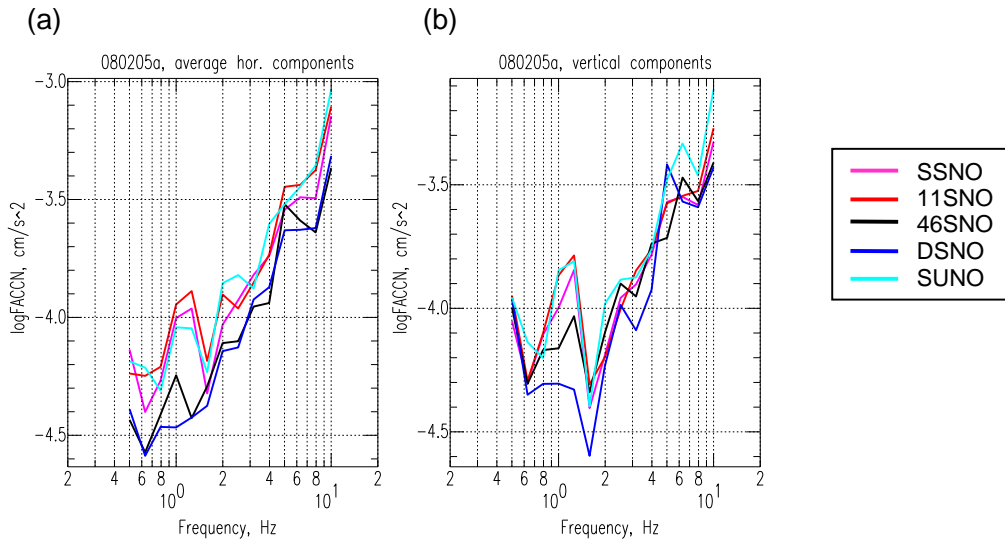


Figure 31: Smoothed Fourier spectra of average horizontal (a) and vertical (b) components of acceleration (including S and surface waves, duration 40 s), for the Georgian Bay event (Figure 29). Designations are the same as in Figure 30.

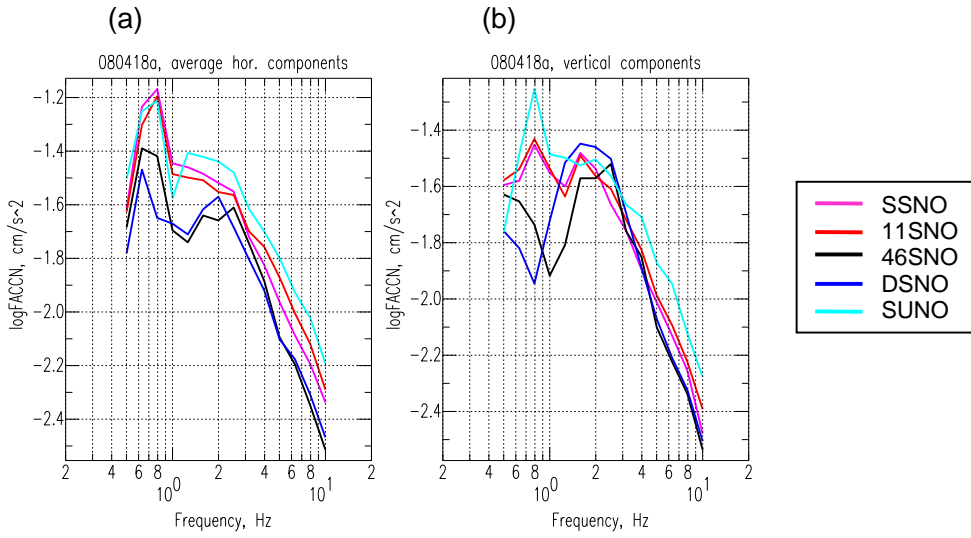


Figure 32: Smoothed Fourier spectra of average horizontal (a) and vertical (b) components of acceleration (including S and surface waves, duration 180 s), for the Illinois event (Figure 28).

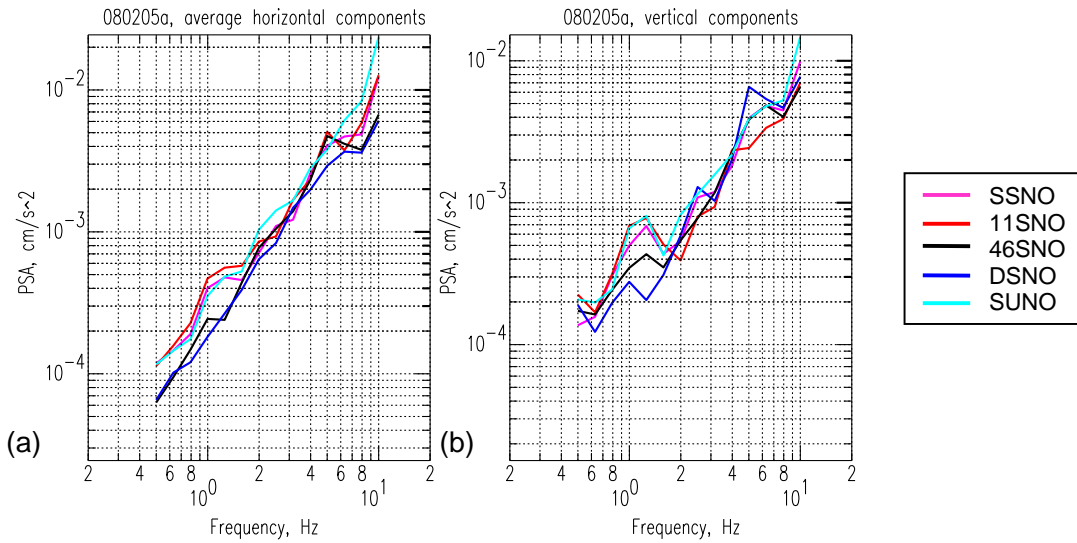


Figure 33: Response spectra of average horizontal (a) and vertical (b) components of acceleration for the Georgian Bay event (Figure 29 and 31). Designations are the same as in Figure 30.

3. COMPARISON OF MOTIONS ON SURFACE TO UNDERGROUND

Most of the signals recorded and used for calculations are at a great enough distance from SNO (8 km or more) that the distance from the event to all stations is roughly equal. Because the source effects and path effects are similar for such recordings, any differences in observed ground motions can be attributed to the site conditions of the stations, in particular, whether they are on the surface or underground. However, the data are too sparse to determine whether there are any directional effects.

3.1 ANALYSIS OF FOURIER SPECTRA

To evaluate the frequency-dependent differences in motions at the PUPS stations, the ratio of the Fourier spectrum at each station to that at every other station that recorded the same event is examined first. This provides the amplification at one station relative to another. In this exercise, the average of two horizontal components of the Fourier acceleration spectra for each record are used (where a geometric mean is calculated, by averaging log spectra); the vertical component is considered separately. There are ideally 6 pairs of surface to underground ratios for each event: SSNO/46SNO, SSNO/LSNO (or SSNO/NSNO), SSNO/DSNO, 11SNO/46SNO, 11SNO/LSNO (or 11SNO/NSNO), and 11SNO/DSNO. In practice, local noise from mine activities often eliminates one or more records (see sections 2.3 and 2.4). These ratios show significant variability from one event to another, indicating that the relationship has a significant stochastic element, and cannot be robustly determined from a small number of recordings. The noise at some stations may also complicate the interpretation of the ratios, as it contributes to the scatter in results.

To confidently establish the relative amplitude ratios between stations requires collection of a large number of events. The number of events is important, as the standard error of the mean is the standard deviation of observations divided by the square-root of the number of observations, N . As N grows, the standard error of the mean will decrease, allowing a more confident determination of the overall trends, even though variability from event-to-event may remain high.

In this chapter, variability of spectral ratios, and their strong dependence on epicentre distance, is demonstrated using examples from typical events. To better understand this dependence, the database is subdivided into 7 groups: $\Delta=8-40$ km (97 events), $\Delta=40-80$ km (9 events), $\Delta=100-150$ km (8 events), $\Delta=150-250$ km (22 events), $\Delta=250-900$ km (31 events), $900-1200$ km (4 events), and $\Delta>3500$ km (73 events). Average spectral ratios are estimated for every group and then compared. Summing all individual spectral ratios for all events within each group, and dividing the result by the number of observations, gives the average spectral ratios for horizontal and vertical components for the group.

3.1.1 A few examples of spectral ratios for typical event variants

In Figure 34 and Figure 35, ratios of surface-to-underground motions in the frequency band 0.5-30 Hz are displayed for the typical mining event of MN2.6, on May 11, 2008 (Figure 22 and Figure 23), as calculated for S waves (Figure 34) and for the whole seismogram including both P and S waves (Figure 35).

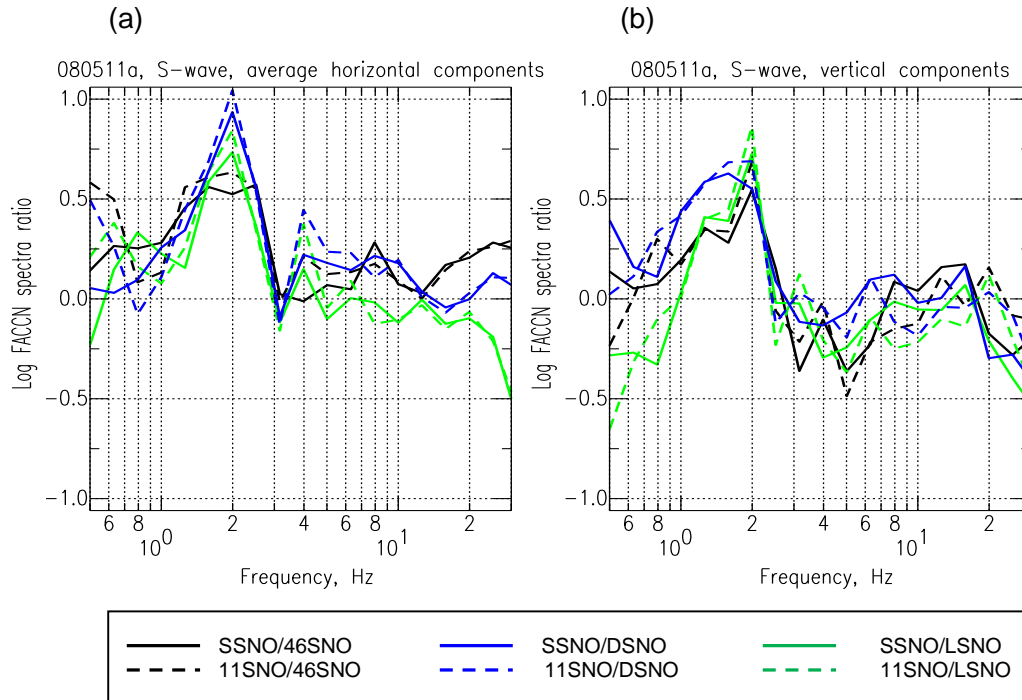


Figure 34: Log ratios of surface motions to underground motions for the typical mining event MN2.6 on 11 May 2008 calculated for Fourier spectra of S-waves. (a) Average horizontal component. (b) Vertical component.

It is clearly seen that for stations with an acceptable level of noise, the inclusion of P-waves in the analysis does not significantly affect the results. At the noisy station LSNO, the inclusion of P-wave energy adds more noise, resulting in distortion of the spectral ratios. It is concluded that, in general, the behaviour of underground stations relative to those on the surface can be determined using just the S-wave window. Because this is the window of most engineering interest, it will be the focus of the remainder of the study in the case of local and regional events. For teleseismic earthquakes, the whole waveform for spectral estimations, including P, S and the surface wave package (if the time window is not too long), are used. Inclusion of P waves is sometimes effective to broaden the spectral band of the signal to the high frequency area.

Note the clear, apparent site effect at surface stations relative to those underground for the typical mining event, with a strong relative amplification near 2 Hz by nearly an order of magnitude on both the horizontal and vertical components. By contrast, there is a modest apparent de-amplification of vertical components at 3-6 Hz on the surface. This pattern is typical of our observations from local events.

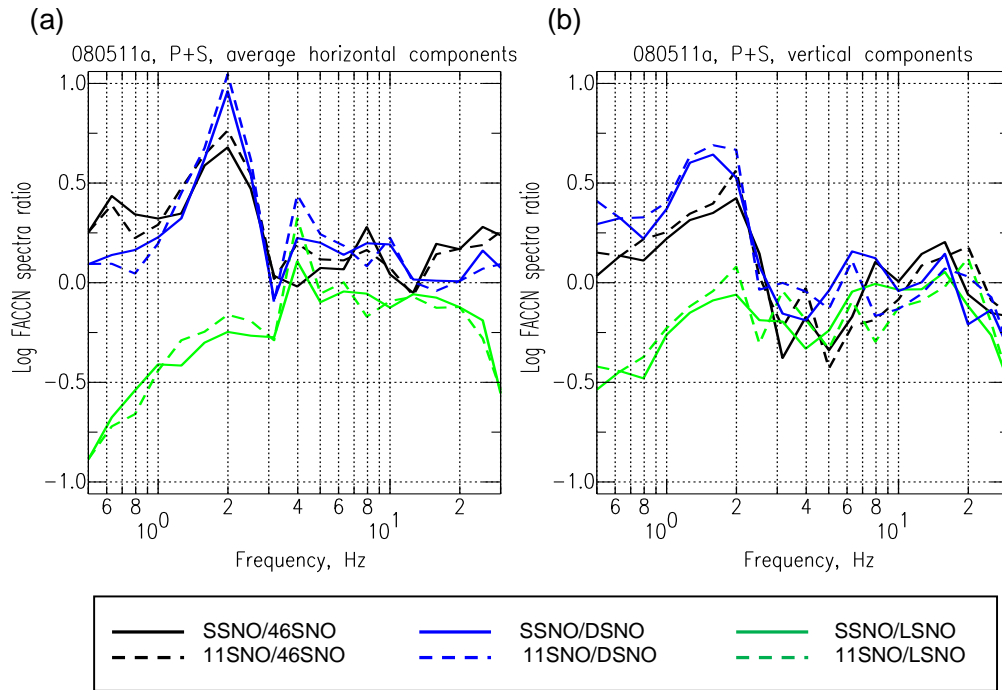


Figure 35: Log ratios of surface motions to underground motions for the typical mining event MN2.6 on 11 May 2008, calculated for Fourier spectra of P- and S-waves. (a) Horizontal components. (b) Vertical components.

Figures 36 to 38 present ratios of the Fourier spectra at lower to intermediate frequencies: 0.03-3 Hz as estimated from records of the teleseismic Mw7.9 earthquake that occurred on May 12, 2008 in Sichuan, China (Figure 36); 0.5-10 Hz, as estimated from records of the distant regional event of Mw5.4 on April 18, 2008 in Southern Illinois (Figure 37), and from records of the close regional event of MN2.5 (Figure 38) that occurred along the east coast of Georgian Bay on February 5, 2008.

Waves with frequencies >1 Hz are strongly attenuated and scattered during propagation over long distances, resulting in rapidly-increasing noise contamination at frequencies above 1 Hz for teleseismic events (Figures 26 to 27 and Figure 36), or above 10 Hz for regional Illinois events (Figure 37b). Therefore, spectral ratios determined from teleseismic and regional observations are probably not reliable at $f > 1$ Hz and $f > 10$ Hz, respectively. Spectral ratios calculations were made for the Sichuan earthquake using the entire body-wave window, and compared to those made using just the P-wave package (Figure 36a and Figure 36b, respectively). For the Illinois earthquake, the spectral ratios were compared based on the group of S and surface waves and those based on just the P-waves (Figure 37a and Figure 37b). Only the S+Lg/Rg window was used for the Georgian Bay event (Figure 38). It is difficult to calculate spectra for the P-wave window in the case of close regional and local events, because they are usually characterised by low SNR. Moreover, the duration of this window is too short for close local events for such estimations.

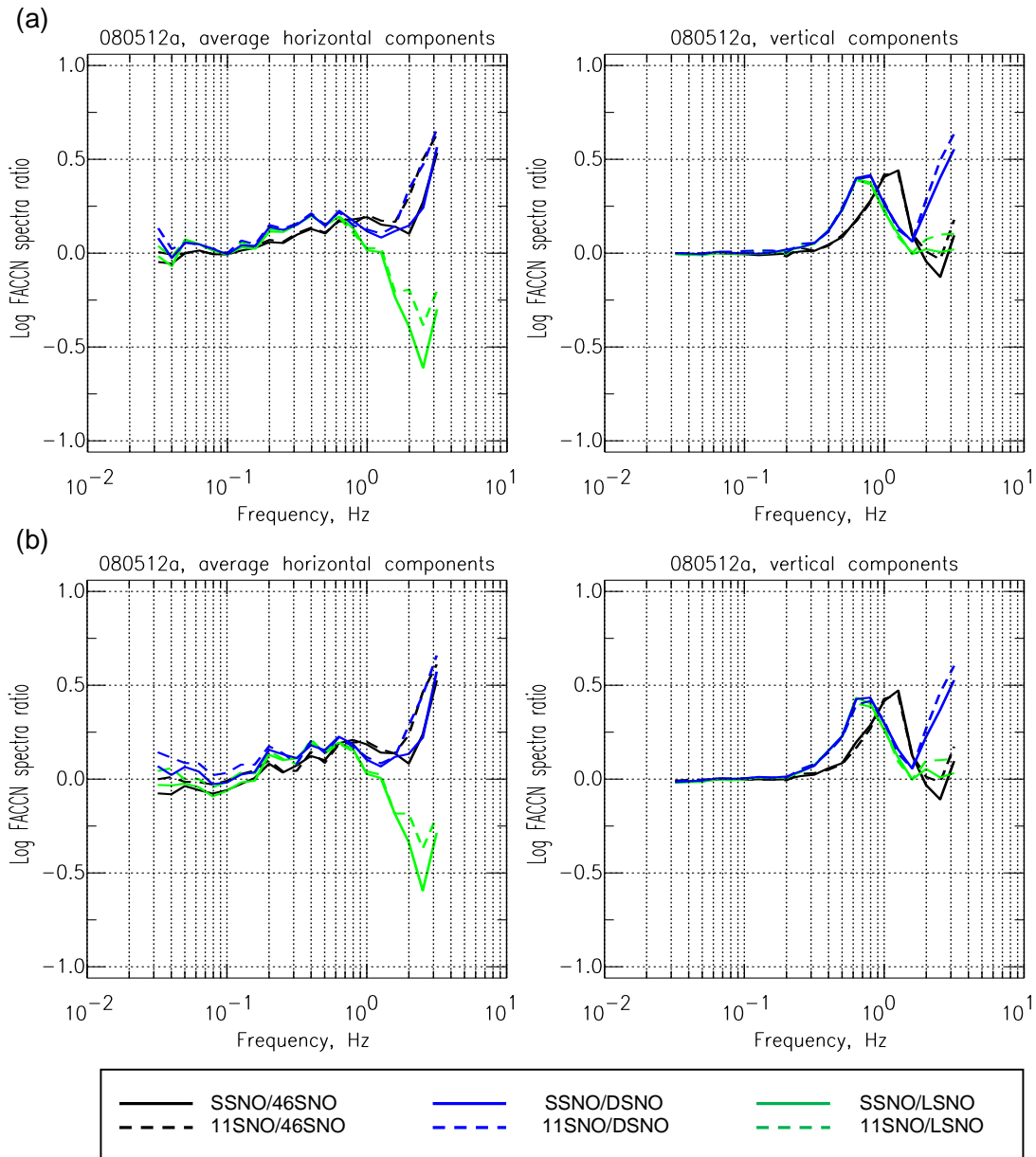


Figure 36: Log ratios of surface stations to underground stations for teleseismic event Mw7.9, 12 May 2008, Sichuan, China (Figure 25) calculated for Fourier spectra of average horizontal component (on the left) and vertical component (on the right). (a) For 1000 s records including P- and S-wave groups. (b) For P-wave group only (55 s).

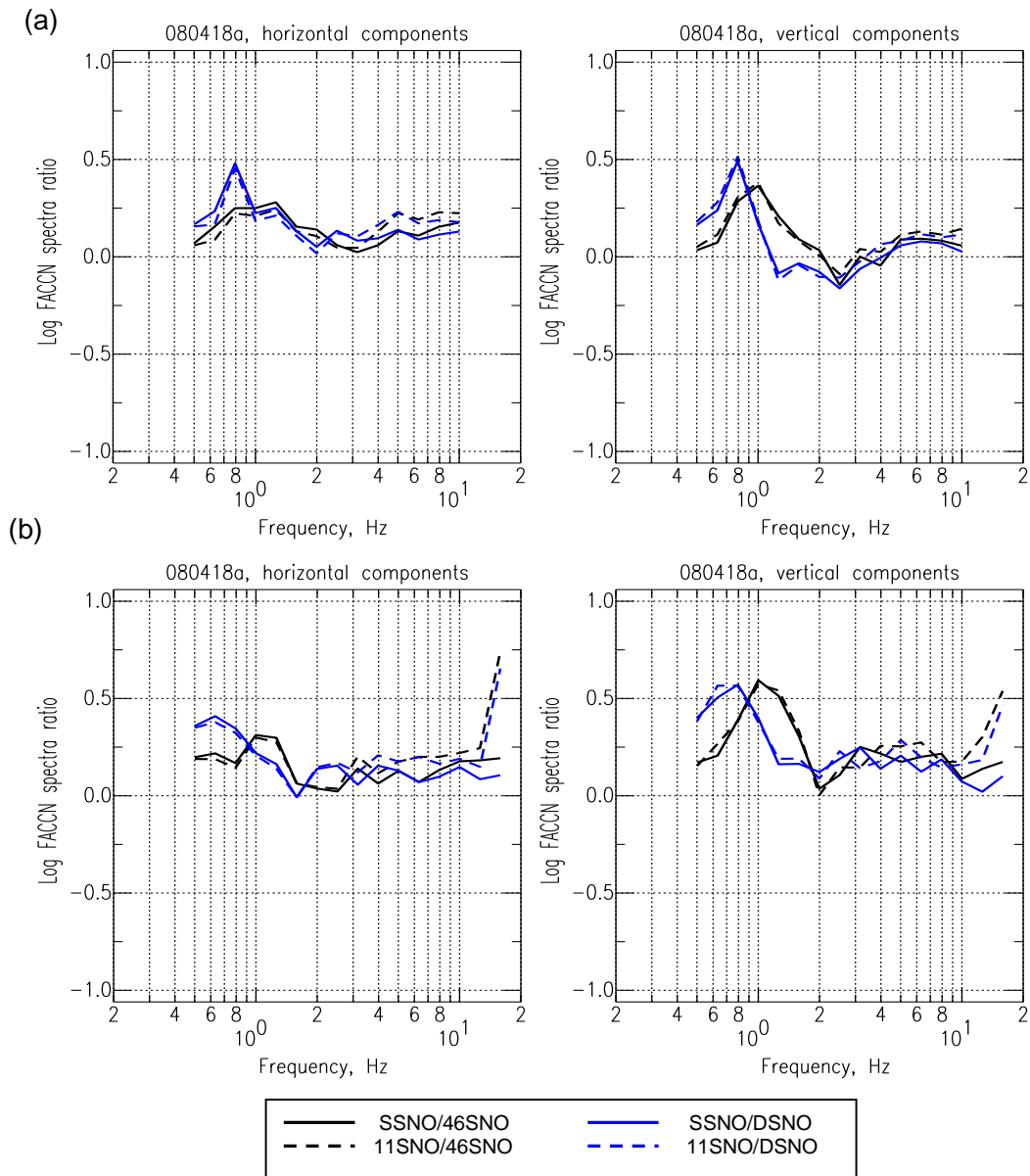


Figure 37: Log ratios of surface stations to underground stations for the regional event Mw5.4, 18 April 2008, Southern Illinois (Figures 28, 30 and 32) calculated for Fourier spectra of average horizontal component (on the left) and vertical component (on the right). (a) For S and Lg-waves (180 s). (b) For the P-wave package (90 s).

It is remarkable that spectral ratios for teleseismic events are not sensitive to the choice of window. Regardless of whether the P+S waveform package, or just the P-wave package, is used, a peak amplification of surface stations relative to those underground at a frequency near 1-Hz is observed. Furthermore, there is a relative shift of this peak to lower frequency as the depth of the underground station increases; this is especially evident for the vertical component.

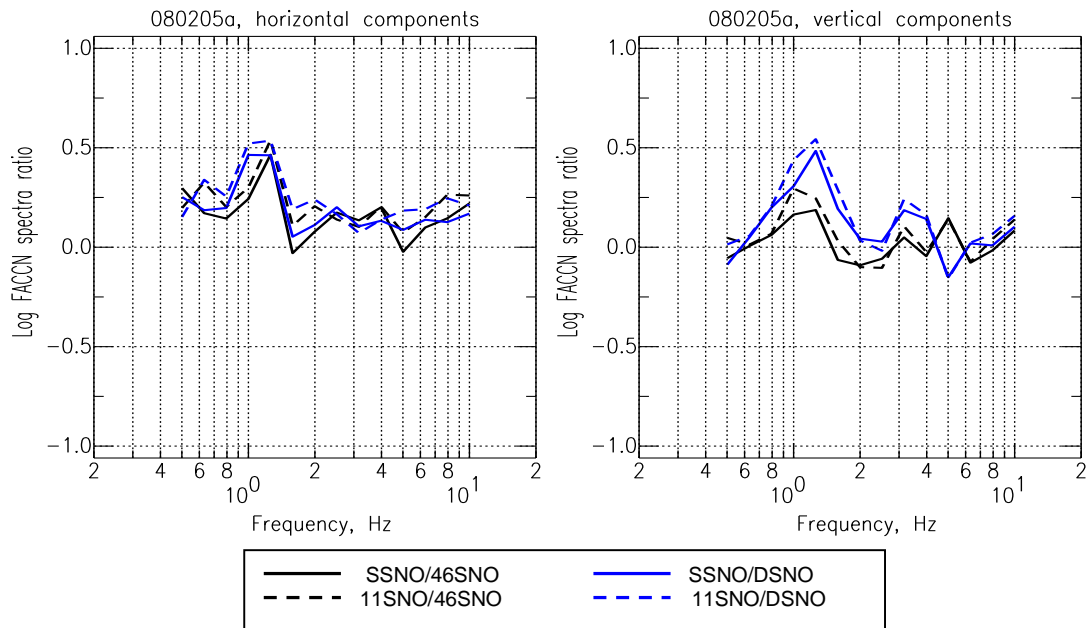


Figure 38: Log ratios of surface stations to underground stations for the Georgian Bay regional event MN2.5, 5 February 2008 (Figures 29, 31 and 33) calculated for Fourier spectra of average horizontal component (on the left) and vertical component (on the right) including both S and Rg/Lg waves (40 s).

In the case of the Illinois earthquake, the form of spectral ratios calculated for P-wave and for S+Lg waves is again very similar. The position of the peaks is the same, but there is an important difference: for the S+Lg window, amplification of surface stations relative to those at intermediate depth (1.4 km at 46SNO) is less than that at the deeper level (2.1 km at DSNO), while for the P-phase window their amplitudes are equal. In the case of the Georgian Bay event, for spectral ratios calculated for the S+Lg/Rg window the same phenomenon is observed (Figure 38).

When the spectral ratios from regional events (Figure 37, epicentre distance $\Delta=1047$ km, and Figure 38, $\Delta=156$ km) are compared to those from close local events (Figures 34 to 35, $\Delta=23$ km), it is observed that the local events show peak amplification of motion near 2 Hz, while the peak from the regional data moves to 0.8-1.2 Hz as epicentral distance increases.

The most reasonable explanation is that the peak amplification for the local events is due to the influence of short-period surface waves, whose amplitudes decrease as depth increases (this is shown later in more detail in Section 3.4); more pronounced de-amplification at the deeper station DSNO in comparison to the shallower 46SNO at local (Figure 34) and regional (Figure 37 and Figure 38) distances supports this conclusion. At longer periods ($T > 3-5$ s, see Figure 36), the wavelengths of surface waves exceed the depth of the SNO stations underground, and thus the effect of surface waves on the ratio would be less pronounced as period lengthens. The observation that the peak shifts to lower frequencies as depth of the station increases may be related to the variation of medium properties with depth.

3.1.2 Average spectral ratios: nearest ($\Delta=8-40$ km) versus most distant ($\Delta>3500$ km) events

It is useful to contrast the ratios of surface to underground motions for local and very distant events. There are 97 nearby local events and 73 teleseismic events. Their average spectral ratios are obtained by summing spectral ratios for all events for each group, and dividing the result by the number of observations; this is done separately for horizontal and vertical components. Figure 39 shows such ratios for SSNO on the surface relative to the 46SNO station underground, for teleseismic data (Figure 39a, frequency band 0.05-2 Hz) and close local data (Figure 39b, frequency band 0.5-30 Hz). Note that the ratios are plotted in log units, so that a value of 0.3 corresponds to amplification by a factor of two. The standard deviations of the ratios are also shown to indicate the high event-to-event variability in the ratios. Surface motions are higher than those underground by 0.3 to 0.5 log units over the range from 1 -3 Hz, corresponding to factors of two to three. At low frequencies (<0.2 Hz), surface and underground motions are essentially equal. At high frequencies (>6 Hz), horizontal-component motions are very similar on the surface and underground, while vertical motions are actually somewhat lower (0.1-0.2 units) on the surface.

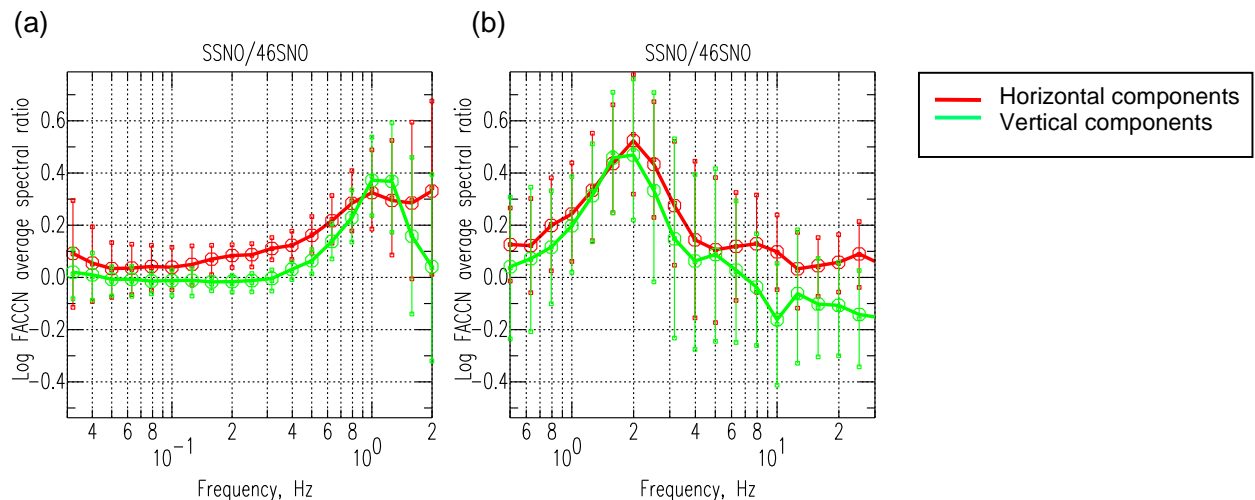


Figure 39: Mean log ratios of the surface station SSNO to underground station 46SNO. Error bars correspond to the standard deviations of these ratios. (a) From database of 73 teleseismic earthquakes ($\Delta>3500$ km). (b) From database of 97 close local mining events ($\Delta=8-40$ km).

Figure 40 presents in more detail the average spectral ratios for each pair of surface-underground stations for the database of 73 nearby events ($\Delta=8-40$ km), but with standard error bars instead of standard deviation (to emphasize uncertainty in the mean, rather than variability of observations). Station LSNO is not included due to noise problems. It is seen, first of all, that surface stations SSNO and 11SNO provide very similar ratios (relative to each underground station) despite the fact that the 11SNO station is noisier than the SSNO station. For the deeper DSNO station, the spectral ratios are similar to those for 46SNO, but have some important distinctions. In particular, the peak amplification at frequencies 1.6-2.0 Hz is higher at DSNO and slightly shifted towards lower frequency, reaching 0.7 log units (factor of 5) for vertical components; this may be due to the greater depth of DSNO, which would attenuate the short-period local surface waves even more than for 46SNO. At higher frequencies (3-30 Hz), horizontal components at DSNO are clearly suppressed, by about 0.2 log units (factor of 1.6).

For DSNO at, frequencies greater than 6 Hz, vertical components at the surface are approximately equal to those at depth.

The distribution of standard deviations with frequency is shown in Figure 41. The variability of observations is relatively uniform; there is a small local minimum of deviations at 20 Hz, and increasing values at the edges of the frequency interval: at $f < 0.8\text{Hz}$ and $f > 30\text{Hz}$.

Figure 42 and Figure 43 plot the spectral ratios of surface to underground stations for 73 teleseismic events (frequency band 0.05-2 Hz), along with their standard errors. Again, it is observed that amplification of motions for the surface stations starts at $f > 0.1\text{ Hz}$ for horizontal components, or at $f > 0.3\text{ Hz}$ for the vertical, becoming large for $f > 0.5\text{ Hz}$. Recall that the spectral ratios at $f > 1\text{ Hz}$ are unreliable for teleseismic events; for higher frequencies regional and local events must be relied upon.

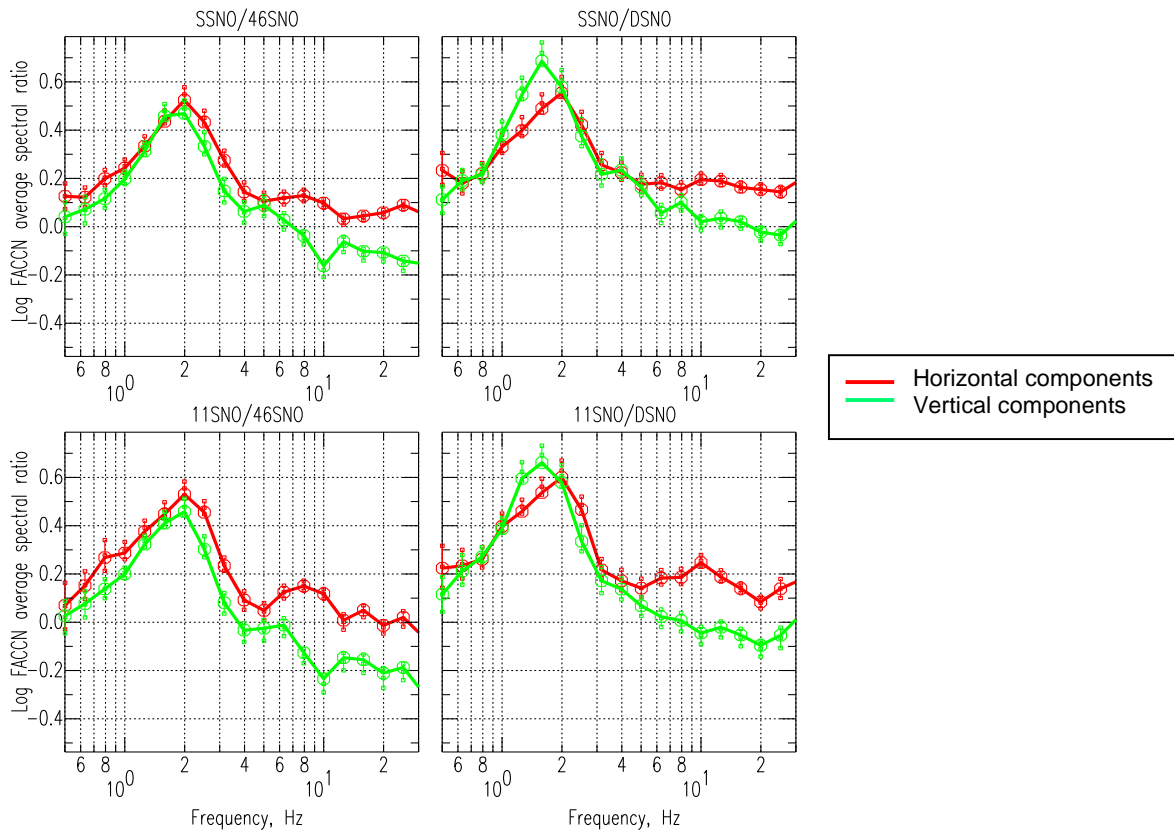


Figure 40: Mean log ratios of the surface stations SSNO (upper line) and 11SNO (low line) to underground stations 46SNO (on the left) and DSNO (on the right) calculated from database of 97 close local mining events ($\Delta=8-40\text{ km}$). Error bars correspond to the standard errors of these ratios.

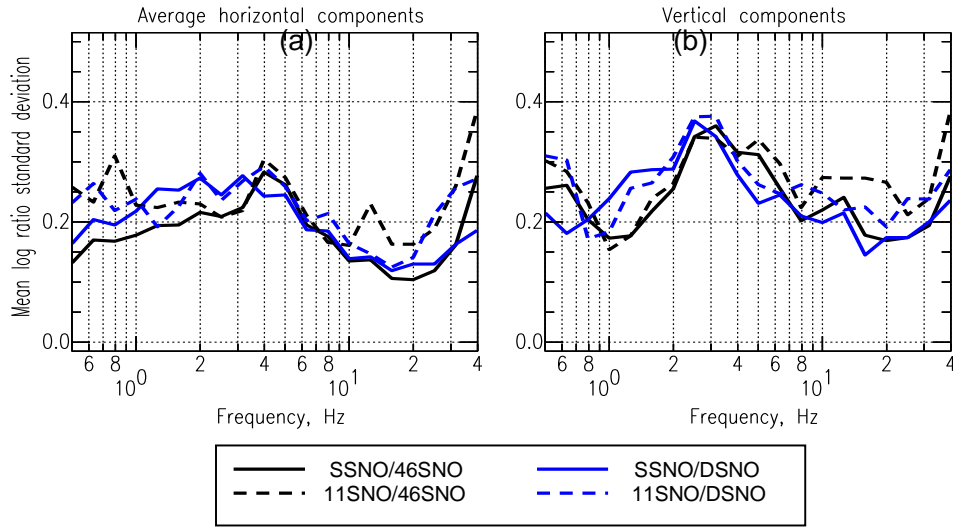


Figure 41: Distribution of standard deviations over frequency for the mean log ratios shown in Figure 40. (a) Horizontal components. (b) Vertical components.

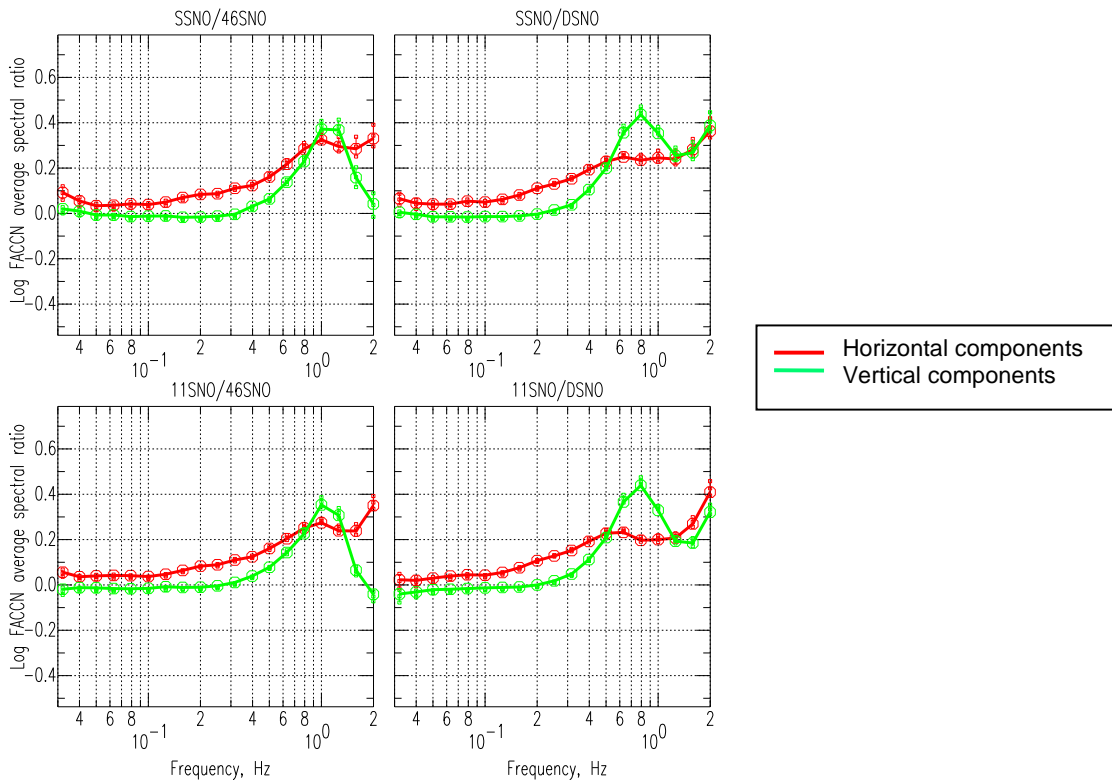


Figure 42: Mean log ratios of the surface stations SSNO (upper line) and 11SNO (low line) to underground stations 46SNO (on the left) and DSNO (on the right) calculated for 73 teleseismic ($\Delta>3500$ km) earthquakes. Error bars correspond to the standard errors of these ratios.

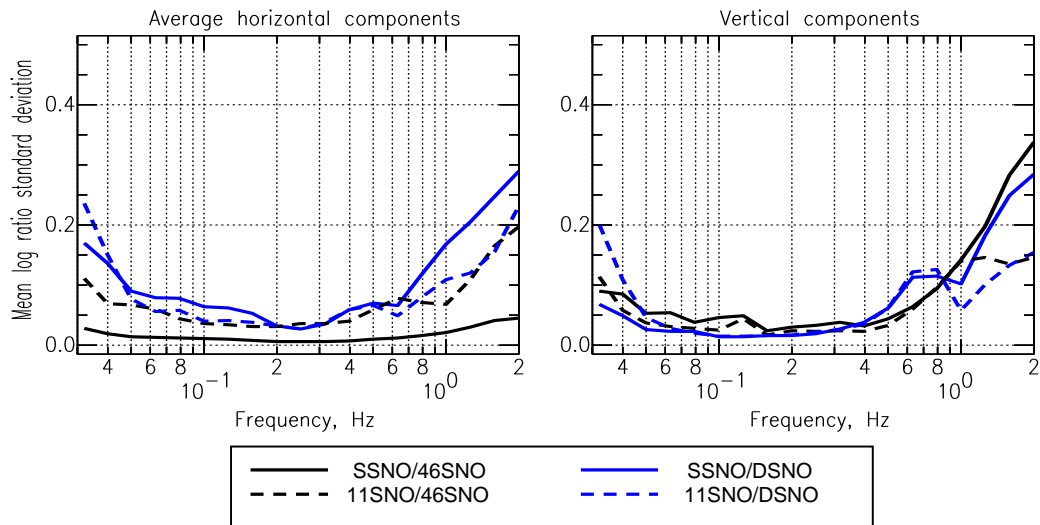


Figure 43: Distribution of standard deviation over frequency for mean log ratios shown in Figure 42. (a) Horizontal components. (b) Vertical components.

In Figure 42, a relative shift of the peak amplification towards lower frequency is observed as the depth of the underground station increases, especially for the vertical component. In order to better understand the amplitude relationships between stations, the ratio of the two surface stations (SSNO/11SNO), and the two underground stations (46SNO/DSNO), are plotted relative to each other. The high-frequency behaviour is shown in Figure 44, based on the local events database, while the low-frequency behaviour is shown in Figure 45, based on the teleseismic events database.

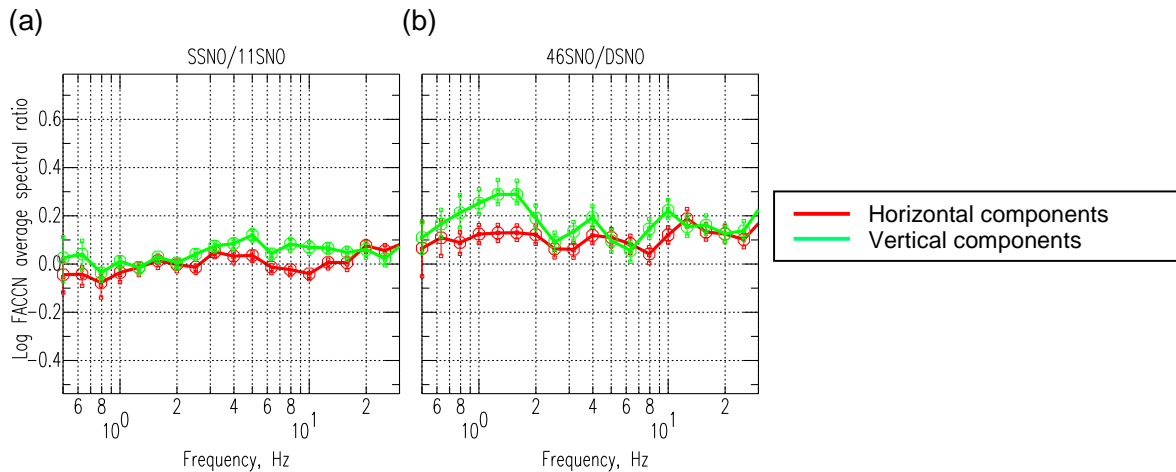


Figure 44: Mean log ratios (from the local events database) of (a) the surface stations SSNO and 11SNO and (b) underground stations 46SNO and DSNO. Error bars plotted correspond to the standard errors of these ratios.

Figure 44a and Figure 45a support the conclusion about the similarity of surface-underground spectral ratios for SSNO and 11SN0 stations: their direct log ratio varies near zero, deviating to both sides by no more than 0.1 log units (i.e., a factor of 1.3). This suggests that these stations, located very close to each other on the surface, have nearly-identical underlying geological structures and produce similar site responses.

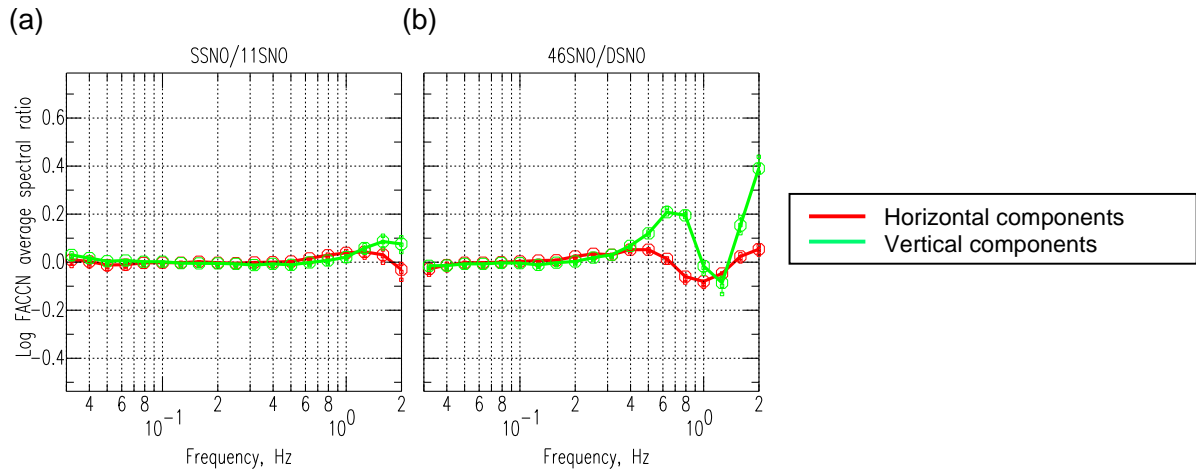


Figure 45: Mean log ratios (from the distant events database) of (a) the surface stations SSNO and 11SN0 and (b) underground stations 46SN0 and DSNO. Error bars plotted correspond to the standard errors of these ratios. Designations are the same as in the previous figure.

On the other hand, the two underground stations, 46SN0 and DSNO evidently are not identical in terms of their responses. Being separated by almost 700 m in the vertical direction and 2 km horizontally, they are located on the opposite sides of the rim of the ore bodies (which are in the form of a massive sulphide lens) in different rocks, granite gabbro (46SN0) and norite rock (DSNO) (Figures 1 to 2). As seen on Figure 44b and Figure 45b, the average Fourier spectra of acceleration at the shallower station (46SN0) are higher than those at the deeper station (DSNO) at frequencies $f > 0.4$ Hz, especially for vertical components. The peak difference reaches 0.2 log units at about 2 Hz for local data, and at 0.7 Hz for teleseismic data. This is the cause of the relative shift of the peak amplification towards lower frequency with depth of the underground station (as seen in Figures 36 to 37, and Figures 40 and 42).

As noted earlier, LSNO was moved to a quieter location during 2009. The relocated station (under the new name NSNO) enriched the database with records of 22 local events, 38 regional ones, and 87 teleseismic earthquakes. Figure 46 shows spectral ratios for 14 nearby events which have NSNO records. The NSNO records are similar to those at DSNO, but have higher noise at $f < 1$ Hz.

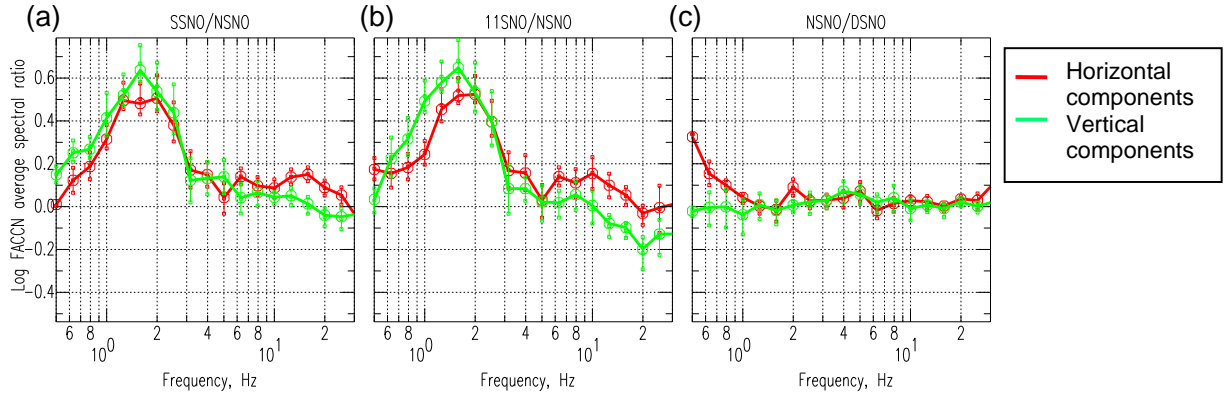


Figure 46: Mean log ratios (from the 14 close local events database including NSNO records) of (a) SSNO/NSNO, (b) 11SNO/NSNO and (c) NSNO/DSNO. Error bars correspond to the standard errors of these ratios.

3.1.3 Average spectral ratios for local events at a range of distances ($\Delta=8-100$ km)

The last year of the PUPS experiment introduced a new type of data; records of 9 local events in the intermediate distance range from 40-80 km were obtained (Table 4). Spectral ratios of the surface station SSNO to underground stations 46SNO and DSNO calculated for these events are shown in Figure 47 (green lines) in comparison with those for the 97 nearby events discussed in the previous section (yellow lines in Figure 47, the same as in Figure 40). Moreover, in 2009, a dozen blasts at distances 8-80 km were recorded that had enhanced high frequency content; 8 of these had SNR sufficiently high to estimate spectra in the broad frequency band 0.5-100 Hz (black dotted lines in Figure 47).

In contrast to the typical mining events, these blasts have a more pronounced and longer coda. Their frequency composition is shifted to higher frequencies, resulting in good SNR even at $f > 40$ Hz (see Figure 48). Note that the blast whose spectra are shown in Figure 48 (left) has smaller magnitude and is more distant than the typical mining event shown on the right, but its spectral amplitude at $f > 50$ Hz exceeds that of a typical mining event.

Figure 49 shows spectral ratios derived from the two high-frequency blasts having the best SNR at all stations. Note that high-frequency ($f > 40$ Hz) differences in spectral ratios between surface (SSNO) and underground stations DSNO and NSNO are likely due to apparent site effects between these two underground stations at very high frequencies, even though both are at the 2.1 km level.

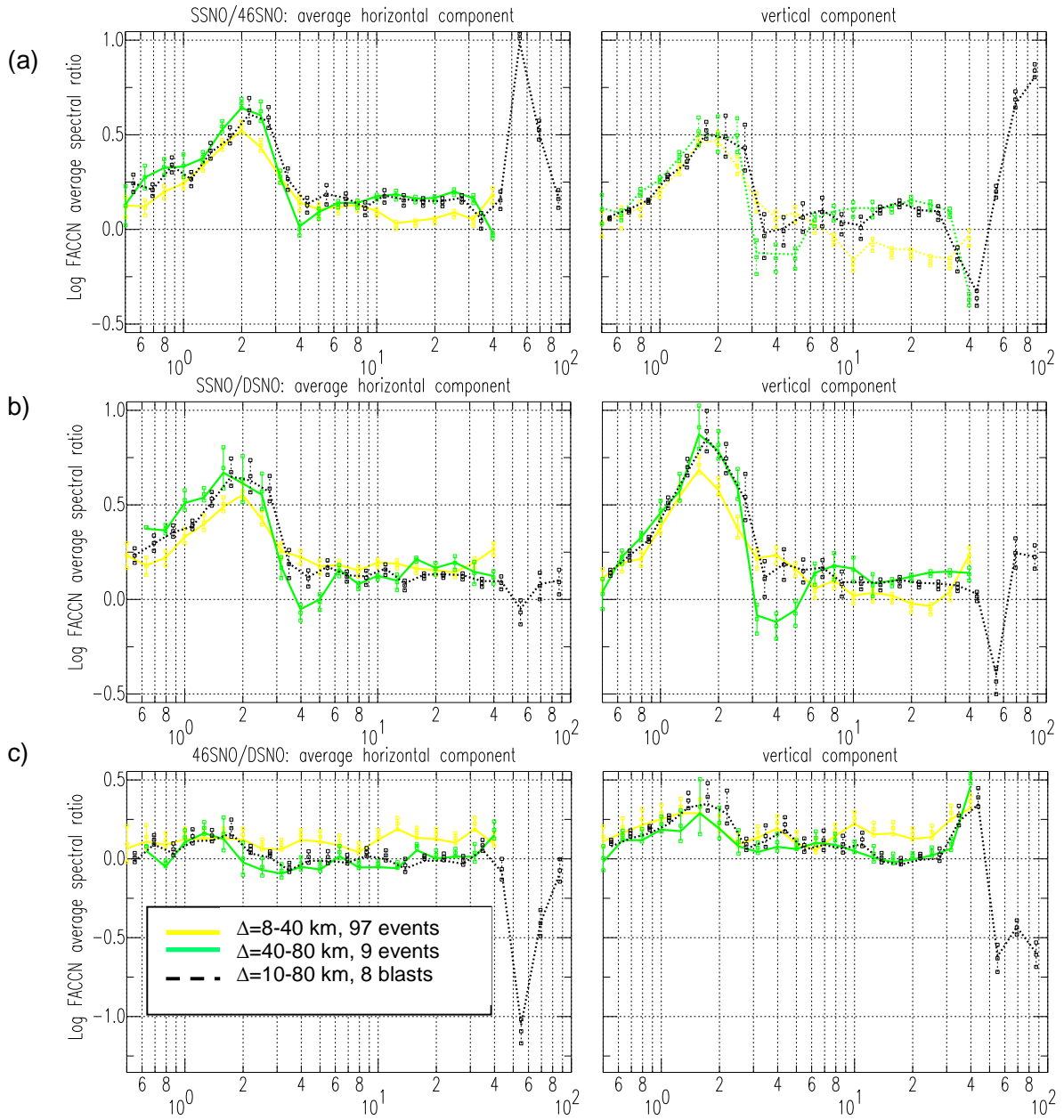


Figure 47: Mean log spectral ratios based on the data from three groups of local events. Ratios shown are (a) of the surface stations SSNO to underground stations 46SNO and DSNO, and (b) underground stations NSNO and DSNO. Error bars correspond to the standard deviation of these ratios.

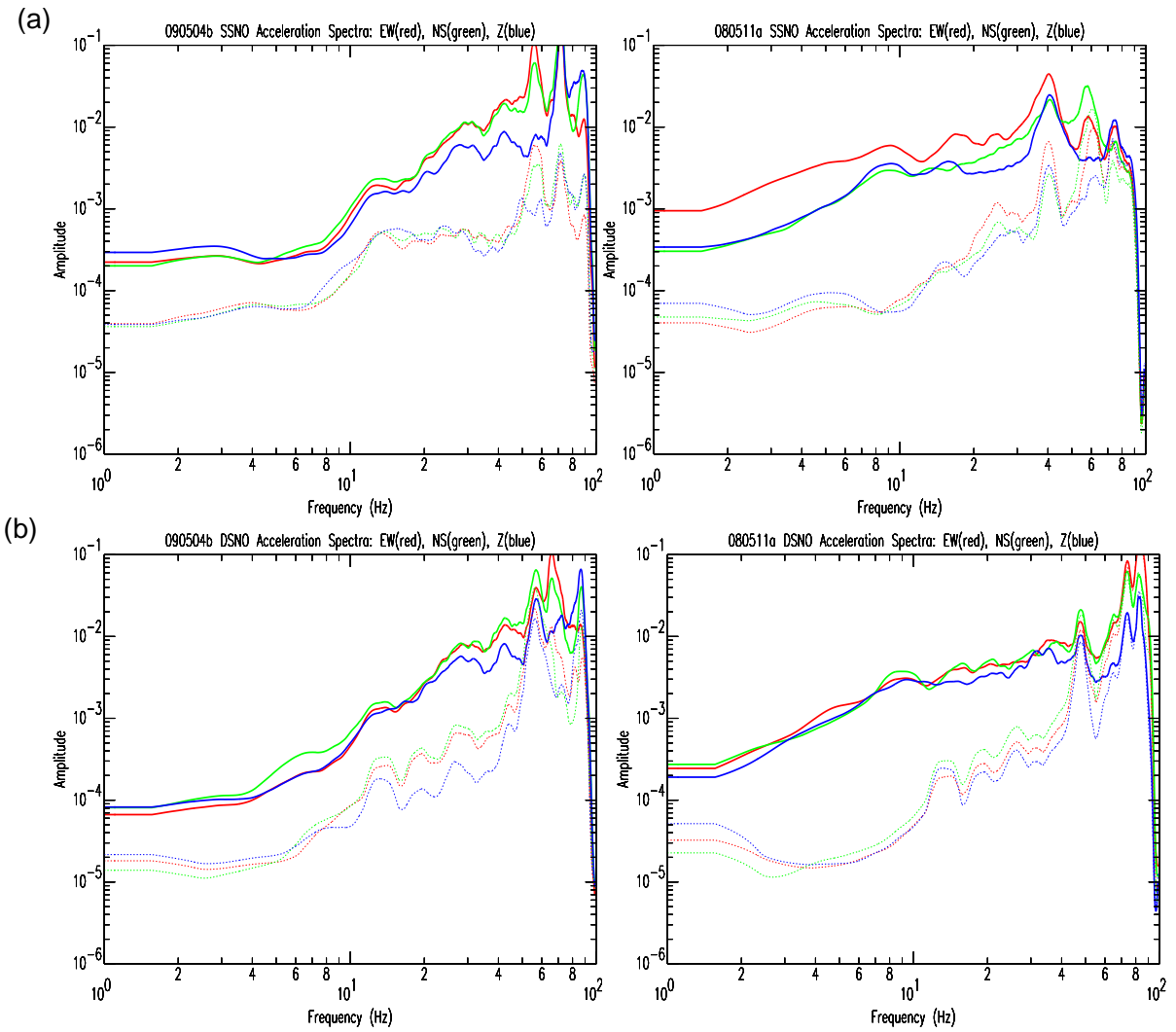


Figure 48: Comparison of spectra of acceleration (corrected for instrument, cm/s^2) of signal (solid lines) and pre-event noise (dotted lines) calculated for the M2.1 blast that occurred on 4 May 2009 at 35 km distance from DSNO (left) and the typical mining event of MN2.6, 11 May 2008, at 23 km from DSNO (right). Vertical components are shown in blue, horizontal ones in red and green.

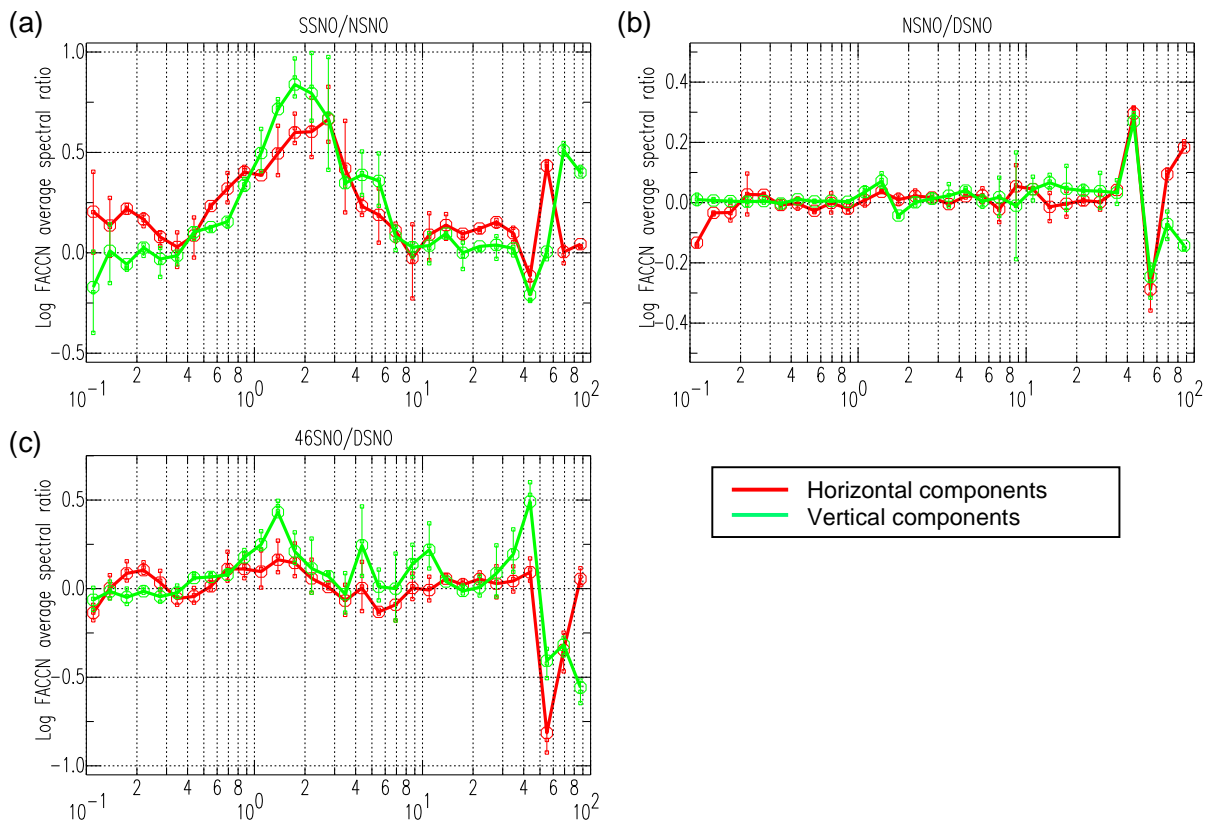


Figure 49: Mean log ratios of (a) the surface station SSNO and underground station NSNO, (b) underground stations NSNO and DSNO, and (c) underground stations 46SNO and DSNO, averaged over two blasts (# 96 and 97 in Table 4). Error bars plotted correspond to the standard deviation of these ratios.

Overall, comparing the data obtained over a range of distances, it can be concluded that at frequencies 0.5-30 Hz, the location and amplitude of the main 2-Hz spectral peak in the ratio of surface to underground motions is similar for all events in the distance range from 8 to 100 km. At higher frequencies, there are some complex effects of large amplitude that may be attributable to details of geological differences between stations. It is possible that significantly increased acoustic impedance of ore deposits between stations relative to their crystalline host rocks, which is different for every station, is relevant in the site effect here. Note that shafts with depleted ores are filled with sand, which has low acoustic impedance; this might further increase the contrasts in high-frequency site effects at mines underground. The observed difference in site responses at neighbouring stations DSNO and NSNO (located closer to the nearest ore body, Figure 1) supports such an interpretation. The 0.3 km/s step decrease in velocity at the Gabbro/Norite oblique contact of the Sudbury Structure may also explain some of the differences observed (Milkereit and Eaton, 1998). A more detailed consideration of these very high-frequency site effects is beyond the scope of this study.

3.1.4 Average spectral ratios for regional events ($\Delta=100-1050$ km)

Figure 50 presents mean log spectral ratios, based on the data from 66 regional events (frequency band 0.5-10 Hz) sorted by distance into five groups, for the surface station SSNO relative to the deep station DSNO and intermediate-depth station 46SNO, and for the underground station DSNO relative to 46SNO (Note: plots using the other surface station, 11SNO, as a reference show similar behaviour, and are not shown for brevity). Despite the uncertainty of these ratio values for the group of most distant events (800-1050 km), each point of which is estimated from only 5 events, evident general observations can be made. Overall, for regional events, the underground vertical and horizontal ground motions are lower than those at the surface over the frequency range 0.5-1.2 Hz.

In contrast to local events (Figure 47), the peak relative amplification for regional events recorded on the surface shifts from 2 Hz to lower frequencies, 0.8-1.2 Hz, and decreases in amplitude. Moreover, there is a clear dependence of the spectral peak of the ratio on epicentre distance. As distance to the event increases, the amplification peak narrows and shifts to lower frequencies on the horizontal component. On the vertical component, the peak also shifts to lower frequencies as the distance increases, but the behaviour is more complicated.

3.2 ANALYSIS OF RESPONSE SPECTRA

The response spectra offer another means of addressing the relative behaviour of underground versus surface stations. They may offer some advantages in comparison to Fourier spectra, in that response spectra have a smoother behaviour with frequency. Response spectra must be less influenced by random noise, because they reflect the peak response of an oscillator to the signal, rather than being a cumulative measure. Response spectra (5% damped pseudo-acceleration) are used to examine this issue.

In this analysis, as in the case of the Fourier spectrum, the relative behaviour of each station is examined through the ratio of the response spectrum at each surface station to that at every underground station which recorded the same event. In Figure 51, ratios for the same typical local event of MN2.6 on May 11, 2008 calculated for S wave (Figures 51a and 51b) and for the whole seismogram (Figures 51c and 51d) are displayed. As for Fourier spectra (Figures 34 and 35), the resulting ratios are similar in both cases for stations with an acceptable level of noise, while in the case of noisy station LSNO, the inclusion of P-waves distorts the spectral ratios. Figure 52 and Figure 53 present ratios of the response spectra at lower frequencies: 1) 0.03-3 Hz estimated from records of the teleseismic Mw7.9 earthquake occurred on May 12, 2008 in Sichuan, China (Figure 52) and 2) 0.2-3 Hz from the regional event Mw5.4 on April 8, 2008 in Southern Illinois (Figure 53). As in the case of Fourier spectral ratios (Figures 36 to 40a), values at $f > 1$ Hz are not reliable due to strong attenuation and scattering of high-frequency body waves from distant events.

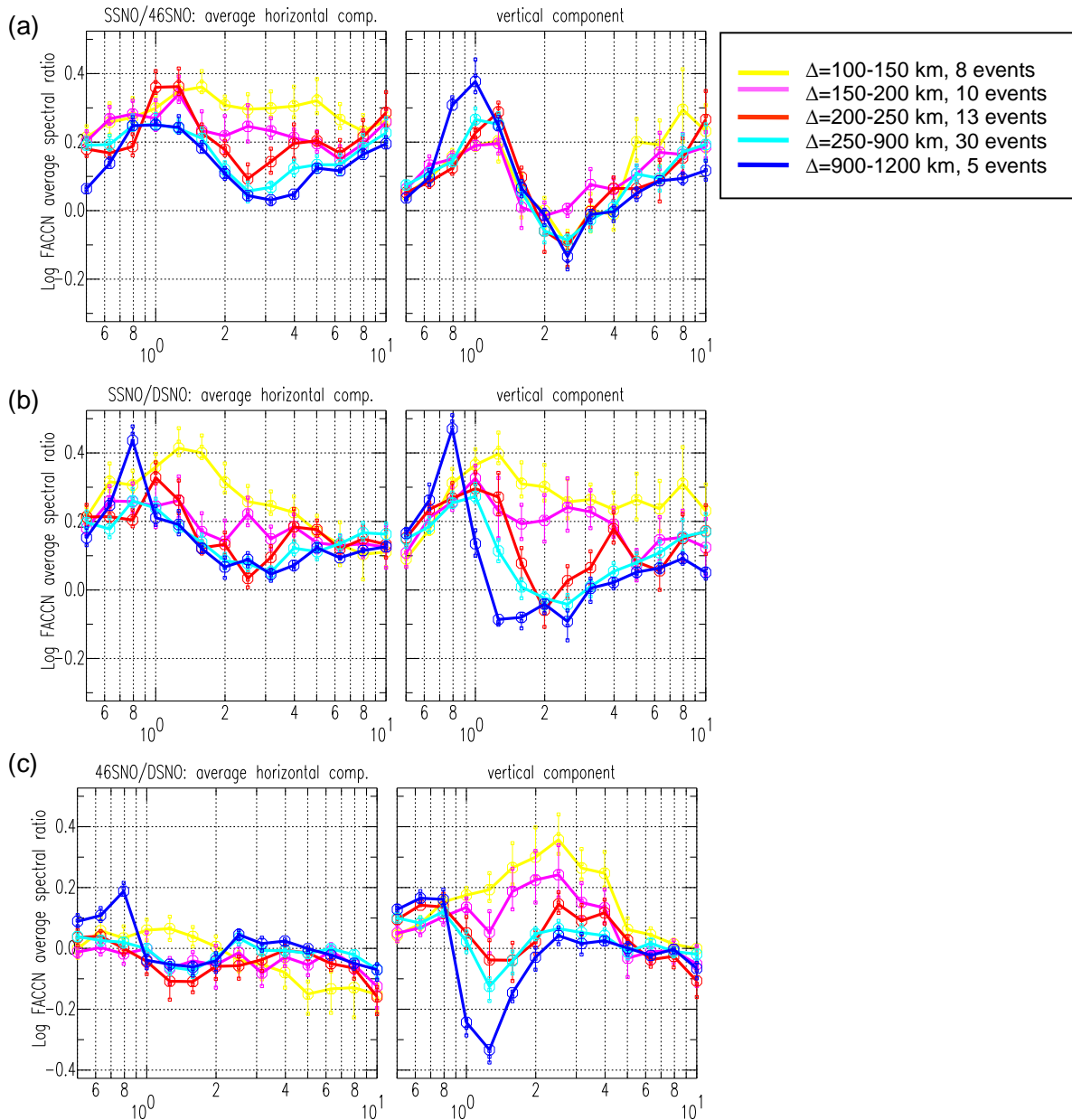


Figure 50: Mean log spectral ratios based on the data from five groups of regional events with increasing epicentre distances. Ratios shown are (a) of the surface stations SSNO to underground stations 46SNO, (b) of the surface stations SSNO to underground stations DSNO, and (c) underground stations 46SNO and DSNO. Error bars correspond to the standard deviation of these ratios.

Figure 54 shows average response spectral ratios of the surface station SSNO to the underground station 46SNO; the behaviour is very similar to that shown in Figure 39 for Fourier spectra, although the peak of the maximum at 2 Hz is slightly reduced (to 0.2 log units, or a

factor of 1.6). Thus, for this pair of stations, vertical and horizontal amplitudes of the response spectra on the surface are greater than that underground on average by a factor of 1.6, at frequencies in the vicinity of 2 Hz, while at 7-30 Hz amplitudes are almost the same for horizontal components and are less by a factor of approximately 1.6 for the vertical component. Site effects begin to be visible from 0.1 Hz for the horizontal component and 0.5 Hz for the vertical component.

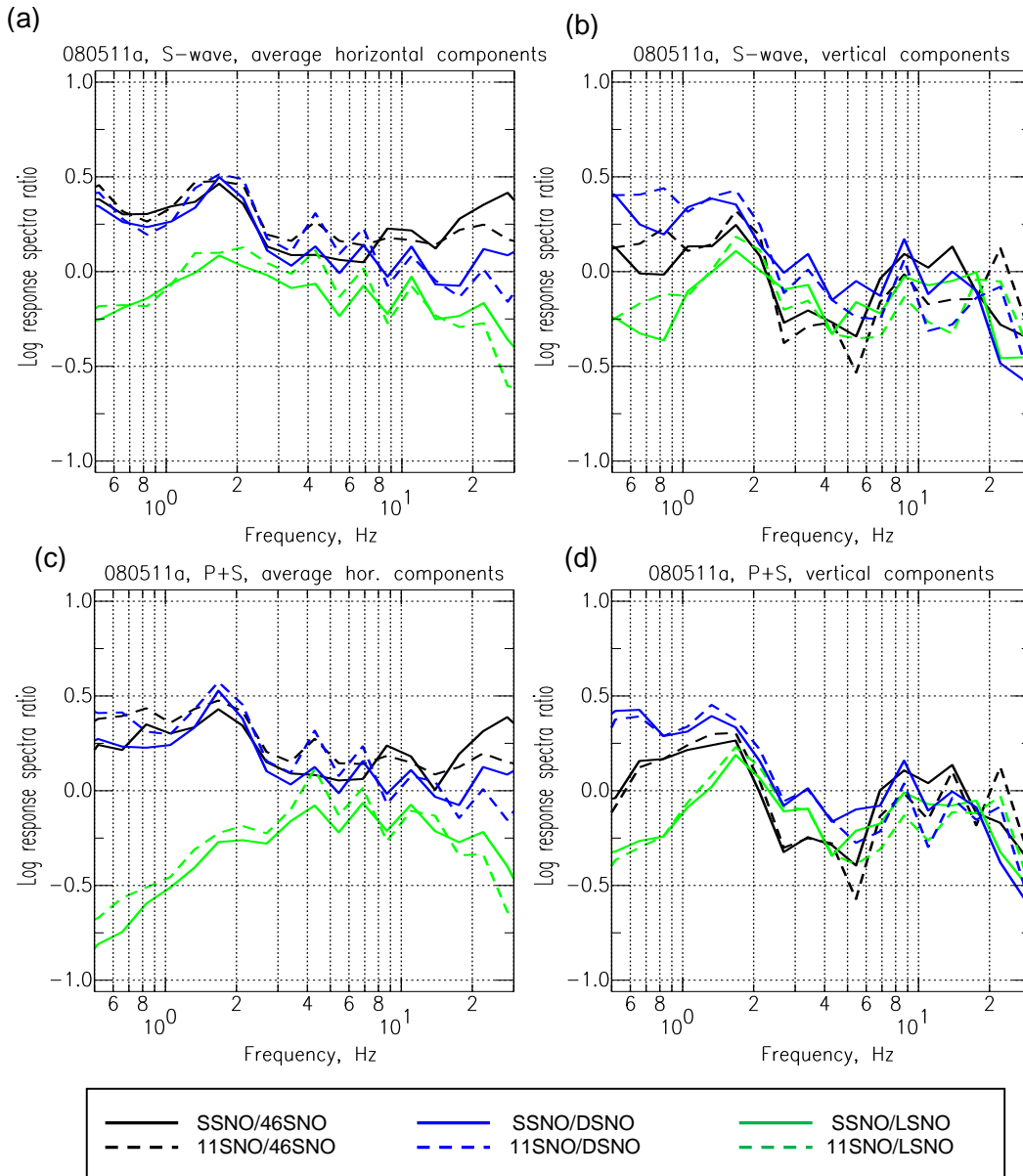


Figure 51: Log ratios of surface stations to underground stations for the event MN2.6 on 11 May 2008 (Figures 22 to 24 and Figures 34 to 35) calculated for response spectra of S-wave and P+S waves. (a) Average horizontal component, S-wave. (b) Vertical component, S-wave. (c) Average horizontal component, P+S-wave. (d) Vertical component, P+S-wave.

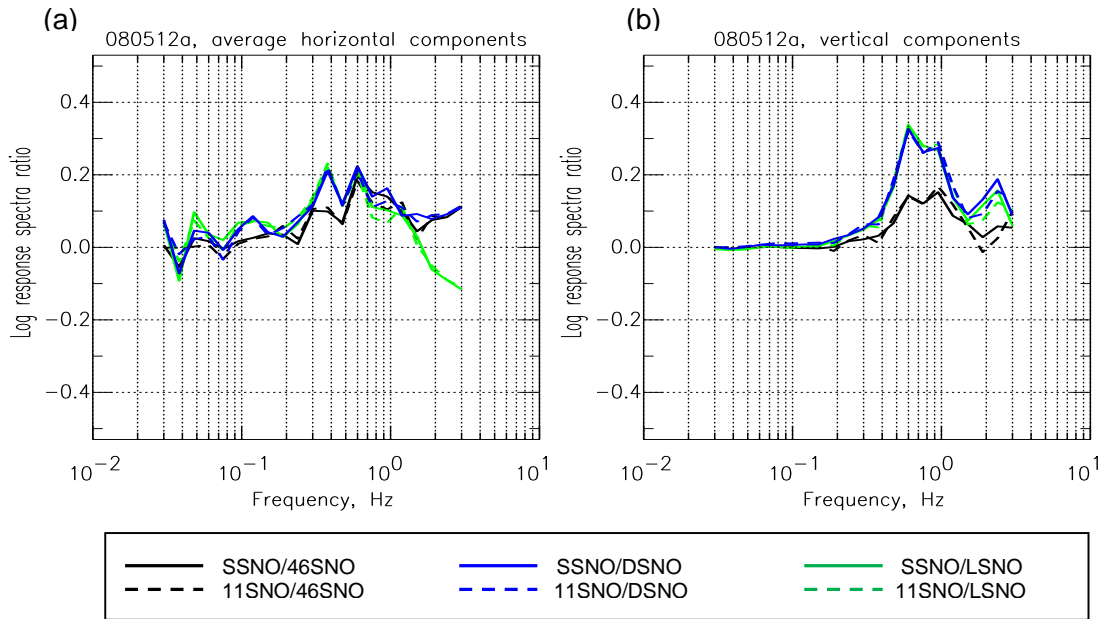


Figure 52: Log ratios of surface stations to underground stations for the teleseismic event Mw7.9, 12 May 2008, Sichuan, China (Figures 25 to 27 and Figure 36) calculated for response spectra of the body waves group (1000 s). (a) Average horizontal component. (b) Vertical component.

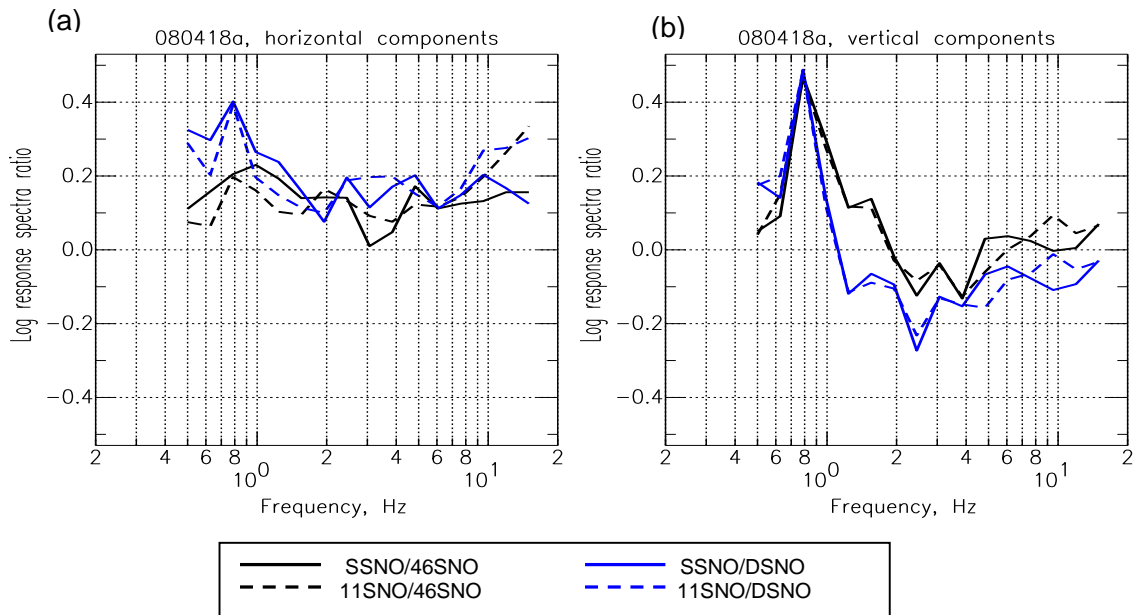


Figure 53: Log ratios of surface stations to underground stations for the regional event Mw5.4, 18 April 2008, Southern Illinois (Figures 28, 30, 32 and 37) calculated for response spectra of acceleration of the 180 s record including S and Lg waves. (a) Average horizontal component. (b) Vertical component.

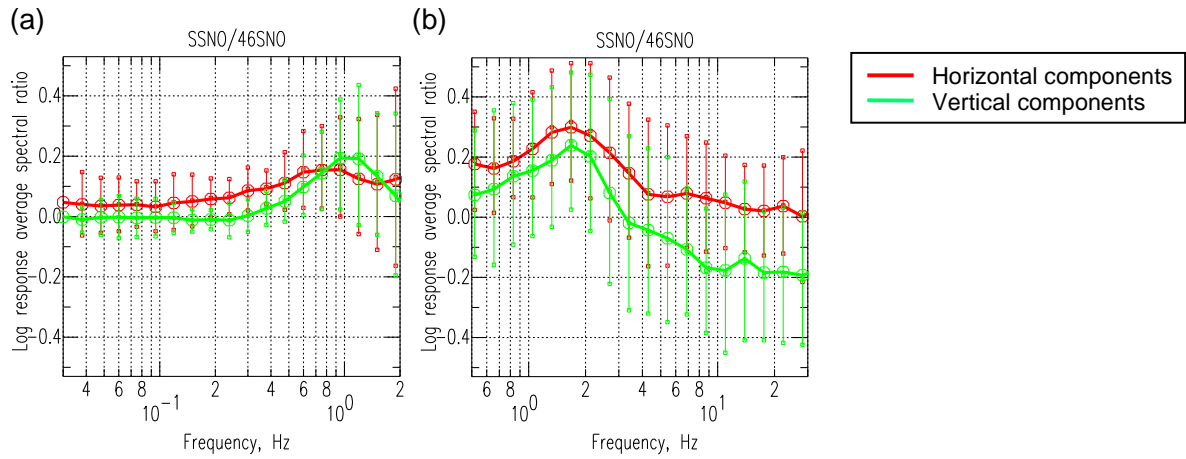


Figure 54: Average ratios of response spectra of the surface station SSNO to underground station 46SNO. Error bars correspond to the standard deviations of these ratios. (a) From the database of 73 teleseismic earthquakes. (b) From the database of 97 close local mining events ($\Delta=8-40$ km).

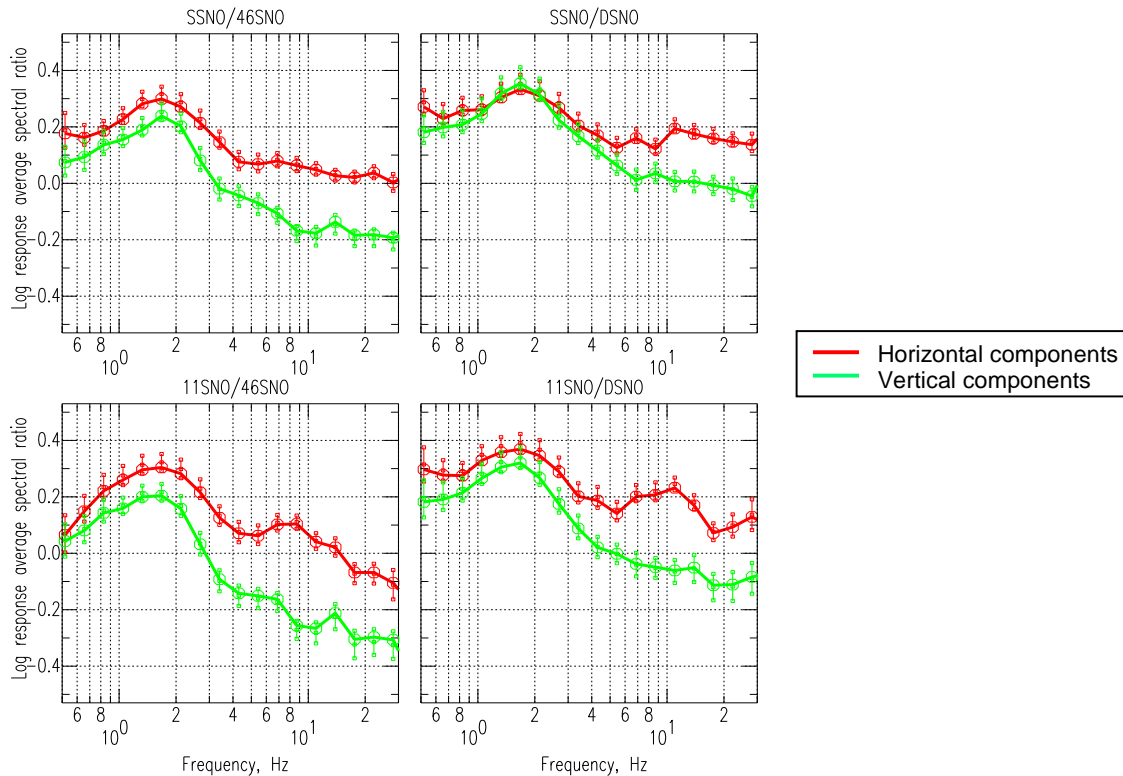


Figure 55: Average ratios of response spectra of the surface stations SSNO (upper two plots) and 11SNO (lower two plots) to underground stations 46SNO (on the left) and DSNO (on the right) for horizontal (red) and vertical (green) components of S-waves, from database of 97 close local mining events ($\Delta=8-40$ km). Error bars correspond to the standard errors of these ratios.

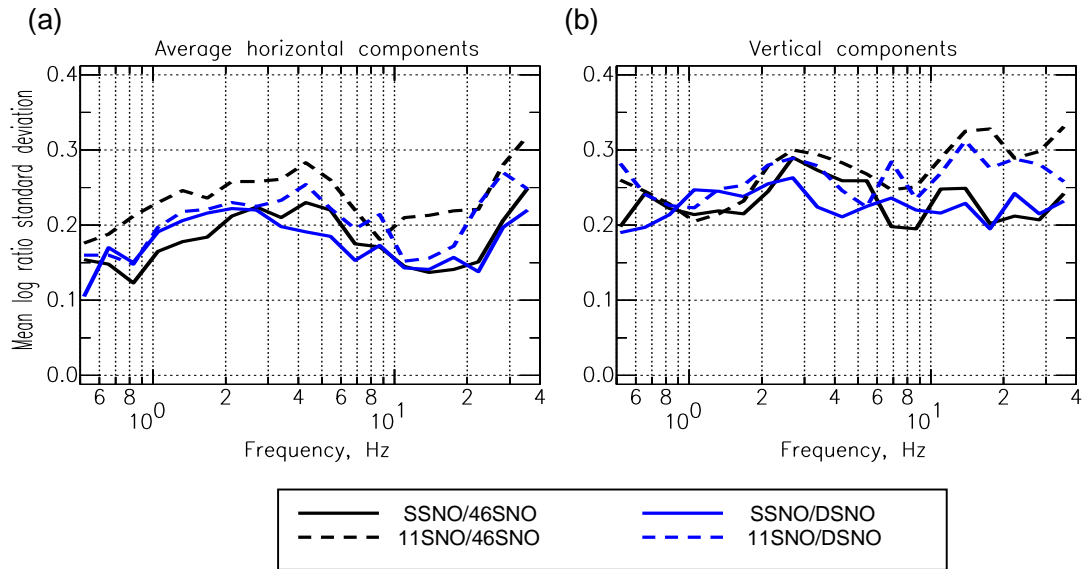


Figure 56: Distribution of standard deviation over frequency for average ratios of response spectra shown in Figure 55. (a) Horizontal components. (b) Vertical components.

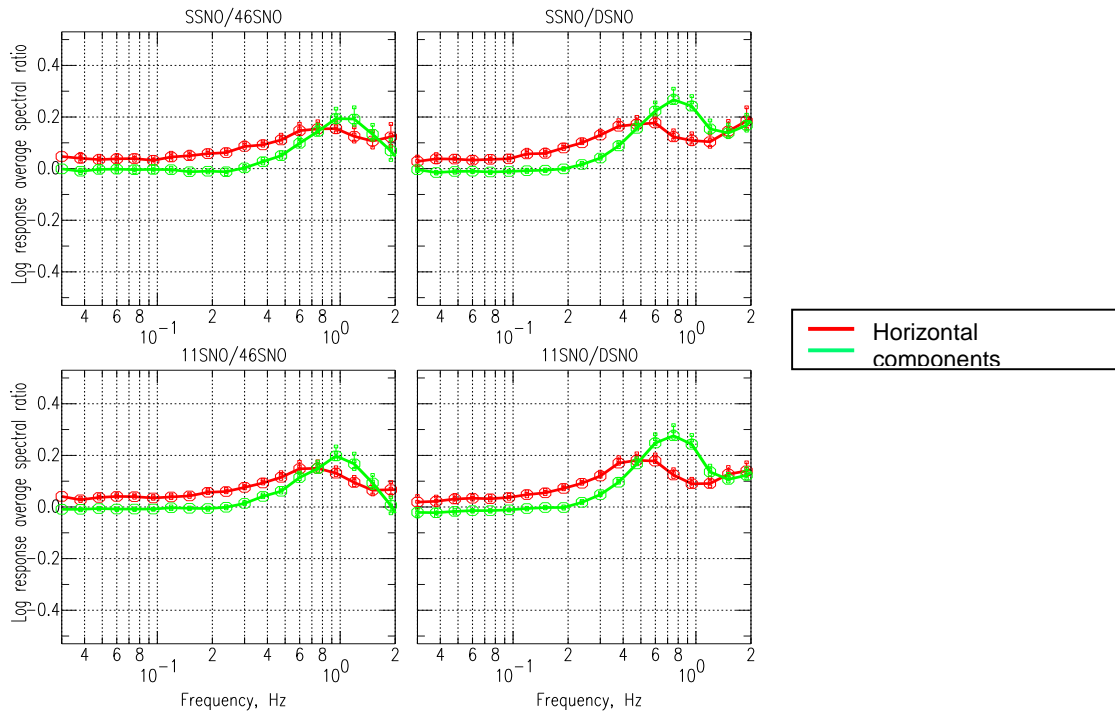


Figure 57: Average ratios of response spectra of the surface stations SSNO (upper two plots) and 11SNO (lower two plots) to underground stations 46SNO (on the left) and DSNO (on the right) for horizontal (red) and vertical (green) components of S-waves, from database of 73 teleseismic earthquakes ($\Delta > 3500$ km). Error bars correspond to the standard errors of these ratios.

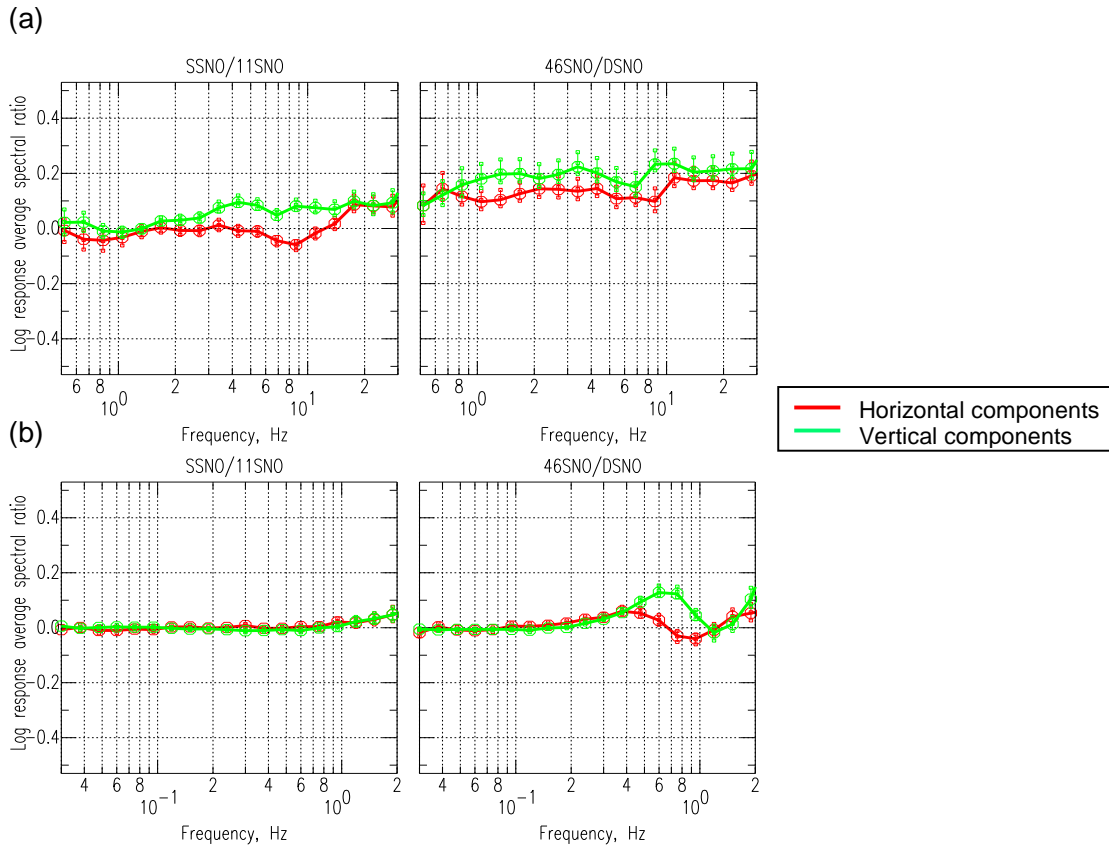


Figure 58: Average ratios of response spectra of the surface stations SSNO and 11SNO (on the left) and underground stations 46SNO and DSNO (on the right), from (a) the database of 97 nearby mining events ($\Delta=8-40$ km), and (b) 73 teleseismic earthquakes ($\Delta>3500$ km). Error bars correspond to the standard errors of these ratios.

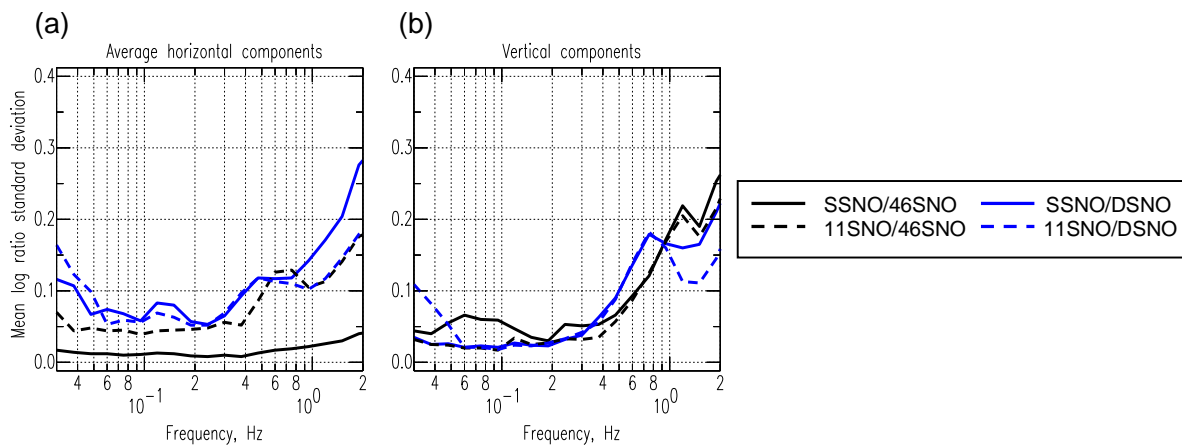


Figure 59: Distribution of standard deviation over frequency for average ratios of response spectra shown in Figure 57. (a) Horizontal components. (b) Vertical components.

Figures 59 through 62 show average response spectrum ratios (surface-to-underground) and the distribution of standard deviations for the database of 73 nearby events ($\Delta=840$ km) and 73 teleseismic earthquakes ($\Delta>3500$ km).

Figure 59 provides ratios for surface and underground stations relative to each other for the two types of events (local and distant). The patterns observed are very similar to those seen for Fourier spectra. As in the case of Fourier spectra analysis of local events, average ratios of response spectra calculated for S wave and the whole record of an event almost fully coincide, and thus are omitted here.

The surface-to-underground response spectra ratios are larger for the horizontal than for the vertical component, in the studied frequency band from 0.5-30 Hz for local mining events (Figure 55). This is consistent with the view that horizontal motions are more amplified on the surface than vertical components due to the velocity gradient effect (Siddiqi and Atkinson, 2002).

Overall, the response spectra data (for local and teleseismic events) indicate that the underground station 46SNO shows a relative de-amplification of the horizontal component relative to the surface at frequencies $f<1.3$ Hz, while the deeper station DSNO reveals such de-amplification of horizontal component at all frequencies from 0.02 Hz to 30 Hz. For the vertical component and for the mining events, de-amplification relative to the surface sites at $0.5<f<2.5$ Hz at the underground station 46SNO, and at $0.5<f<5$ Hz at the station DSNO, is observed. Higher frequencies are characterized by amplification of the vertical component underground, which is noticeable for the 46SNO station (factor of 1.6-2.0) and minor (no more than factor of 1.2) at the deeper station DSNO for local mining events.

It should be kept in mind that all of these amplifications are just relative, and that the variability from one event to another, as reflected by the standard deviation, is large (more than factor of 2). On the other hand, the ratios of surficial to underground motions are based on 97 local events and 73 teleseismic events, and thus the standard errors of the mean are low, about 0.001-0.06 log units. This means that average trends for these databases are determined with confidence, though the factors may vary from one event to another.

3.3 SUMMARY OF GROUND MOTIONS UNDERGROUND COMPARED TO THOSE ON THE SURFACE

The key observations from the comparisons of ground motions recorded on the surface to those underground in the frequency range 0.05-30 Hz can be summarized as follows (Figure 60):

1. Signals from the shallow local events near Sudbury show strong apparent amplification of ground motion observed on the surface relative to those at underground sites. The amplification peaks near 2 Hz, where it is on average a factor of three to eight; and
2. The amplification peak gets narrow, decreases in amplitude, and shifts towards lower frequencies (0.8-1 Hz) for regional and teleseismic events.
- 3.

For explanation of this behavior, average spectral ratios are compared with that of separate events and their band-pass filtered time series. As noted in Section 3.2.1, at teleseismic distances >3500 km, spectral ratios estimated from P and S waves are similar. Moreover, these ratios are close to unity. This suggests that, for very distant events, the higher

amplitudes are not related to body-wave reverberations in the subsurface layers, nor to any specific type of waves, such as surface waves (period > 3 s for teleseismic distances). Rather, it is likely that the observed differences in amplitudes for teleseismic events are related to depth-dependent differences in the medium properties for the pairs of stations examined.

On the other hand, signals from the most distant regional event, namely, the well-recorded Illinois earthquake, demonstrate that the P-wave package (Figure 61a) is amplified at the surface sites in a manner similar to that of S and Lg waves (Figure 61b), but not identically. This amplification is particularly significant in the 0.5-1.5 Hz frequency band. The amplification is most pronounced for the deepest station DSNO for S+Lg waves, while for P waves it is the same for both underground levels (Figure 37b). The behaviour of the 0.8 Hz peak may be due to the influence of the Lg phase, which is the strongest continental phase at regional distances. Note that one wavelength for a 0.8 Hz wave corresponds to a penetration depth of about 4 km. The fact that this peak is seen for P waves and teleseismic waves, but not for the Lg phase, suggests the importance of surface wave phenomena. The Lg phase is a specific surface wave that includes higher-mode Rayleigh waves and high-frequency Love-wave overtone energy (Lay and Wallace, 1995). It produces large-amplitude arrivals on all three components of motion (vertical, radial, and transverse) out to 1000 km for continental settings.

By contrast to distant events, the peak amplifications observed on surface stations for the local mining events are of greater amplitude, and cover a higher-frequency and wider spectral band, between 1 and 3 Hz (Figure 60). This peak is explained by the existence of short-period fundamental mode local surface waves for close events ($T=0.4-2$ s), which are strong due to the shallow depth of mining related events (0-3 km). This interpretation is supported by Figure 62, which shows filtered time series for the vertical component in 3 frequency bands (0.5-3 Hz, 3-6 Hz and 6-20 Hz) for a typical local mining event (11 May 2008, MN2.6, at 22.8 km, same event as shown in Figures 22 to 24, Figures 34 to 35, and Figure 51). The filtered time series reveal that specific waves are responsible for the 2 Hz peak. Specifically, the 2 Hz peak can be attributed to wavelets that are observed only in the 0.5-3 Hz frequency band, with group velocity about 2.7 km/s (vertical component) and about 3 km/s (horizontal component) and dominant frequency 1-2 Hz; these wavelets arrive later than the direct shear wave Sg. The time delay is about 1 s and 0.5 s for SV and SH components, respectively. These are probably the short-period fundamental-mode Rayleigh wave (Rg, Figure 62a) and Love wave (Lg, Figure 62b), as their amplitudes diminish markedly with depth, suggesting they are surface waves. Note that the Lg wave here (unlike at regional distances) represents predominantly transverse motion through the upper crust. Note also that the amplitudes of ground motion in the Sg window are similar for the surface and underground stations at high frequencies. Interestingly, at frequencies below about 6 Hz, the shear wave vertical amplitudes (in the window before Rg arrival) are actually higher underground than on the surface. Because the Rg amplitude is twice as great as that of Sg (SV) wave at $f = 0.5-3$ Hz, and its decrease in amplitude with depth is very strong (a factor of ~ 6), the net result is amplification of vertical component at 0.5-3 Hz on the surface, and de-amplification at 3-6 Hz (as seen in Figure 34b).

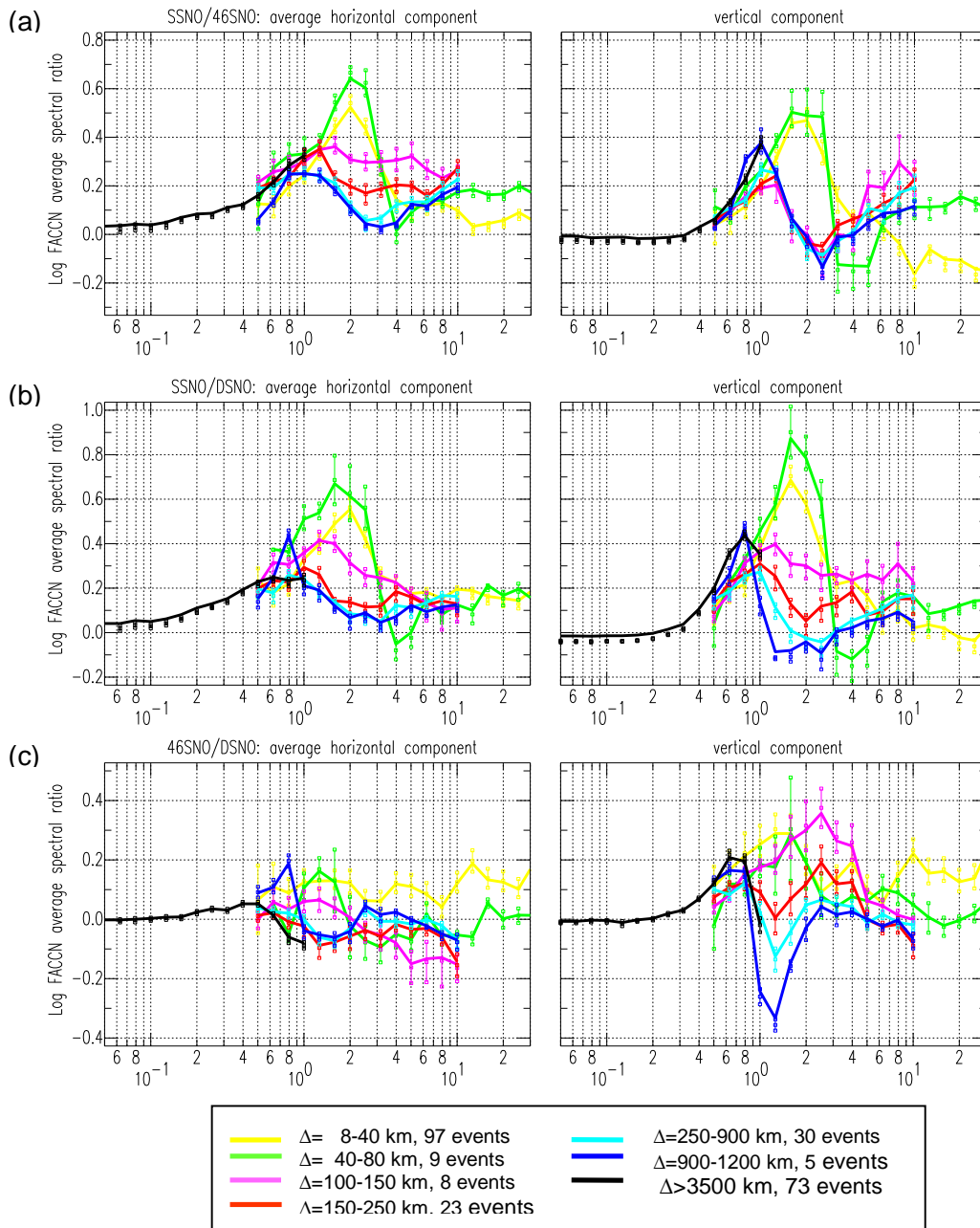


Figure 60: Mean log spectral ratios averaged over 7 groups of events sorted by distance, for horizontal (left) and vertical (right) components. Error bars correspond to the standard errors of these ratios. In the legend, the range of epicenter distances is given for every curve with the number of events. (a) Ratios for SSNO station on the ground surface relative to the 46SNO station underground (1.4 km). (b) Ratios for SSNO station on the surface relative to the DSNO station underground (2.1 km). (c) Ratios between underground stations 46SNO to DSNO.

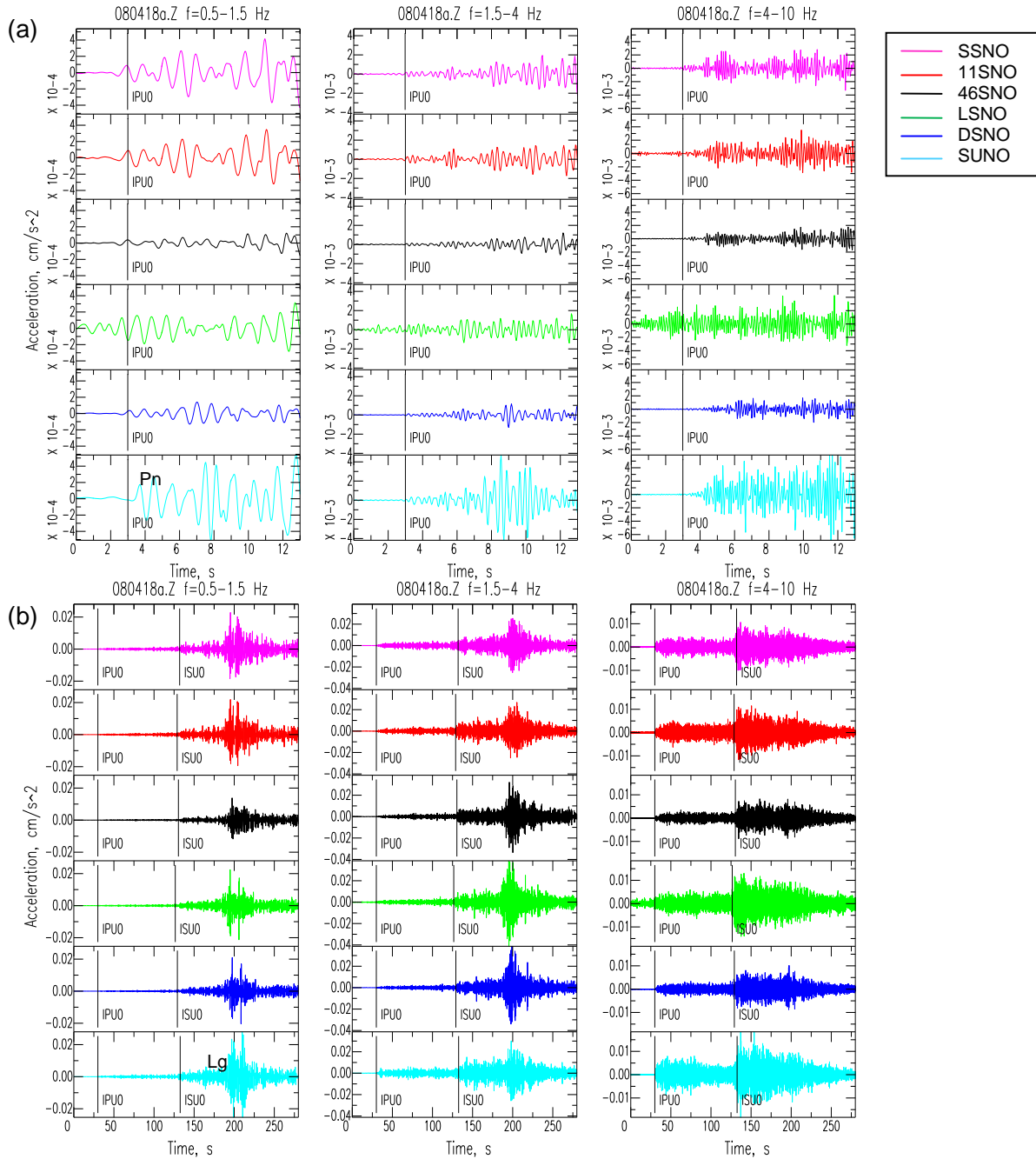


Figure 61: Frequency-amplitude variability depending on the site location: vertical Z component of ground motion acceleration for the regional event Mw5.4, 18 April 2008, Southern Illinois (Figures 28, 30, 32, 37 and 53) at SNO and SUNO stations in three frequency bands, 0.5-1.5 Hz (left column), 1.5-4 Hz (central column) and 4-10 Hz (right column). (a) First 10 s of the P-wave. (b) The whole record including Pn, Sn and Lg wave-groups. Horizontal components (R and T) show similar amplifications.

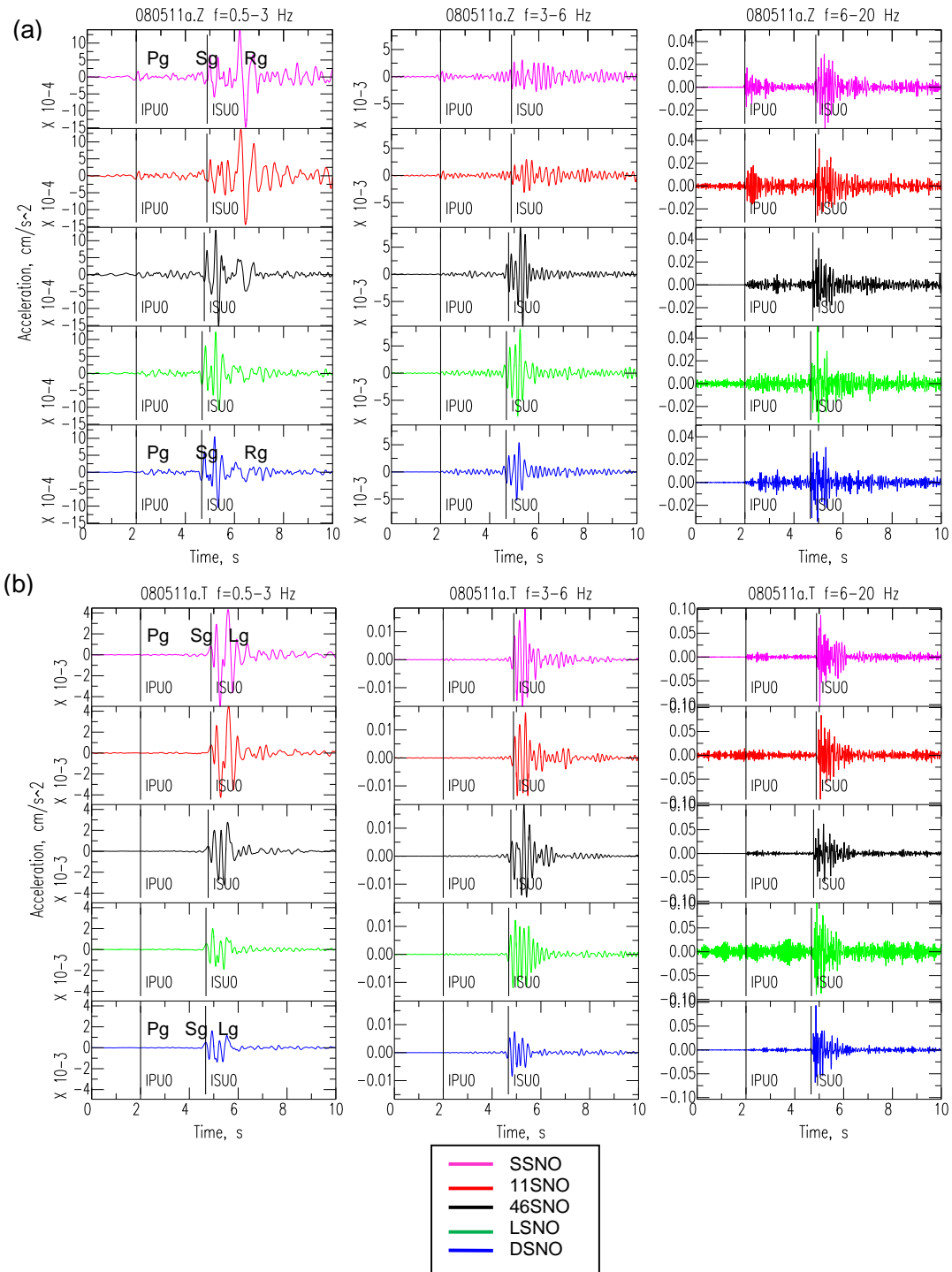


Figure 62: Frequency-amplitude variability depending on the site location: (a) vertical and (b) transverse components of ground motion acceleration for the typical mining event MN2.6 on 11 May 2008 at 5 SNO stations in three frequency bands, 0.5-3 Hz (left column), 3-6 Hz (central column) and 6-20 Hz (right column). Epicentre distance for DSNO station is 22.8 km as estimated by GSC (Table 4).

This phenomenon is examined for a more distant mining event, the MN2.1 event of May 8, 2008, 35.3 km from SNO. As seen on Figure 63, the apparent amplification attributable to the Rg wave is even stronger in the vertical direction for this event, probably because the greater distance has allowed the Rayleigh wave to develop more fully, and separate from the shear wave more distinctly. The amplification on the surface relative to underground is very large, on both the vertical and horizontal components, suggesting that the Rg wave is a very significant component of the motion on the surface for frequencies less than 3 Hz.

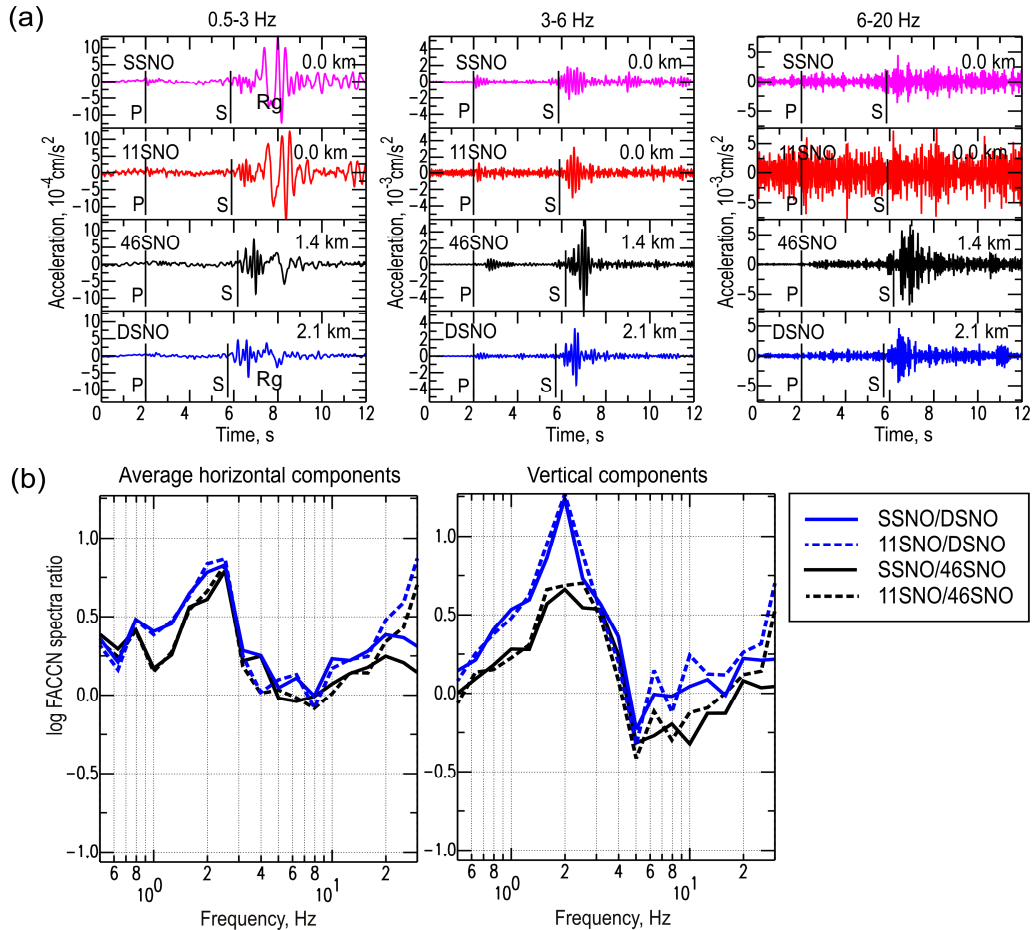


Figure 63: The MN2.1, 8 May 2008 mining event at 35.3 km from the SNO Lab. (a) Frequency-amplitude variability depending on the station depth; vertical components of ground motion acceleration in three frequency bands, 0.2-4 Hz (left column), 4-9 Hz (central column) and 9-20 Hz (right column). The stations names and their depths are given above the traces. (b) Log ratios of surface stations to underground stations calculated for Fourier spectra of average horizontal component (left) and vertical component (right) of S-waves.

To provide further insight into the observed waves, their spectrograms and particle motions are evaluated. Figure 64 presents the vertical and transverse components of acceleration from this event, and their spectrograms, at the ground surface (SSNO) and at 2.1 km depth underground (DSNO) in the frequency band 0.2-10 Hz. As this was a shallow event (within the upper 2 km),

both Rayleigh and Love waves were excited. These surface waves are clearly separated in time and/or in frequency from the Sg (SV and SH) body waves on the surface site, as shown in the spectrograms; the group velocities can be estimated as 2.9 km/s for the Rayleigh Rg wave, and 3.1 km/s for the Love wave, for the first arrival at frequency 1 Hz. Note that the Lg wave here represents predominantly transverse motion through the upper crust. Underground the Rg and Lg are strongly decreased in amplitude and truncated in frequency composition. The dispersive character of the surface waves is also evident, as these constituents are delayed in time relative to Sg.

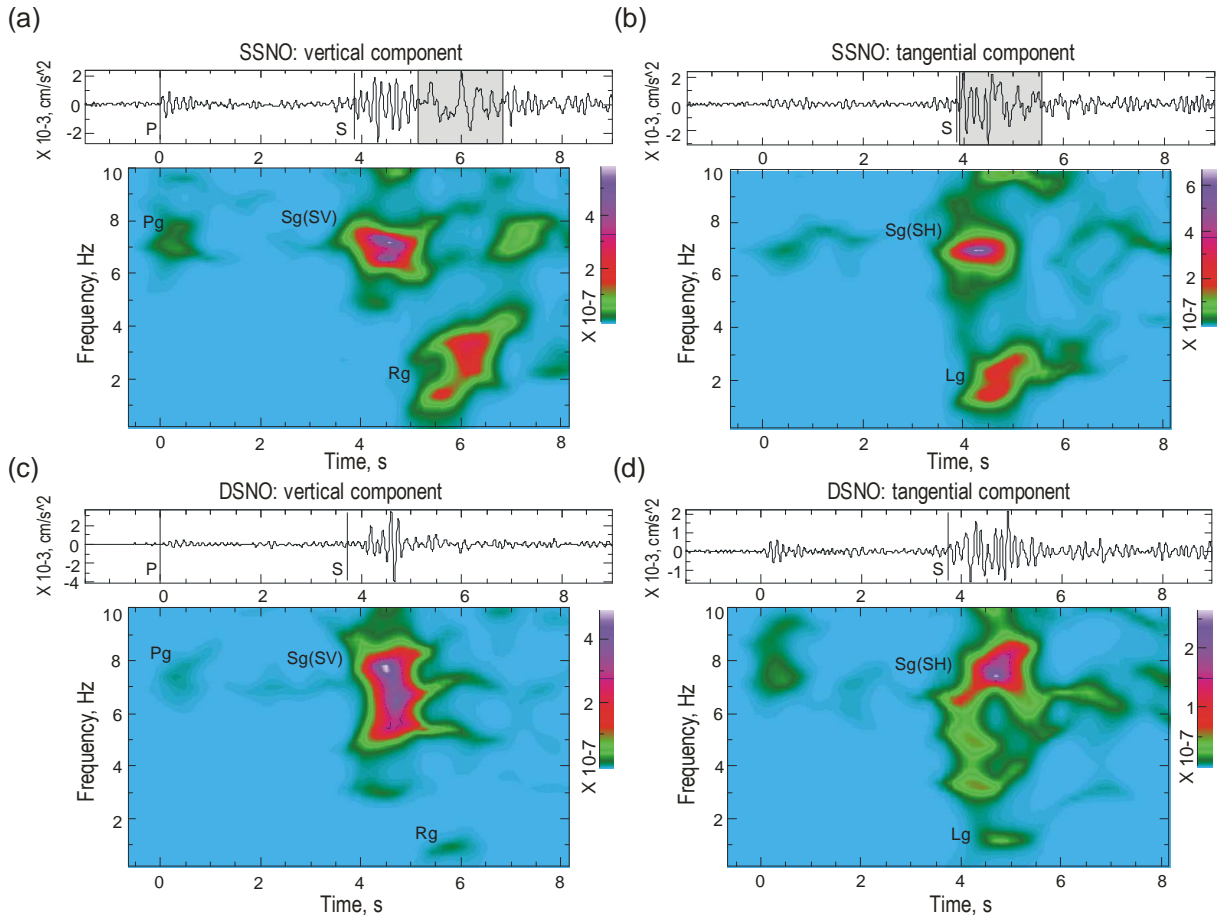


Figure 64: Records of the local Sudbury mining event MN2.1, 8 May 2008 (35.3 km distant from DSNO as determined from the GSC epicenter location) in the frequency band 0.2-10 Hz and their spectrograms. (a) vertical and (b) tangential components of acceleration at ground surface (SSNO station); (c) vertical and (d) tangential components of acceleration at 2.1 km depth (DSNO station). The time intervals on seismograms for surface stations, as selected by gray shading, represent the group velocity arrival time windows for (a) Rg (2.5 to 2.9 km/s) and (b) Lg (2.8 to 3.2 km/s).

On Figure 65, particle motions for the Rayleigh wavelet recorded from this event on the surface and underground, in the radial-vertical RZ plane at frequencies 0.2-4 Hz, are plotted. Note the clear retrograde movement (against the direction of propagation) in an elliptical pattern with a vertical long axis, as expected for Rayleigh waves (Russell, 2001). The ground motion

underground is simpler than that on the surface, showing just a 1-Hz harmonic; the 2-4 Hz constituents that provide additional particle circulation on the surface disappear underground. Although the dominant feature on the surface, intense local surface waves, Rg and Lg, are strongly attenuated underground. One wavelength for a 2 Hz wave corresponds to a penetration depth of the order of the depth of the underground stations ($3 \text{ km/s} / 2\text{Hz} = 1.5 \text{ km}$). Some Rg and Lg waves at the deepest level of 2.1 km (stations DSNO and LSNO, Fig. 62-65) are observed, but the amplitudes of these waves are weaker than at the intermediate depth of 1.4 km (46SNO), and are much weaker than on the surface.

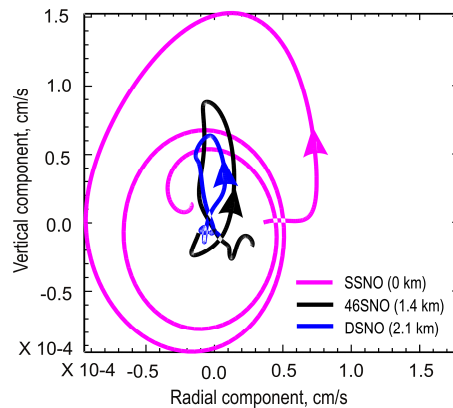


Figure 65: Particle motion (velocity in radial-vertical plane) in the Rayleigh wave during 1.5 s (starting 5.1 s after P-wave arrival, see Figure 64) for the mining event MN2.1, 8 May 2008, in the 0.2-4.0 Hz frequency band, at ground surface (gray solid curve), at a depth of 1.6 km (thin black dotted curve), and at a depth of 2.1 km (thick black solid curve). Direction of movement indicated by arrows corresponds to retrograde particle motion.

3.4 OVERVIEW OF HIGH-FREQUENCY RG STUDIES

Many other researchers have observed this short-period (<3s) fundamental mode Rayleigh wave (Rg) at local and regional distances and used it in their studies, particularly as a depth discriminant for earthquakes and explosions (Bath, 1975; Kafka, 1990; Saikia, 1992; Kocaoglu and Long, 1993; Goforth and Bonner, 1995; McLaughlin et al., 2004; Malovichko, 2005; Goforth et al., 2006; Ma et al., 2008; Ma and Eaton, 2009).

The Rg wave is the result of complex interference of P and S waves in the vicinity of the source and along the propagation path. Its excitation is very dependent on the focal depth; if the source depth is greater than 4 km, the amplitude of short-period Rg waves becomes weak (Kafka, 1990; Ma et al., 2008). Lay and Wallace (1995) note that in most regions, Rg is rapidly attenuated, and it is rare to identify it beyond a few hundred kilometres. By contrast, Lg (crustal "channel") waves may travel in continental shield regions over larger distances (Bormann, 2002) than Rg waves. Thus, Lg waves will be more important in determining the spectral ratio effects at larger distances, while the effects seen here for the local events may be specific to those expected for shallow crustal earthquakes nearby. Both of these types of events and behaviour are important in terms of their seismic hazard implications.

Rg waves with frequency 1.5-2 Hz are dominant in all records in the local distances database primarily due to the bias of this database towards motions generated by very shallow events,

such as blasts and rockbursts in mines. Nevertheless, it is important to recognize that short-period surface waves are the largest identifiable phases excited by shallow events at local distances, and have spectral amplitudes exceeding those of body-wave arrivals (McLaughlin et al., 2004). Jessie et al. (2002) modelled short-period surface waves from small explosions by the pseudo-spectral method. They also have shown that, for explosions, the largest arrival at stations at local distances for vertical components in the 0.5-4 Hz frequency band is Rg; however, the complexity of the Rg packet varies significantly at each station depending on lateral velocity and attenuation variations and on near-source scattering effects. Furthermore, modelling by Malovichko (2005) and Malovichko and Baranov (2001) have shown that rockfalls accompanying blasts and rockbursts in mines also can increase the amplitude of the resulting Rg phase. Due to its large amplitude, Rg may be a significant contributor to hazard for surface sites for shallow nearby events (though it is not a site effect, it is a significant path effect); this contribution may not be readily captured by existing ground-motion prediction models due to the paucity of data including this effect within ground-motion databases and models. More investigation of the significance of Rg for seismic hazard for shallow nearby earthquakes is warranted. The associated hazard applies to surface sites, but not those underground.

3.5 HIGH-FREQUENCY RG AND LG WAVES OBSERVED IN CANADA BY SURFACE STATIONS AT LOCAL AND REGIONAL DISTANCES

To understand why the amplification peak on the surface relative to that underground (attributed to the Rayleigh wave Rg) shifts in frequency as the distance from the event increases, consider Figure 66. This figure plots vertical and transverse component seismograms recorded by broadband stations of the Canadian seismic network at distances from 22-354 km for the Lively, Ontario mining-induced earthquake of MN4.1, which occurred on November 29, 2006 a few hundred meters under the SNO Lab (Atkinson et al., 2007). The seismograms are filtered in two frequency bands (0.5-1.2 Hz and 1.2-2.2 Hz), defined here as the 1-Hz and 2-Hz bands. In the 1-Hz band, the Rg and Lg waves are clearly visible at all distances (out to 354 km) with maximum amplitude being associated with group velocity 2.8-3.2 km/s for Rg and 3.3-3.6 km/s for Lg; in the 2-Hz band, surface waves arrive a bit later, and are predominant only at the nearest stations. Note that the 2-Hz constituent of the Lg wave decreases but does not disappear at the largest distance presented (354 km), while that of Rg is not observed at 248 km and farther. Note also that the vertical component of Lg is developing as distance increases; thus it becomes visible at 118-146 km, and matches the Rg amplitude at 1 Hz at 180 km distance (Figure 66a). Recall that this component was not observed at a distance of 35 km for the MN2.1, May 8, 2008 mining event (Figure 64).

The rapid loss of higher-frequency constituents of the Rg wave with distance allows the longer-period and shear-wave components of the waves, and their effects, to dominate the spectral ratios at larger distances for the vertical component. For the transverse component, this loss is slower. This may be the reason for differences in spectral ratios for horizontal and vertical components at 1-2 Hz. The shear wave effects include amplification at lower frequencies on the surface relative to underground, resulting from the impedance gradient attributable to decreasing shear-wave velocity as the surface is approached. This is balanced by a high-frequency energy absorption near the surface due to jointing and weathering (kappa effects), so that at higher frequencies ($5 < f < 30$ Hz) the motions underground are similar in amplitude to those on the surface.

It may be deduced from Figure 64 and Figure 66 that the distance range at which this transition takes place is about 150-200 km. Beyond this range, the higher-frequency components of the

Rg wave become negligible, and those of Lg waves become small, though longer-period surface waves (1 Hz) may still be contributing significantly to the spectral ratios.

At longer periods ($T > 3-5$ s), the wavelengths of surface waves exceed the depth of the SNO stations underground, and thus the effect of surface waves on the ratio must be less pronounced. The peak in the ratio of surface to underground amplitudes observed at teleseismic distances may be due to other factors, such as the variation of medium properties with depth. At the lowest frequencies (0.1 Hz), amplitudes on the surface and underground are approximately equal, as would be expected based on their wavelengths.

Presence of 1-2 Hz surface waves at local and close regional distances, and their attenuation with epicentre distance, can readily be seen in spectra as well as in time series. This is shown in Figure 67 for the Lively event. All spectra presented are corrected for instrument and geometrical spreading and roughly corrected to a reference distance of $D=100$ km, by multiplication by $\sqrt{D/100}$. Spectra with strong resonant site effects were excluded; spectra of stations at similar epicentre distances are grouped and averaged, to allow trends to be more clearly seen.

Strong surface waves cause departures from a theoretical 'omega-squared' spectrum in form of a shoulder at 2 Hz for local and nearby stations, which shifts to 1 Hz and less with increasing distance. This shoulder is responsible for the 1-2 Hz peak of spectral ratios for nearby events. The database of underground records of local and regional events is limited by the lack of events at mid-crustal depths, for which surface wave effects may be less important. This points to the need to more carefully study the constituent wave components of the ground-motion signal, on the basis of regional records of ground motions induced by earthquakes of eastern Canada, to better understand the importance of depth on ground motions. For this purpose, the Canadian composite seismicity catalogue and station list for 1990-2008 was analyzed to find events with strong signal ($M > 3.8$) and good station distribution over a range of local to regional distances. In addition to the shallow Lively event, a few events (6) were found from varying depths: shallow events ($h \sim 5$ km), moderate ($h \sim 10$ km) and deep ($h > 15$ km) events. Their spectra and groups of spectra, averaged over similar epicenter distances, allow examination of how the surface wave contribution develops over distance for events with different hypocenter depth. This will allow for characterization of how much of the signal is in the form of surface waves that would be attenuated with depth.

Spectra shown in Figures 68 through 73 are calculated and grouped in the same manner as those for the Lively event (Figure 67). They are presented by increasing hypocenter depth, from 1 km (Figure 68) to 19 km (Figure 73). As in Figure 67, spectra were calculated separately for R, T and Z directions of every event, allowing the opportunity to separate the influence of different types of regional surface waves. The T-component reflects the influence of only Lg waves, while the R and Z components combine effects of Rg waves (at local and close regional distances) and Lg waves (at regional distances).

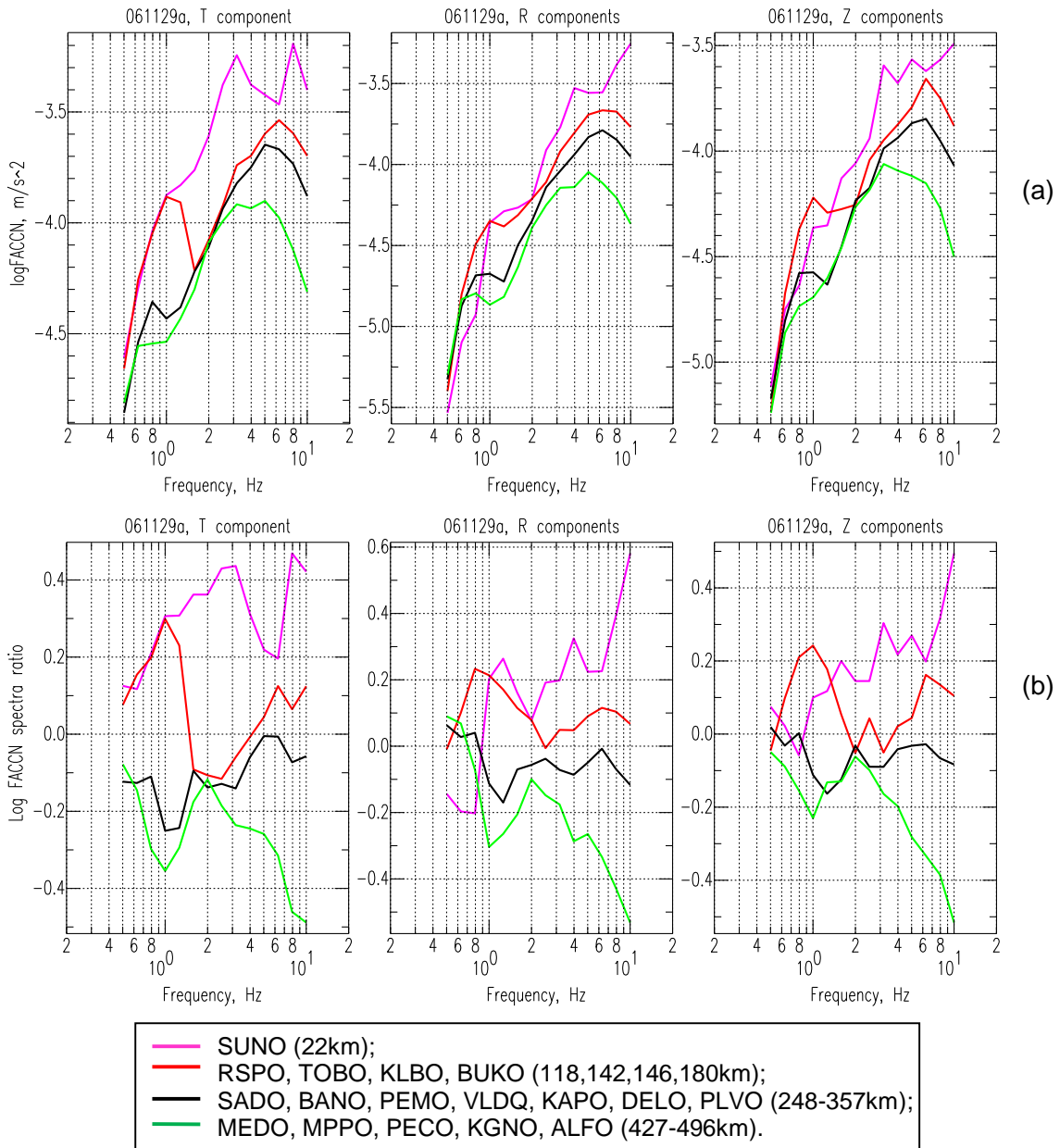


Figure 67: (a) Smoothed Fourier spectra and (b) spectral ratios of horizontal (T and R) and vertical (Z) components of acceleration (S and Rg/Lg waveforms), for the Lively earthquake (Figure 66) recorded by Canadian broadband stations at local and regional distances. Spectra are averaged over stations listed in the legend (their epicenter distances are given in the brackets). Spectra are corrected for instrument and geometrical spreading and reduced to 100 km.

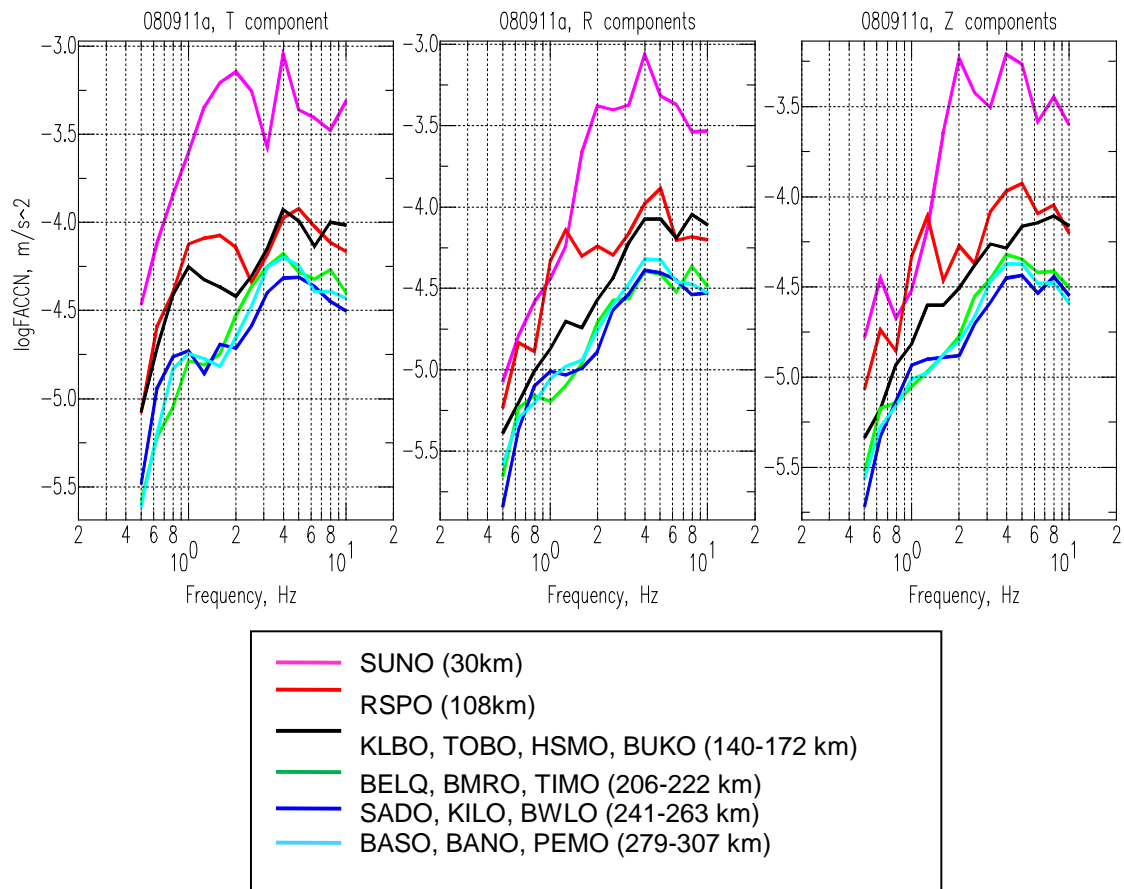


Figure 68: (a) Smoothed Fourier spectra and (b) spectral ratios of horizontal (T and R) and vertical (Z) components of acceleration (S and Rg/Lg waveforms), for the ML=3.8, 11 September 2008 at 11:21AM, h=1 km earthquake recorded by Canadian broadband stations at local and regional distances. Spectra are averaged over stations listed in the legend (their epicenter distances are given in the brackets). Spectra are corrected for instrument and geometrical spreading and reduced to 100 km.

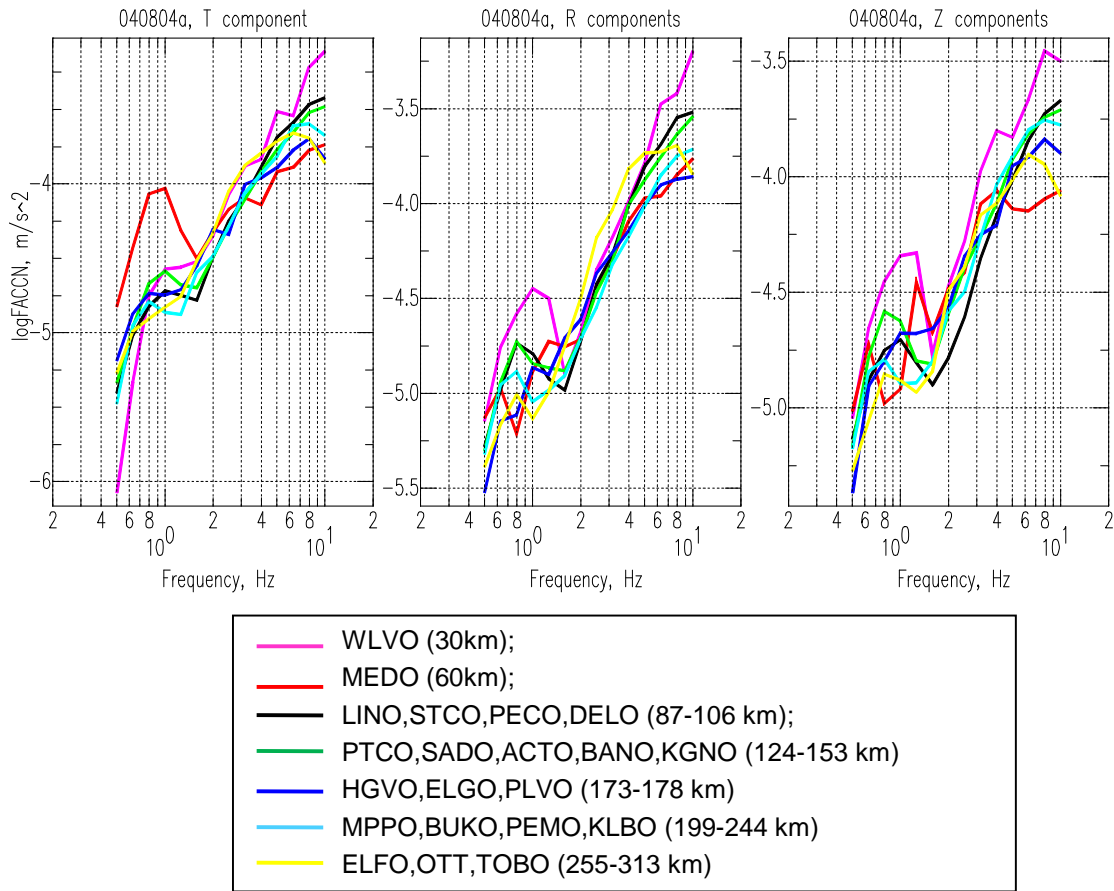


Figure 69: (a) Smoothed Fourier spectra and (b) spectral ratios of horizontal (T and R) and vertical (Z) components of acceleration (S and Rg/Lg waveforms), for the MN=3.8, 4 August 2004 at 11:55PM, $h=3$ km earthquake recorded by Canadian broadband stations at local and regional distances. Spectra are averaged over stations listed in the legend (their epicenter distances are given in the brackets). Spectra are corrected for instrument and geometrical spreading and reduced to 100 km.

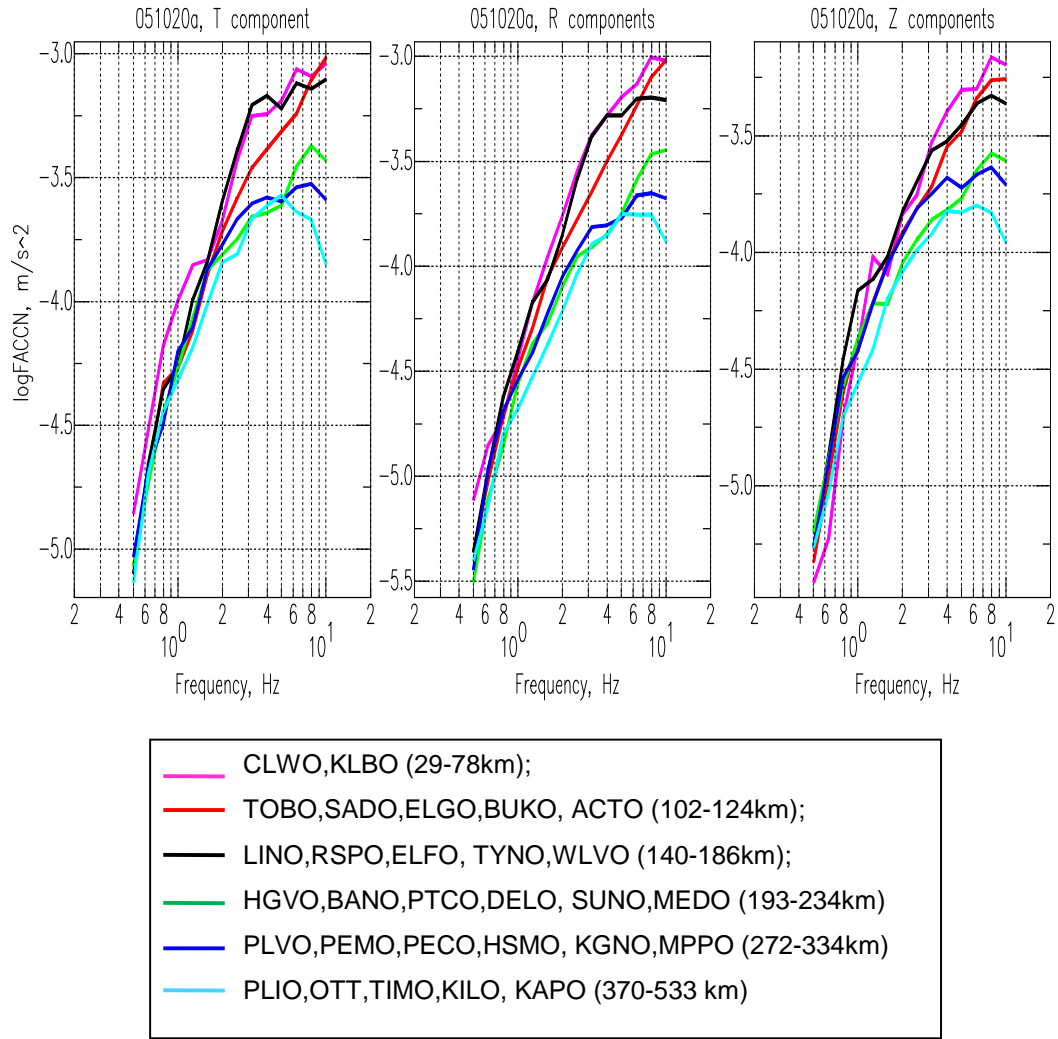


Figure 70: (a) Smoothed Fourier spectra and (b) spectral ratios of horizontal (T and R) and vertical (Z) components of acceleration (S and Rg/Lg waveforms), for the MN=4.3, 20 October 2005 at 9:16PM, h=11 km earthquake recorded by Canadian broadband stations at local and regional distances. Spectra are averaged over stations listed in the legend (their epicenter distances are given in the brackets). Spectra are corrected for instrument and geometrical spreading and reduced to 100 km.

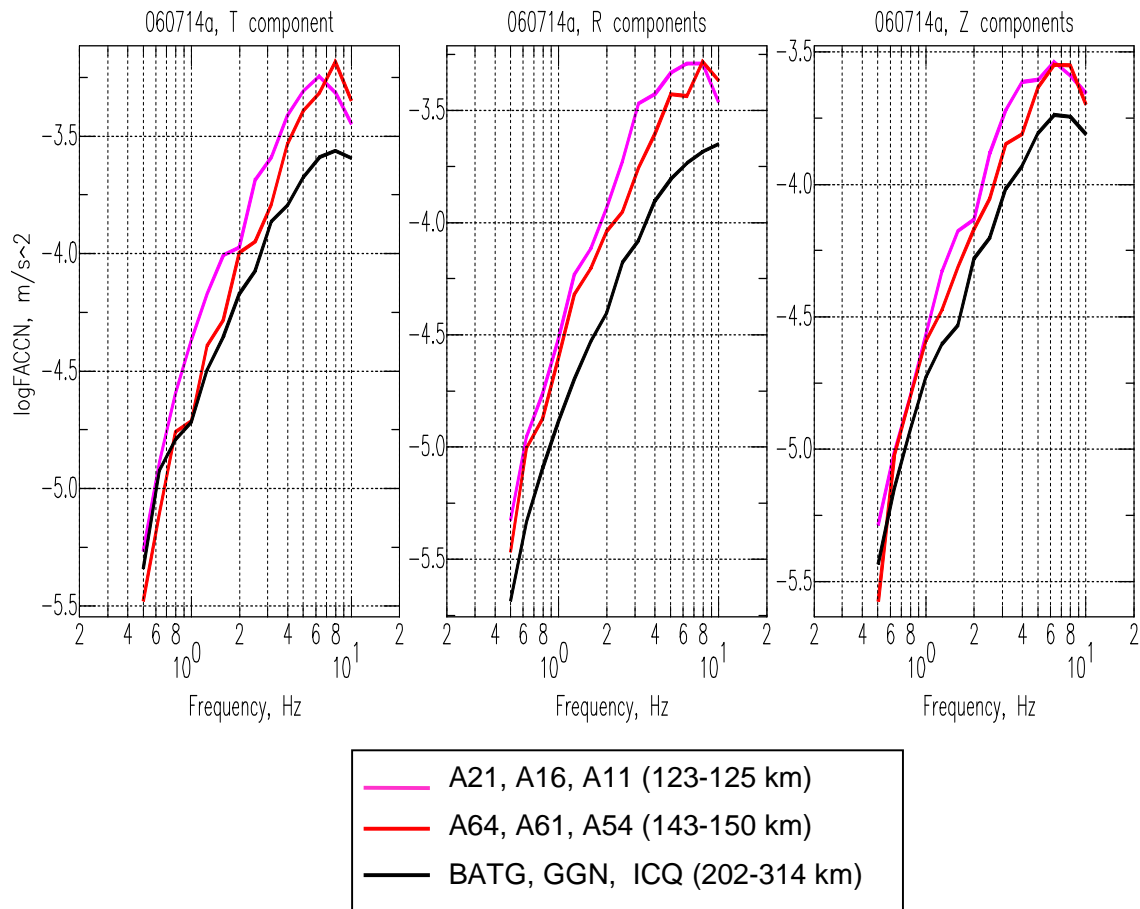


Figure 71: (a) Smoothed Fourier spectra and (b) spectral ratios of horizontal (T and R) and vertical (Z) components of acceleration (S and Rg/Lg waveforms), for the MN=4.0, 14 July 2006 at 9:34AM, h=5 km earthquake recorded by Canadian broadband stations at local and regional distances. Spectra are averaged over stations listed in the legend (their epicenter distances are given in the brackets). Spectra are corrected for instrument and geometrical spreading and reduced to 100 km.

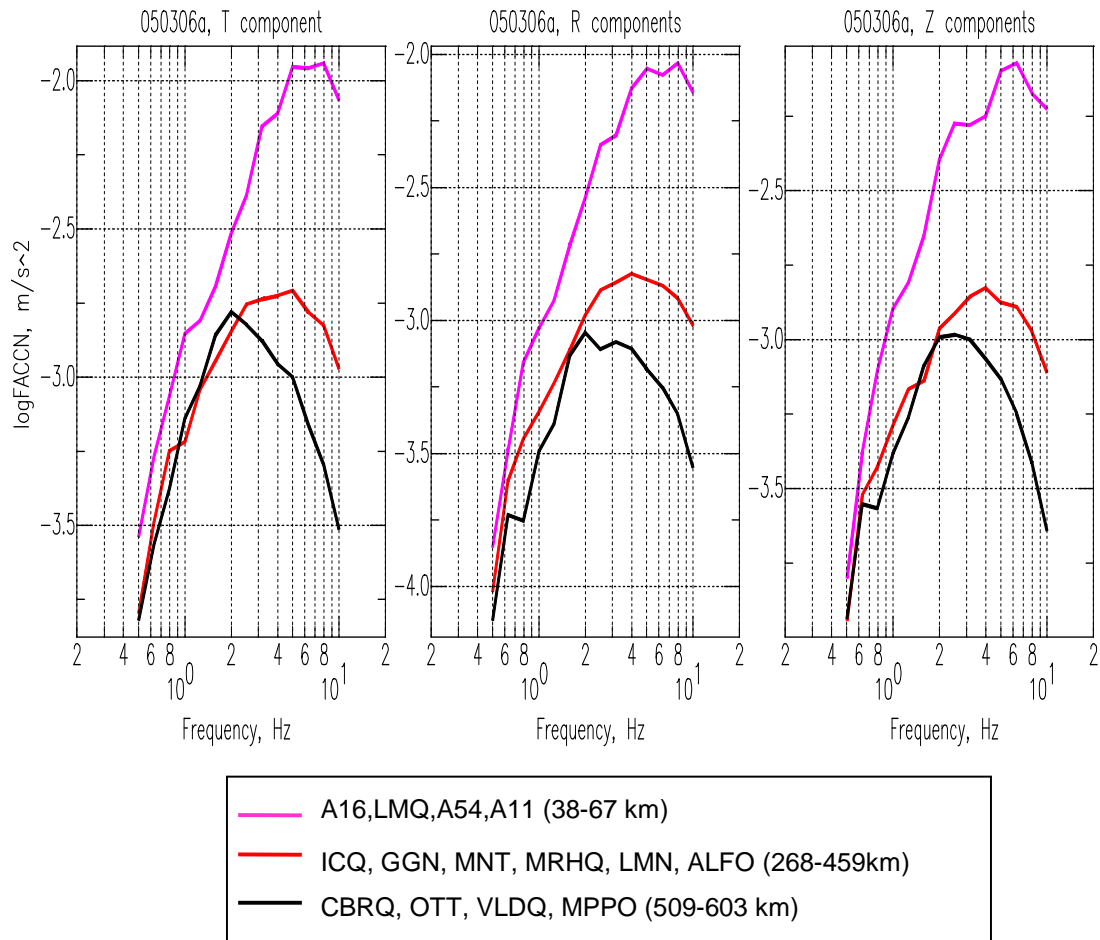


Figure 72: (a) Smoothed Fourier spectra and (b) spectral ratios of horizontal (T and R) and vertical (Z) components of acceleration (S and Rg/Lg waveforms), for the MN=5.4, 6 March 2005 at 6:17AM, h=13.3 km earthquake recorded by Canadian broadband stations at local and regional distances. Spectra are averaged over stations listed in the legend (their epicenter distances are given in the brackets). Spectra are corrected for instrument and geometrical spreading and reduced to 100 km.

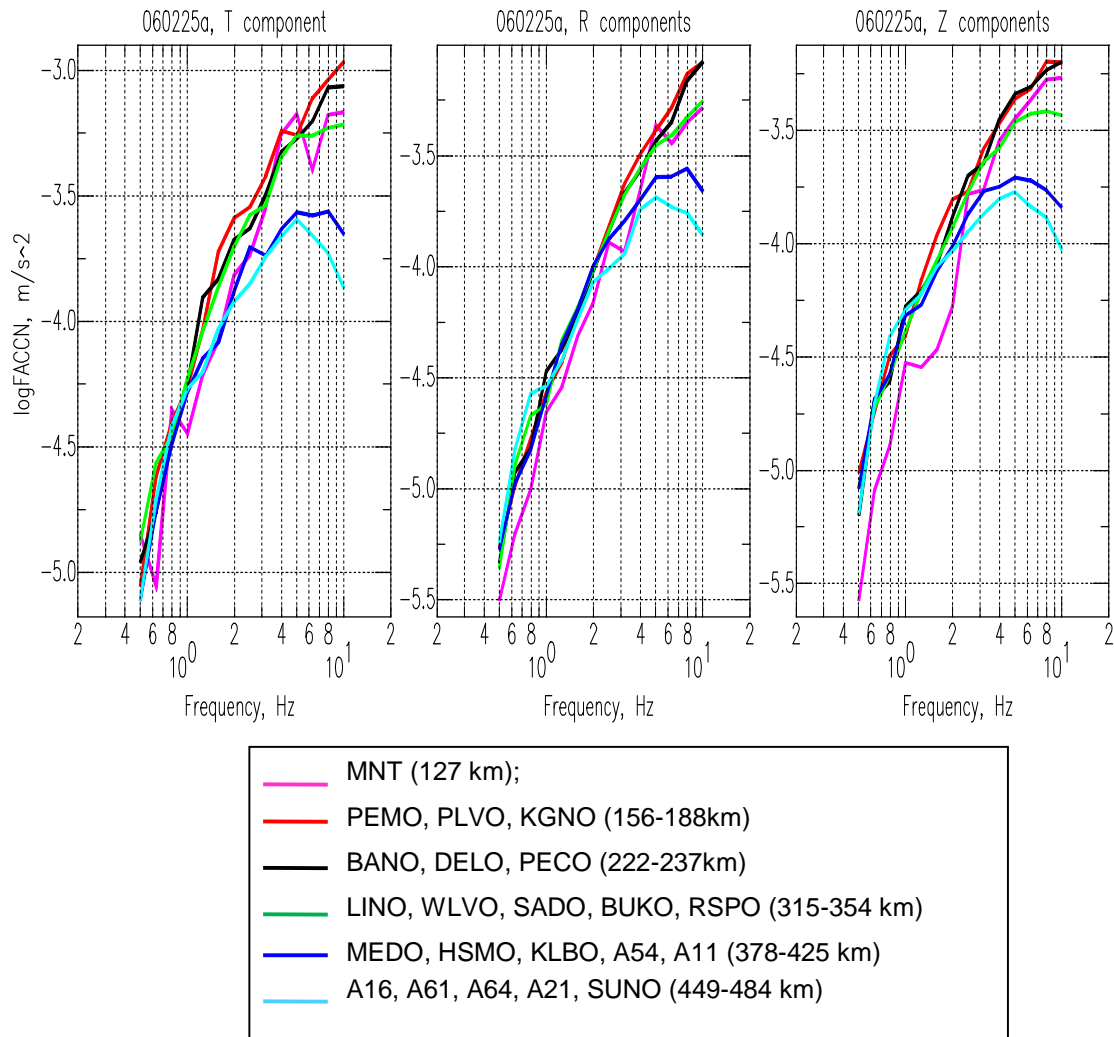


Figure 73: (a) Smoothed Fourier spectra and (b) spectral ratios of horizontal (T and R) and vertical (Z) components of acceleration (S and Rg/Lg waveforms), for the MN=4.5, 25 February 2006 at 1:39AM, h=19 km earthquake recorded by Canadian broadband stations at local and regional distances. Spectra are averaged over stations listed in the legend (their epicenter distances are given in the brackets). Spectra are corrected for instrument and geometrical spreading and reduced to 100 km.

The main conclusion made from comparison of these spectra supports results of studies made earlier by Kafka (1990) and Ma et al. (2008): if the source depth is greater than 4 km, the amplitude of the short-period Rg waves diminishes (Figures 70 through 73). The 1-2 Hz “shoulder” seen on the vertical component spectra, attributed to Rg waves, is strong for shallow events (Figures 67 through 69) at local distances; it diminishes and shifts to lower frequencies within the first few hundred kilometres, reflecting its rapid attenuation, as suggested by Lay and Wallace (1995).

4. IMPLICATIONS FOR OTHER GROUND MOTION PARAMETERS

The ground motion recordings on the surface and underground from the PUPS project can provide insight into ground-motion parameters that are important in the development of ground-motion prediction equations (GMPEs). GMPEs are a cornerstone of probabilistic seismic hazard analysis and assessment. Current GMPE models for eastern North America (ENA) are based largely on expected motions for hard-rock sites, similar to the SUNO, SSNO or 11SNO stations, on the surface. In the work reported in Chapter 3, it is shown that at frequencies less than 2 Hz, underground motions may be significantly lower due to the attenuation of surface waves that contribute to lower-frequency ground motions. It is also apparent that the interpretation of ground motions at $f < 2$ Hz, for stations on the surface, is complicated by these effects. In this section, ground motion parameters that are important in the modelling of ground motion effects in ENA, and in the development of GMPEs for seismic hazard analysis are examined. These parameters are: (i) the attenuation of ground motion in earth's crust within 50 km of the source; and (ii) kappa, the high-frequency decay parameter that acts to filter out high-frequency ground motions. The implications of the study for source parameters such as the stress drop are also discussed.

4.1 ATTENUATION OF GROUND MOTIONS NEAR THE EARTHQUAKE SOURCE (<50 KM)

A key question that controls amplitudes for GMPEs in ENA concerns the rate of attenuation due to geometric spreading within about 50 to 70 km of the earthquake source. The recent GMPEs of Atkinson and Boore (2006) used a geometric spreading rate of $R^{-1.3}$ within the first 70 km, based on an empirical study of spectral amplitudes in ENA at rock sites by Atkinson (2004) (Note: R is hypocentral or fault distance – these distance measures are equivalent for small-to-moderate events). This spreading rate is significantly faster than the theoretical rate of $1/R$ for body-wave spreading in a homogeneous half-space that had been assumed to apply in previous models (e.g., Atkinson and Boore, 1995). The faster decay rate, believed to be due to crustal layering and related path effects, is an important factor in localizing seismic hazard near the earthquake source.

The data at SNO and SUNO provide an excellent opportunity to study attenuation in the critical distance range from 1–50 km. The ground motions from events that occurred very close to either SUNO or SNO are examined, so that attenuation from one station to the other (SUNO and SNO are about 24 km apart) could be determined. Specifically, there are 22 events that occurred within 5 km of SUNO – thus they occurred approximately at SUNO within location error. The average distance of these events from SUNO is 3.3 km and 24 km from SNO. The attenuation of motions for these events from SUNO to the SNO stations SSNO and 11SNO (both on the surface), a distance factor of $24/3.3 = 7.27$, or 0.86 log units, is examined here. The goal is to determine the geometric spreading factor over this distance, to see if it matches the expected rate of $R^{-1.3}$ based on the study of Atkinson (2004).

The general expression for the observed Fourier amplitudes, $A(f)$, at a hypocentral distance R is:

$$\log A(f) = \log A_0(f) - b \log R - c R$$

where $A_0(f)$ is the source spectrum of the event (as a function of frequency), b is the geometric spreading coefficient, and c is the anelastic attenuation. The anelastic attenuation coefficient c is inversely related to the regional Quality factor, Q , by:

$$Q = \pi f / (2.3 c \beta)$$

To determine the geometric spreading coefficient, b , it is necessary to correct the observed spectra for the effects of anelastic attenuation. These effects would normally be quite small over this distance range, but due to the shallow focal depth of the events, the ray paths from the events near SUNO to the surface stations at SNO will be very shallow – within the top few km. Atkinson (2004) found that attenuation is greater for shallow events, which is assumed to be attributable to the lower Q values (higher anelastic attenuation) near the surface. For the very shallow paths involved in this study, an appropriate estimation of Q is required in order to correct the observed amplitudes. Given the hard-rock environment, the shear-wave velocity and stiffness will increase only very slowly in the top kilometer or two, within which the rays travel, and a constant Q model is assumed for the layer as a rough approximation. The Q value will be much higher than those reported for sediments (because the travel paths are entirely within hard, fractured rock), and this places a lower limit of 100 on Q . For example, Langston et al. (2005) report Q values near 100 for deep sediments in the Mississippi Embayment. However, the Q values will be lower than those reported for travel paths deeper in the crust, which are near 1000 for intermediate frequencies (Atkinson, 2004). Thus, a trial value setting the initial Q estimate at 400 was selected, which implies $c = \pi f / (2.3 Q \beta) = 0.00114f$, for an estimated shear-wave velocity in the top 2 km of $\beta = 3$ km/s. The appropriateness of the estimate can be tested by examining the determined values for the b -coefficient as a function of frequency. The apparent geometric spreading rate should be approximately independent of frequency, while anelastic attenuation increases with increasing frequency ($0.00114f$, as above). Thus if the selected Q value is too low, the apparent geometric attenuation will decrease with increasing frequency to compensate, while if the Q value is too high the opposite trend will result.

To determine the apparent geometric spreading rate, the difference between the amplitudes at SUNO, and those at 11SNO or SSNO (for each SNO station), are divided by the difference in log distance, and the values then corrected for anelastic attenuation. For example, if A_1 is the amplitude at SUNO for a near event (within 5 km), and A_2 is the corresponding amplitude at SNO (either 11SNO or SSNO), for a given frequency, then:

$$b = ((\log A_1 - \log A_2)/0.86) - 21 c$$

where the value 0.86 is the difference in distance for the event from SUNO to SNO in log units ($\log 24 - \log 3.3$), and the value 21 is the same distance in linear units ($24 - 3.3$). The frequency range of the analysis should be above those that are affected by the spectral amplitude peaks near 2 Hz due to surface waves, but below the corner frequency of the events, beyond which signals become weak (i.e., in the frequency band from approximately 3 to 20 Hz).

Figure 74 plots the mean geometric spreading value (b) determined from the SUNO/SNO pairs as a function of frequency, along with the standard deviation of the estimates from one station pair to another. Though the variability is significant, the mean values are very stable due to the number of observations (approximately 20). The apparent b value is constant with frequency over the range from 3 to 20 Hz, with a mean value of 1.32 ± 0.06 (standard error of the b estimate, averaged over all frequencies). The constant trend with frequency supports the reasonableness of the choice of $Q=400$. This analysis provides a robust estimate of geometric spreading for body waves within the first 25 km of the earthquake source. It is in good agreement with the value of 1.3 inferred by Atkinson (2004) based on regional studies.

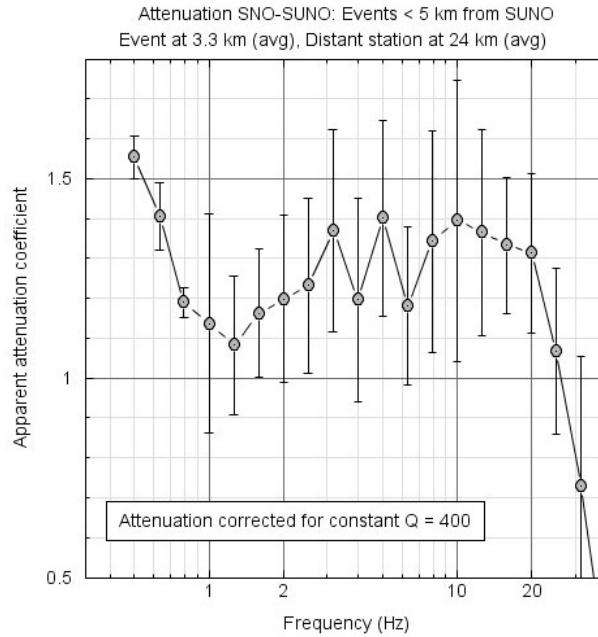


Figure 74: Mean and standard deviation of apparent geometric spreading coefficient (b) from hypocentral distance R = 3 to 24 km, based on 20 shallow events that occurred within 5 km of SUNO, and were recorded at both SUNO and SNO surface stations. Assumes constant Q = 400. Average b = 1.32±0.06

4.2 DETERMINATION OF HIGH-FREQUENCY ATTENUATION FACTOR KAPPA

According to simple earthquake source models, such as the Brune model (Brune, 1970; Boore, 1983), the Fourier displacement spectrum of the earthquake source has a constant value at low frequencies, with amplitude proportional to seismic moment. The spectrum has a “corner frequency” determined by the size of the event, with smaller events having higher corner frequencies. Above the corner frequency, the displacement spectrum decays as frequency-squared. For small events such as the mining events in this study, the corner frequencies are high, well above 10 Hz (verified by inspection of spectral shapes). It has already been concluded that spectral amplitudes for surface stations are elevated for the shallow mining events by strong surface waves (for $f < 3$ Hz). Therefore, it would be expected that the displacement spectra should be relatively flat in the frequency range from 3 to 10 Hz.

A factor that causes the spectral amplitudes to decay with increasing frequency relative to this expectation of a “flat” spectrum is anelastic attenuation. There are two components to this attenuation: the Q effect, discussed above, and the kappa effect. Kappa is a near-source high-frequency attenuation that is believed to be caused by energy absorption in the near-surface layers (Anderson and Hough, 1984). They state that the Fourier amplitudes, corrected for geometric spreading to a distance of 1 km, may be modelled as:

$$A = A_0 \exp(-\pi f \kappa)$$

where the attenuation (κ) is composed of two parts:

$$\kappa = \kappa_0 + R/(Q \beta)$$

In this expression, κ_0 is the near-surface attenuation, and the second term is the anelastic attenuation due to Q effects (Note: when the near-surface factor 'kappa' is referred to, it is usually κ_0 that is meant). According to the above expressions, a plot of the natural log of the displacement amplitudes versus linear frequency will be a straight line with a slope proportional to κ , and a 0-intercept proportional to seismic moment. A plot of κ versus distance will then be another straight line, with 0-intercept of κ_0 and a slope of $1/(Q \beta)$.

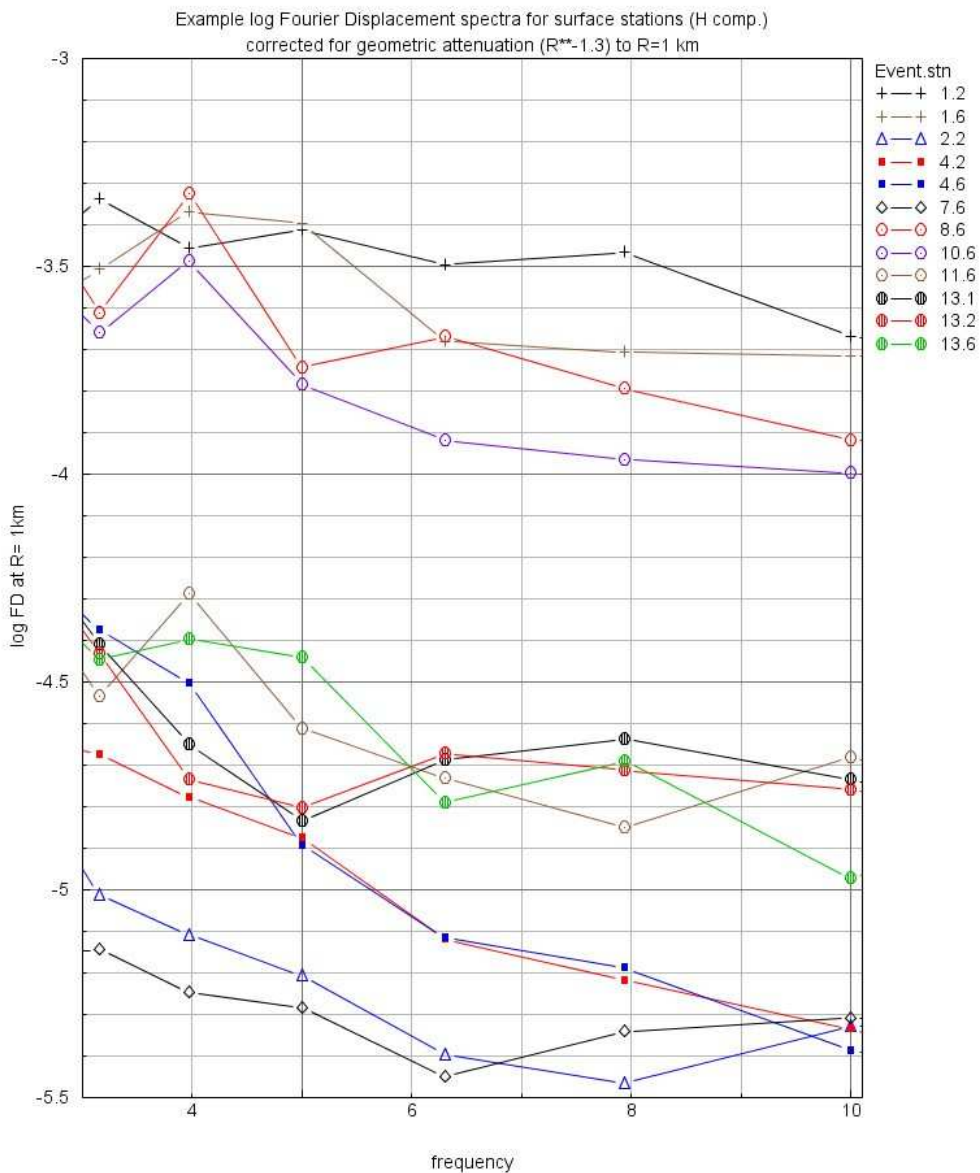


Figure 75: Example Fourier displacement spectra at the source ($R=1$ km) for surface stations.

To determine kappa values, the log Fourier displacement versus frequency is fit in the range from 3 to 10 Hz, for each record of local mining events. The average horizontal and the vertical components are examined separately, as are surface and underground stations. For each analysis set, there are approximately 150 records, representing small events ($M < 3$) at distances < 30 km. Figure 75 shows selected typical records for which slopes are fitted.

On Figure 76, the kappa values determined from all of the slopes are summarized. It is apparent that there is great variability. An estimate can be made of κ_0 but Q will not be reliably determined due to the small distance range. Fitting the kappa values versus distance (for $R < 32$ km), as described above, values of κ_0 of 0.033 and 0.051 are obtained for surface stations, for horizontal and vertical components, respectively. Underground, the corresponding values are 0.038 and 0.022. Standard errors of kappa are 0.005 to 0.006. The inferred κ_0 values are high relative to expectations for hard-rock ENA sites. For example, Atkinson and Boore (2006) use a kappa of 0.006 as a representative value for ENA hard rock. Furthermore, there does not appear to be a significant difference in kappa between the surface and underground stations. It is possible that the relatively large kappa values are attributable to highly-fractured rock, due to the Sudbury meteorite impact structure. They may also represent a source effect for these shallow mining events.

The slopes of the kappa versus distance plot are only significant for two cases: 1) horizontal components on the surface, and 2) vertical components underground. For these two slopes the inferred Q values are 476 and 303, respectively, which is consistent with the assumed value of $Q=400$.

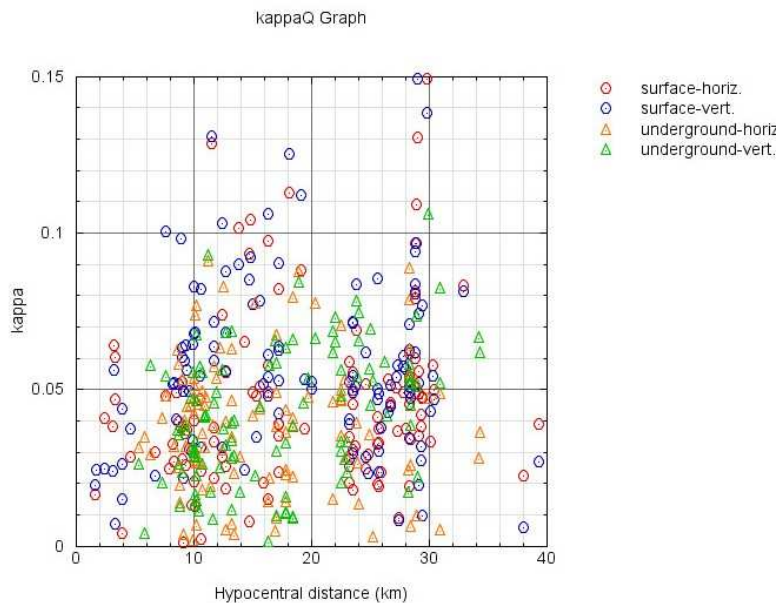


Figure 76: Kappa values determined from slope of log Fourier displacement versus frequency for each record (3-10 Hz).

5. CONCLUSIONS

The PUPS project analyzed ground motions on the surface and underground for 106 local events (shallow mining-induced events and blasts), 66 regional earthquakes (moderate events hundreds of km away), and 73 teleseismic events (large earthquakes >1000 km away). The analyses lead to several important conclusions regarding the differences between earthquake ground motions recorded on the surface and those in underground cavities. Results from the PUPS project demonstrate that, in general, earthquake ground motions underground are lower in amplitude than those on the surface. The relationship between underground and surface motions is complex, with the ratio of surface/underground motions being a frequency-dependent function that depends on the type of earthquake and the depth of the underground cavern. Motions on the surface are amplified in specific frequency ranges due to the presence of surface waves in the signal. For earthquakes at shallow depths, occurring nearby, there are strong surface waves that cause a peak amplification of surface motions relative to those underground that often exceed a factor of two; this peak occurs near a frequency of 2 Hz. For larger earthquakes happening farther away, the surface waves cause amplification at longer periods. These motions decrease in amplitude as the depth of the underground station increases because surface-wave amplitudes diminish with increasing depth. At very low frequencies (0.1 Hz) and at very high frequencies (>10 Hz), underground and surface motions are very similar in amplitudes. Consideration of these factors, when assessing the seismic hazard for underground repositories, may reduce the predicted ground motion levels for specific types of events.

Another important conclusion of this study involves the attenuation of ground motion near the earthquake source. Studies of signals at Sudbury, in comparison to those at SNO, show that ground motions decay at a rate of approximately $R^{-1.3}$ in the first 20 to 30 km from the earthquake source (where R is distance). This supports the ground-motion prediction equations of Atkinson and Boore (2006), and implies that a mitigating factor in seismic hazard studies in Ontario is this relatively steep attenuation of wave amplitudes as we move away from an earthquake source. An unexpected finding of this study is that kappa values, which control the attenuation of motions at very high frequencies, are unexpectedly large (0.02 to 0.05) at both surface and underground sites. This causes diminished ground-motion amplitudes at high frequencies (>5 Hz). However, this finding may be specific to the highly-fractured rock environment near Sudbury, and/or the source characteristics of the shallow mining-induced events that were the focus of the study.

The apparent amplification effects seen in the underground records compared to those on surface can be explained in a qualitative way by considering the dominant phases generated by different types of events at different distances, and their general behaviour. The results from spectra analysis supports the results of Kafka (1990) and Ma et al. (2008), which show that when the source depth is greater than 4 km, the amplitude of the short-period Rg waves diminishes. A fuller understanding of the relationship between the surface and underground records could theoretically be obtained by detailed modelling of the waveforms and their interactions. However, this modelling would require detailed three-dimensional information on the velocity structure that is not available, and would be a complex exercise beyond the scope of this empirical study. Finally, it must be emphasized that the database of regional events is limited by the lack of events at mid-crustal depths, for which surface wave effects may be less important. Careful study of the constituent wave components of the ground-motion signal on a regional basis would allow improved ground-motion prediction models for surface sites, and possibly better prediction capabilities as to how those motions will be modified for underground facilities.

In summary, the studies at SNO have shown that there is a clear de-amplification of ground motions at underground stations relative to those on the surface, which depends on the type of earthquake and the depth of the station. The effect appears to be mostly due to the removal of surface wave energy at depth, and thus depends on the depth of the seismic event and its distance, as well as the depth of the station.

ACKNOWLEDGEMENTS

We wish to thank the Sudbury Neutrino Observatory (SNO) and Vale Inc. for providing various logistical supports throughout the course of the project. We thank Tom Lam and the Nuclear Waste Management Organization for their valuable support of the project.

REFERENCES

- Anderson, J. and S. Hough. 1984. A model for the shape of the Fourier amplitude spectrum of acceleration at high frequencies, *Bull. Seism. Soc. Am.*, 74, 1969-1993.
- Atkinson, G.M. and D.M. Boore 1995. Ground-motion relations for eastern North America, *Bull. Seism. Soc. Am.* 85, 17-30
- Atkinson, G.M. and D.M. Boore. 2006. Ground motion prediction equations for earthquakes in eastern North America. *Bull. Seism. Soc. Am.*, 96, 2181-2205.
- Atkinson, G.M., S. Kaka, D. Eaton, A. Bent, V. Peci and S. Halchuk. 2007. A very close look at a moderate earthquake near Sudbury, Ontario. *Seism. Res. L.*, 79, 119-131.
- Bard, P. 1999. Microtremor Measurements: A Tool for the Effect Estimation? *The Effects of Surface, Geology on Seismic Motion, (Balkeman, Rotterdam)*, 1999 ISBN 90 5809 030 2.
- Bath, M. 1975. Short-period Rayleigh waves from near-surface events, *Phys. Earth Planet. Inter.*, 10, 369-376.
- Beresnev, I. and G. Atkinson. 1997. Shear wave velocity survey of seismographic sites in eastern Canada: Calibration of empirical regression method of estimating site response, *Seism. Res. L.*, 68, 981-987.
- Blakeslee, S. and P. Malin. 1991. High-frequency site effects at two Parkfield downhole and surface stations, *Bull. Seism. Soc. Am.*, 81, 332-345.
- Boerner, D.E., B. Milkereit and A.J. Naldrett. 1994. Introduction to the special section on the Lithoprobe Sudbury Project, *Geophys. Res. Lett.*, 21, 919--922.
- Boerner D.E., B. Milkereit and A. Davidson. 2000. Geoscience impact: A synthesis of studies of the Sudbury structure, *Canadian Journal of Earth Sciences*, 37, 477–501.
- Boll, S. F. 1979. Suppression of acoustic noise in speech using spectral subtraction, *IEEE Tans. Acoust., Speech Signal Processing*, ASSP-27, 113-120.
- Bonner, J.L., J.L. Orrey and A.C. Rosca. 2002. Modeling short-period surface waves from small explosions at the Shagan test site, *24th Seismic Research Review – Nuclear Explosion Monitoring: Innovation and Integration*.
- Boore, D. 1983. Stochastic simulation of high-frequency ground motions based on seismological models of the radiated spectra. *Bull. Seism. Soc. Am.*, 73, 1865-1894.
- Boore, D. 1996. SMSIM – Fortran programs for simulating ground motions from earthquakes, *US Geol. Surv. Open-file Rpt.* 96-80-A.
- Boore, D. and W. Joyner. 1997. Site amplifications for generic rock sites, *Bull. Seism. Soc. Am.*, 87, 327-341.

- Bormann, P. (Ed.). 2002. IASPEI: New manual of seismological observation practice (NMSOP), GeoForschungsZentrum Potsdam.
- Brune, J. 1970. Tectonic stress and the spectra of seismic shear waves from earthquakes. *J. Geophys. Res.*, 75, 4997-5009.
- Davídek, V., P. Sovka and J. Šika. 1995. Real-Time Implementation of Spectral Subtraction Algorithm for Suppression of Acoustic noise in Speech. In *Proc. of EUROSPEECH '95* Madrid, 141-144.
- De Luca G., E. Del Pezzo, F. Di Luccio, L. Margheriti, G. Milana and R. Scarpa. 1998. Site response study in Abruzzo (Central Italy): underground array versus surface stations, *Journal of Seismology*, 2, 223-236.
- Fukushima, Y., J. Gariel and R. Tanaka. 1995. Site-Dependent Attenuation Relations of Seismic Motion Parameters at Depth Using Borehole Data, *Bull. Seism. Soc. Am.*, 85, 1790-1804.
- Goforth, T.T. and J.L. Bonner. 1995. Characteristics of Rg waves recorded from quarry blasts in Central Texas, *Bull. Seism. Soc. Am.*, 85, 1232-1235.
- Goforth, T.T., Hetzer, C.H. and B.W. Stump. 2006. Characteristics of regional seismograms produced by delay-fired explosions at the Minntac Iron Mine, Minnesota, *Bull. Seism. Soc. Am.*, 96, 272-287.
- Graizer, V., T. Cao, A. Shakal and P. Hipley. 2000. Data from downhole arrays instrumented by the California Strong Motion Instrumentation Program in studies of site amplification effects, presented at the Proceedings of the 6th International Conference on Seismic Zonation, Palm Springs, California.
- Gutenberg, B. 1951. Observation and theory of microseisms, in *Compendium of Meteorology*, edited by T.F. Malone, *Am. Meteorol. Soc., Providence, R. I.* 1303-1311
- Hanks, T. 1982. fmax. *Bull. Seism. Soc. Am.*, 72, 1867-1879.
- Jenkins, G.M. and D.G. Watts. 1969. Spectral analysis and its applications. Holden-Day, San Francisco, Cambridge, London, Amsterdam.
- Kafka, A.L. 1990. Rg as a depth discriminant for earthquakes and explosions: a case study in New England, *Bull. Seism. Soc. Am.*, 80, 373-394.
- Kanai, K. and T. Tanaka. 1951. Observations of the earthquake-motion at the different depths of Earth. I, *Bull. Earthq. Res. Inst.*, 29, 107-113.
- Kedar, S., M.F. Longuet-Higgins, N. Webb, R.C. Graham and C. Jones. 2008. The origin of deep ocean microseisms in the North Atlantic Ocean. *Proc. R. Soc. A* 8 March 464/2091, 777-793.

- Kinoshita, S. 1999. A stochastic method for investigating site effects by means of a borehole array *SH* and Love waves, *Bull. Seism. Soc. Am.*, 89, 484-500.
- Kinoshita, S. 2008. Deep-borehole-measured Q_P and Q_S attenuation for two Kanto sediment layer sites, *Bull. Seism. Soc. Am.*, 98, 463-468.
- Kocaoglu, A.H. and L.T. Long. 1993. Tomographic inversion of R_g wave group velocities for regional near-surface velocity structure, *J. Geophys. Res.*, 98, 6579-6587.
- Lay, T. and T. Wallace. 1995. Modern global seismology, Academic Press.
- Lida, M., H. Yamanaka and N. Yamada. 2005. Wave Field Estimated by Borehole Recordings in the Reclaimed Zone of Tokyo Bay, *Bull. Seism. Soc. Am.*, 95, 1101-1119.
- Longuet-Higgins, M. 1950. A theory of the origin of microseisms, *Philos. Trans. R. Soc. London*, 243, 1-35.
- Ma, S., D. Eaton and J. Adams. 2008. Intraplate seismicity of a formerly glaciated shield terrane: A case study from northern Ontario, Canada. *Bull. Seism. Soc. Am.*, 98, 2828-2848.
- Ma, S. and D.W. Eaton. 2009. Anatomy of a Small Earthquake Swarm in Southern Ontario, Canada, *Seism. Res. Lett.*, 80, 214-223.
- Malek, F., C. Trifu, F. T. Suorineni, S. Espley and M. Yao. 2008. Management of High Stress and Seismicity at Vale Inco Creighton Mine, *American Rock Mechanics Association, The 42nd U.S. Rock Mechanics Symposium (USRMS), June 29 - July 2, 2008, San Francisco, CA*, 08-386.
- Malovichko, D.A. 2005. Study of "low-frequency" seismic events sources in mines of the Verkhnekamskoye potash deposit. *Controlling seismic risk. Proceedings of the Sixth International Symposium on Rockbursts and Seismicity in Mines, 9-11 March 2005, Australia, Perth, ACG*, 373-377.
- Malovichko, D.A. and Yu.V., Baranov. 2001. Application of numerical modelling for analysis of underground recordings of seismic events. In *Proc. of the 5th Symposium on Rockbursts and seismicity in mines, Megaliesberg, 2001* (eds. G. Van Aswegen, R.J.Durrheim, W.D.Ortlepp) SAIMM, Johannesburg, South Africa, 479-482.
- Matsunami, K., W. Zhang, K. Irikura and L. Xie. 2003. Estimation of Seismic Site Response in the Tangshan Area, China, Using Deep Underground Records, *Bull. Seism. Soc. Am.*, 93, 1065-1078.
- McLaughlin, K. L., J. L. Bonner and T. Barker. 2004. Seismic source mechanisms for quarry blasts: modeling observed Rayleigh and Love wave radiation patterns from a Texas quarry, *Geophys. J. Int.*, 156, 79-93.
- Milkereit, B., D. Eaton, J. Wu, G. Perron, M. Salisbury, E. K. Berrer and G. Morrison. 1996. Seismic imaging of massive sulfide deposits: Part II. Reflection seismic profiling, *Economic Geology*, 91, 829-834.

- Milkereit, B. and D. Eaton. 1998. Imaging and interpreting the shallow crystalline crust, *Tectonophysics*, 286, 5-18.
- Milkereit, B. and A. Green. 1992. Deep geometry of the Sudbury Structure from seismic reflection profiling, *Geology*, 20, 807-811.
- Moon, W.M. and L.X. Jiao. 1998. Sudbury meteorite-impact structure modeling with LITHOPROBE high-resolution seismic refraction results, *Geoscience Journal*, 2, 26- 36.
- Nuttli, O.N. 1973. Seismic Wave Attenuation and Magnitude Relations for Eastern North America, *J. Geophys. Res.*, 78, 876-885.
- Okada, Y., K. Kasahara, S. Hori, K. Obara, S. Sekiguchi, H. Fujiwara and A. Yamamoto. 2004. Recent progress of seismic observation networks in Japan —Hi-net, F-net, K-NET and KiK-net, *Earth Planets Space*, 56, xv–xxviii.
- Plesinger, A. M. Hellweg and D. Seidl. 1986. Interactive high-resolution polarization analysis of broad-band seismograms, *J. Geophys.*, 59, 129-139.
- Russell, D. 2001. Acoustics Animations: Rayleigh surface waves, Kettering University Applied Physics, <http://www.gmi.edu/~drussell/Demos/waves/wavemotion.html>.
- Saikia, C. K. 1992. Numerical study of quarry generated Rg as a discriminant for earthquakes and explosions: Modeling of Rg in Southwestern New England, *J. Geophys. Res.*, 97, 11057-11072.
- Salisbury, M.H., R. Luliucci and C. Long. 1994. Velocity and reflection structure of the Sudbury Structure from laboratory measurements, *Geophys. Res. Let.*, 21, 923–926.
- Shearer, P. M. and J. A. Orcutt. 1987. Surface and near-surface effects on seismic waves theory and borehole seismometer results, *Bull. Seism. Soc. Am.*, 77, 1168-1196.
- Siddiqi, J. and G. Atkinson. 2002. Ground motion amplification at rock sites across Canada, as determined from the horizontal-to-vertical component ratio, *Bull. Seism. Soc. Am.*, 92, 877-884.
- Soczkievicz, E. 1997. The penetration depth of the Rayleigh surface waves, *Nondestructive Testing and Evaluation*, 13, 113 – 119.
- Sovka, P., P. Pollak and J. Kybic. 1996. Extended Spectral Subtraction, in *European Signal Processing Conference (EUSIPCO-96)*, Trieste, Italy.
- Wu, J., B. Milkereit and D. Boerner. 1995. Seismic imaging of the enigmatic Sudbury structure, *J. Geophys. Res.*, 100, 4117-4130.
- Yamanaka, H., K. Motoki, K. Etoh, M. Murayama and N. Komaba. 2004. Observation of aftershocks of the 2003 Tokachi-Oki earthquake for estimation of local site effects, *Earth Planets Space*, 56, 335–340.